Swansea University
Prifysgol Abertawe

IN-SITU MAPPING OF LOCALISED CORROSION UNDER THE EFFECT OF STRAIN USING A SCANNING VIBRATING ELECTRODE TECHNIQUE

Roberto Alcivar Andrade, BEng,

[redacted]

Academic Supervisor: Prof. Geraint Williams,
Swansea University

Industrial Supervisor: Dr. Ronald Clark,
National Nuclear Laboratory

Industrial Sponsor: National Nuclear Laboratory

Submitted to Swansea University in fulfilment of the requirements for the Degree of Master of Science in Materials Engineering.

2024

Abstract

Stress Corrosion Cracking (SCC) is a type of material degradation characterised by the combined effect of tensile stress and localised corrosion produced by aggressive ions such as chlorides. It is very difficult to detect and has caused catastrophic failures of components in service at diverse industries. Several researchers have investigated this phenomenon using different approaches, but the role of the stress in the initiation and propagation stage is still not fully understood.

Previous studies have shown that the scanning vibrating electrode technique (SVET) can be used to map pitting corrosion sites on austenitic stainless steels (SS) in non-strained conditions. The present research looks to expand the scope of this technique, employing SVET analysis of strained and non-strained samples of 304 SS in the annealed and thermally sensitised condition. Such samples were tested in 3 M and 4 M $MgCl_2$ concentrations, aiming to obtain relevant data that can improve the understanding of the role of stress in the initiation of pitting corrosion.

As part of the experiments carried out, droplet tests were performed on annealed and sensitised samples under strained and non-strained conditions, determining that 4 M $MgCl_2$ was the ideal concentration whereby spontaneous formation of pits in open circuit conditions was reproducibly observed. Subsequently, the samples were immersed in this chloride electrolyte and the localised corrosion behaviour was studied in-situ using the SVET. The current density maps obtained showed that applied strain can decrease the decay rate of anodic current density for the propagating pits compared with the un-strained surface. Additionally, these results were complemented with potentiodynamic polarisation, optical microscopy, scanning electron microscopy and height-depth microscopy, which showed morphologies and other relevant characteristics. The results obtained could open new research lines to investigate the role of stress in the initiation of SCC in nuclear cladding alloys.

In a separate experiment, the localised corrosion characteristics of coupons consisting of a bespoke nuclear cladding alloy (20Cr/25Ni/Nb) electron beam welded to a simulant sensitised grain boundary alloy (45Fe/45Ni/10Cr) was carried out. The tests performed included potentiodynamic polarisation studies of the alloy, weld, and simulant grain boundary regions separately along with, SVET and SKP analysis of the test coupon as a whole. Spatially resolved SKP-derived maps determined the relative nobility of the cladding in comparison to the simulant alloy, and SVET studies showed that the weld joint was most susceptible to localised corrosion initiation under immersion conditions.

Author Declarations

This work has not previously been accepted in substance for any degree and is not being concurrently submitted in candidature for any degree.

Signed: _[redacted]_____

Date: 08/04/2024

This thesis is the result of my own investigations, except where otherwise stated. Other sources are acknowledged by footnotes giving explicit references. A bibliography is appended.

Signed: _[redacted]_____

Date: 08/04/2024

I hereby give consent for my thesis, if accepted, to be available for electronic sharing.

Signed: _[redacted]_____

Date: 08/04/2024

The University's ethical procedures have been followed and, where appropriate, that ethical approval has been granted.

Signed: _[redacted]_____

Date: 08/04/2024

Table of contents

List of Figures vi

List of Tables xi

0.1 Glossary xii

1 **Literature Review** 1

1.1 Overview 1
1.2 Fundamentals of corrosion 2
1.2.1 Thermodynamics of corrosion 4
1.2.2 Kinetics of corrosion 8
1.3 Localised corrosion 11
1.3.1 Intergranular corrosion 11
1.3.1.1 Intergranular corrosion in austenitic stainless steel 11
1.3.2 Pitting corrosion 13
1.3.2.1 Pitting corrosion initiation and growth 15
1.3.2.2 Effect of inclusions in the pitting process of steels 18
1.3.3 Stress Corrosion Cracking 19
1.3.3.1 Study of SCC in different types of steels 20
1.3.3.2 The role of applied stress in the initiation of SCC 22
1.4 Nuclear industry in the UK 25
1.4.1 Advance Gas-cooled Reactors (AGR) 26
1.4.1.1 Fuel cladding material in AGR 27
1.4.1.2 Spent nuclear fuel cladding alloy and concerns on its integrity.... 29

2 Experimental Details 32

2.1 Stainless steel AISI 304 specimens and conditions 32
2.1.1 Material 32
2.1.2 Environment 32
2.1.3 Tensile load 33
2.2 Droplet test 34
2.3 Uniaxial tensile test 35
2.3.1 Uniaxial Tensile test on samples with pits nucleated on surface 36
2.4 Scanning vibrating electrode technique (SVET) 37
2.4.1 SVET calibration 39
2.4.2 SVET height scan profile 41
2.4.3 SVET experiments 43
2.5 DC Electrochemistry 44
2.5.1 OCP measurement 44

2.5.2 Potentiodynamic polarisation curves 45
2.6 Coupons of 20Cr/25Ni/Nb – 45 Fe/45Ni/10Cr 45
2.6.1 Electrochemistry - Coupons of 20Cr/25Ni/Nb – 45Fe/45Ni/10Cr 46
2.6.2 SVET - Coupons of 20Cr/25Ni/Nb – 45Fe/45Ni/10Cr 47
2.6.3 Scanning Kelvin Probe (SKP) 47
2.6.3.1 SKP setup and calibration 49
2.6.3.2 SKP – coupons of 20Cr/25Ni/Nb – 45Fe/45Ni/10Cr 50
2.7 List of experiments performed 50

3 In-situ mapping of localised corrosion under the effect of strain using a scanning vibrating electrode technique 52
3.1 Introduction 52
3.2 Droplet test 54
3.2.1 Droplet test in non-strained conditions 55
3.2.2 Droplet test in strained conditions 62
3.2.3 Pitting process during droplet test 69
3.2.4 Uniaxial tensile test on samples with pits nucleated on surface 70
3.3 DC Electrochemical experiments 72
3.4 Scanning Vibrating Electrode Technique 75
3.4.1 SVET experiments in 4 M $MgCl_2$ 76
3.4.1.1 SVET-AISI 304 as received in non-strain and strained conditions. 76
3.4.1.2 SVET-AISI 304 sensitised in non-strain and strained conditions... 81
3.4.2 Pit morphology obtained during the SVET experiments 85
3.4.3 Effect of strain in the current density measurements obtained with the SVET 90
3.5 Conclusions 92
3.6 Suggestions for future work 93
4 **Corrosion behaviour of 20Cr/25Ni/Nb - 45Fe/45Ni/10Cr coupons** 95
4.1 DC electrochemistry 95
4.2 SVET experiments on 20Cr/25Ni/Nb - 45Fe/45Ni/10Cr coupons 97
4.3 SKP experiments on 20Cr/25Ni/Nb - 45Fe/45Ni/10Cr coupons 102
4.4 Conclusions 103
4.5 Suggestions for future work 104

List of References …… 105

Acknowledgements

I would like to express my sincere gratitude to all the people who have been involved, directly or indirectly, in the realisation of this project.

First, I would like to thank the people who believed in me and gave me the opportunity to pursue this master's degree. I am especially grateful to the M2A staff (Rebecca White, Thomas Lewis, and David Warren) and my supervisors Geraint Williams and Ronald Clark for their guidance, support, and advice. It was an honour and a privilege to work with them.

The financial support from the funding bodies EPSRC, WEFO, and National Nuclear Laboratory was essential for me to pursue this degree. I am grateful for their belief in people who want to make contributions to science and engineering. I would also like to thank Stacey Moore for sharing the three-point strain rig design and Kuo Yuan for performing the sensitisation heat treatment on the samples.

I could not have completed all the experiments without the guidance of Peter Morgan on the SVET, Helena Ferreira and Rebecca Dewfall on the SEM, Monique Latty on the potentiostat, and Gareth Jones on the SKP. Thank you all for your help and support. I really appreciate the laughs we shared.

I would also like to express my gratitude to my undergraduate mentors Jorge Stella and Omar Quintero from Universidad Simon Bolivar. I feel very fortunate to have had such great professors, thanks for your mentoring.

I want to thank my family, Mamá, Papá, Cristhian, and Iliana, for always being there for me, even if we are thousands of miles away. My grandparents Maria and Luis, who are not longer with me, but their guidance and love are always present.

My last mention is to my partner in life and my daughter, Zoe and Gabriella, who did not hesitate to move to Swansea and give me all the support, love and motivation I needed to accomplish this dream. Thanks for being by my side, Love you both!

I am truly grateful for the support of all these amazing people. Without them, this project would not have been possible.

List of Figures

1.1 The components of an electrochemical corrosion cell [3] 4

1.2 Schematic Diagram E vs pH for Fe in water [4] 7

1.3 Schematic polarization diagram for an active – passive metal [4] 10

1.4 Schaeffler diagram for some common stainless-steel grades [9] 12

1.5 Schematic diagram of the various shapes of pits shown in cross section [12] .. 14

1.6 Schematic of Fontana and Greene model for crevice corrosion initiation of stainless steels in aerated Cl- solution [19] 16

1.7 Schematic of a corrosion pit on a metal in an environment rich in chloride ions [4] 18

1.8 Types of pitting observed at MnS inclusions on 304 SS in 1 M NaCl with and without applied stress reported by Suter and others [33] 23

1.9 Schematic illustration of pit initiation mechanisms at (Mn,Cr)S inclusions with and without applied stress [35] 25

1.10 Fuel element example [5] 26

2.1 Three-point strain rig (left 3D design, right prototype) 33

2.2 Three-point strain rig plot (units in millimetres) 34

2.3 Example of droplet test on AISI 304 samples. a). Non- strained conditions, b) Strained conditions, c) Cross-sectional set-up 36

2.4 Example of a AISI 304 specimen under tensile test 37

2.5 Schematic representations of the SVET probe assembly [58] 38

2.6 Example of the SVET use in the study of corrosion 38

2.7 SVET setup calibration with a two-compartment tube cell [58] 39

2.8 SVET calibration setup 40

2.9 Example of a typical SVET calibration plot for a 4 M $MgCl_2$ solution 41

2.10 SVET 3D height scan modelling 42

2.11 SVET experimental setup for a strained sample using the three-point strain rig. 44

2.12 Location of the three different test regions for coupons of 20Cr/25Ni/Nb – 45Fe/45Ni/10Cr. Yellow square cladding material, Green square Cladding welded to the simulant, and Blue square simulant material 46

2.13 SKP experiment setup 49

3.1 AISI 304 microstructure, a) As received, and b) thermally sensitised. Both images at 20X magnification obtained with an optical microscope 54

3.2 Pit morphology of SS 304 samples tested with 3 M $MgCl_2$ droplets in non-strained conditions, obtained with an optical microscope: a-b) SS 304 as received (50X), c) SS 304 sensitised (50X), d) SS 304 sensitised (20X) 57

3.3 Pit morphology of SS 304 samples tested with 4 M $MgCl_2$ droplets in non-strained conditions, obtained with SEM at different magnifications: a-b) SS 304 (as received), c-d) SS 304 (sensitised) 59

3.4 Pit morphology of SS 304 samples tested with 4 M $MgCl_2$ droplets in non-strained conditions. Obtained with the SEM at different magnifications: a-b) SS 304 (as received), c-d) SS 304 (sensitised) 61

3.5 Pit morphology of sensitised SS 304 samples tested with 4 M $MgCl_2$ droplets in non-strained conditions. Obtained with SEM at different magnifications and highlighting microcavities found along grain boundaries 62

3.6 Pit morphology of SS 304 samples under strained conditions, a) 1 M $MgCl_2$ (sensitised) obtained with SEM, b) 2 M $MgCl_2$ (as received) obtained with an optical microscope (50X) 65

3.7 Pit morphology of SS 304 samples in 4 M $MgCl_2$ in strained conditions, obtained with SEM at different magnifications. a-b) SS 304 (as received), c-d) SS 304 (sensitised).: a-b) SS 304 (as received), c-d) SS 304 (sensitised) 66

3.8 Pit morphology of SS 304 sensitised tested with 4 M $MgCl_2$ droplets in strained conditions, obtained with SEM at different magnifications. a) Colony of pits, b) Satellite pit, and c) Pit with crystallographic etching ……. 67

3.9 Pit morphology of SS 304 sensitised sample tested with 4 M $MgCl_2$ droplets in strained conditions, obtained with SEM …… 68

3.10 Different stages of the pitting process for the thermally sensitised SS 304 in non-strained condition tested with 4 M $MgCl_2$ droplets, a) at 0 h, b) at 24h, c) after 50 h, d) after cleaning with oxalic acid 10% w/v (obtained with SEM and rotated 90°) ……. 70

3.11 Pits nucleated on the surface of AISI 304 uniaxial tensile test specimens obtained with an optical microscope at different magnifications, a) Pit on as received material before the test, b) Pit on the as received material after the test, c) Pit on the sensitised sample before the test, d) Pit on the sensitised sample after the test. The orange arrows exemplify the tensile load applied during the test ….. 72

3.12 Potentiodynamic polarisation curves of AISI 304 in the as received condition in 1 M NaCl, for strained and non-strained samples ……. 73

3.13 Potentiodynamic polarisation curves of AISI 304 in the thermally sensitised condition in 1 M NaCl for strained and non-strained samples ……. 74

3.14 SVET current density maps for AISI 304 as received in non-strained conditions, immersed in 4 M $MgCl_2$, a) 0h, b) 6h, c) 24h ……. 78

3.15 Evolution of SVET current density measurements (J_z) for AISI 304 as received in non-strained condition. a) Current density values in the cross-section of the highest anode location taken at different times, b) Maximum current density at the pit as a function of the time ……. 79

3.16 SVET current density maps for AISI 304 as received in strained condition immersed in 4 M $MgCl_2$, a) 0h, b) 6h, c) 24h …….. 80

3.17 Evolution of SVET current density measurements (J_z) for AISI 304 as received in strained condition. a) Current density values in the cross-section of the highest

anode location taken at different times, b) Maximum current density at the pit as a function of the time …… 81

3.18 SVET current density maps for AISI 304 sensitised in non-strained condition immersed in 4 M $MgCl_2$, a) 0h, b) 6h, c) 24h …… 82

3.19 Evolution of SVET current density measurements (J_z) for AISI 304 sensitised in non-strained condition. a) Current density values in the cross-section of the highest anode location taken at different times, b) Maximum current density at the pit as a function of the time …… 83

3.20 SVET current density maps for AISI 304 sensitised in strained condition immersed in 4 M $MgCl_2$, a) 1h, b) 6h, c) 24h …… 84

3.21 Evolution of SVET current density measurements (J_z) for AISI 304 sensitised in strained condition. a) Current density values in the cross-section of the anode location taken at different times, b) Maximum current density at the pit as a function of the time …… 85

3.22 Pit morphology obtained during SVET experiments in 4 M $MgCl_2$, observed with SEM at different magnifications. a) AISI 304 as received non-strained, b) AISI 304 as received strained, c) AISI 304 sensitised non-strained, d) AISI 304 sensitised strained. …… 87

3.23 Current density variation and its relationship with the pit morphology ……. 88

3.24 Pit morphology obtained during SVET experiments in 4 M $MgCl_2$, obtained with SEM at different magnifications. a) SS 304 as received strained, b) SS 304 sensitised non-strained, c-d) SS 304 sensitised strained …… 89

3.25 Effect of strain in the current density values obtained at pit sites, a) As received material, b) Thermally sensitised …… 91

3.26 Pit depth profile obtained with the VHX-1000 digital microscope. a) AISI 304 as received non-strained. b) AISI 304 as received strained, c) AISI 304 sensitised non-strained, d) AISI 304 sensitised strained …… 92

4.1 Potentiodynamic polarisation curves of different isolated regions for 20Cr/25Ni/Nb - 45Fe/45Ni/10Cr coupons in 1 M NaCl solution 97

4.2 20Cr/25Ni/Nb-45Fe/45Ni/10Cr coupon following potentiodynamic polarisation in 1 M NaCl 97

4.3 Illustration of the area exposed during the SVET experiments 98

4.4 SVET current density maps for 20Cr/25Ni/Nb - 45Fe/45Ni/10Cr coupons in 1 M NaCl solution. a) 0 h, b) 2 h, c) 3h, d) 5h, e) 16 h, f) 21h 99

4.5 Intergranular corrosion site observed on the weld joint of the 20Cr/25Ni/Nb - 45Fe/45Ni/10Cr coupons tested with the SVET in 1 M NaCl, obtained with an optical microscope at different magnifications 101

4.6 OCP measurements for 20Cr/25Ni/Nb-45Fe/45Ni/10Cr coupons in 1 M NaCl..... 102

4.7 Line scans obtained with the SKP on 20Cr/25Ni/Nb - 45Fe/45Ni/10Cr coupons. a) Line scan '0', b) Line scan '3', c) Line scan '6'..... 103

List of tables

1 List of abbreviations xii

1.1 The different forms of corrosion [2] 3

1.2 Nuclear power stations in the UK (1956 – 2035) [38] 27

1.3 20Cr-25Ni-Nb stainless steel typical composition (wt%) [41] 28

2.1 AISI 304 composition (wt%) - provided by Goodfellow Cambridge LTD 32

2.2 Samples tested, techniques and conditions 51

3.1 Tensile test result for AISI 304 (as received and sensitised) 53

3.2 Droplet test results for non-strained AISI 304 samples 56

3.3 Average pit diameter comparison for non-strained AISI 304 samples 56

3.4 Droplet test results for strained AISI 304 samples 63

3.5 Average pit diameter comparison for strained AISI 304 samples 63

3.6 Tensile test results for AISI 304 (as received and sensitised) on samples with and without a pit nucleated on the surface 71

3.7 Potential values obtained for AISI 304 annealed and thermally sensitised under strained and non-strained conditions in 1 M NaCl 75

0.1 Glossary

Table 1 List of abbreviations

Acronym	Description
AC	Alternating Current
AGR	Advance Gas-cooled Reactors
AISI	American Iron and Steel Institute
AMPP	Association for Materials Protection and Performance
ASTM	American Society for Testing and Materials
C-SCC	Caustic Stress Corrosion Cracking
Cl-SCC	Chloride Stress Corrosion Cracking
DC	Direct Current
EDS	Energy Dispersive X-ray Spectroscopy
EN	Electrochemical Noise
FCC	Face Centred Cubic
GB	Grain Boundaries
GDF	Geological Disposal Facility
HAZ	Heat Affected Zone
HE	Hydrogen Embrittlement
HS-AFM	High-Speed Atomic Force Microscopy
HSLA	High Strength Low Alloy
IGC	Intergranular corrosion
NNL	National Nuclear Laboratory
OCP	Open Circuit Potential
PTFE	Polytetrafluoroethylene
PWR	Pressurised Water Reactor
REDOX	Oxidation-Reduction Reaction
RIS	Radiation Induced Segregation
SCC	Stress Corrosion Cracking
SCE	Saturated Calomel Electrode
SEM	Scanning Electron Microscope
SHE	Saturated Hydrogen Electrode
SKP	Scanning Kelvin Probe
SNF	Spent Nuclear Fuel
SS	Stainless Steel
S-SCC	Sulphide Stress Corrosion Cracking
SSRT	Slow Strain Rate Stress
SVET	Scanning Vibrating Electrode Technique
THORP	Thermal Oxide Reprocessing Plant
UTS	Ultimate Tensile Strength
XCT	X-ray Computer Tomography

Chapter 1

1. Literature Review

1.1 Overview

It is no secret that the modern world is built around energy. The society's reliance on electricity has made it essential to find and use energy from whatever source is available.

The electricity we consume is produced by four main industries: fossil fuels, renewables, hydroelectric, and nuclear. Each of these industries uses a vast array of components to generate and transmit the energy produced. These devices are exposed to a wide range of challenging operational conditions and are prone to failure during their service life.

Failure modes in materials can be classified into two groups: mechanical and environmental.

- Mechanical failures are caused by the application of force or stress that exceeds the mechanical properties of the material. Examples of mechanical failures include fatigue, erosion, overloading, fretting, and creep.
- Environmental failures are caused by the exposure to harmful environments, such as high temperatures, chemicals, or radiation. Examples of environmental failures include corrosion and hydrogen embrittlement.

Despite decades of research, the full details of some materials failure are not fully understood. This is due to the high number of variables that can influence the failure process and how they interact with each other.

A good example of a complex failure mode that combines mechanical and environmental factors is stress corrosion cracking (SCC). SCC is difficult to detect and can lead to sudden and catastrophic failures in components during service. One of the challenges in studying SCC is understanding the effect of strain in the early

stages of the process, and it has proven difficult to study using conventional characterisation and electrochemical techniques [1-4].

SCC is a particularly undesirable phenomenon in the storage of spent nuclear fuel (SNF) from Advanced Gas-cooled Reactors (AGR). The nuclear fuel is encapsulated in a bespoke fuel pin cladding alloy made of 20Cr/25Ni/Nb. Once they reach the end of their useful life, the SNF is stored in highly controlled water ponds, where localised corrosion can develop over time. Any threat to the integrity of these components that could lead to the release of radioactive material during storage is a serious concern that must be addressed [5].

For this reason, a full understanding of the variables involved in SCC is of high interest to the nuclear industry. The use of non-conventional techniques, such as scanning vibrating electrode technique (SVET), may prove to be key to finding the missing information. In recent years, SVET has been successfully used to map the initiation of pitting corrosion in different metals and alloys. However, its use in the study of SCC is scarce and it could prove to be a useful tool [6,7].

The aim of this research project is to use the SVET to map localised corrosion sites in an alloy known to be susceptible to SCC in chloride-rich environments while the sample is under tensile load. The results of this study could contribute to a better understanding of the role of strain in the SCC process and help to develop future SVET-SCC experiments using specific nuclear materials, such as 20Cr/25Ni/Nb stainless steel.

The following literature review covers the basic theory of corrosion and SCC, the most relevant findings related to the study of SCC in the early stages, and an overview of the nuclear cladding material and its operational conditions.

1.2 Fundamentals of corrosion

Corrosion is a natural electrochemical process that occurs when a material, typically a metal, reacts with its environment. The environment is defined as the surrounding medium in contact with the material. The reactions typically result in a change in the material's properties that can be detrimental to its integrity. In fact,

corrosion is one of the main failure modes of components during service in several industries, and it can have a significant economic, environmental, and health impact [1].

There are several factors that govern the reaction between the material and its environment, and changes in these factors can alter the outcome of this process. The most relevant factors are [1]:

- The physical state of the environment.
- The chemical composition of the material and the environment (constituents and concentrations).
- Velocity of the solution.
- Residual or applied stress.

Consequently, the Association for Materials Protection and Performance (AMPP) classifies corrosion into 3 main groups that can be seen in table 1.1, the difference between them can be explained when most of the conditions in the interaction material/environment are identified.

Table 1.1 The different forms of corrosion [2].

Group 1: Corrosion readily identifiable by ordinary visual examination	Group 2: Corrosion requiring supplementary means of examination	Group 3: Corrosion requiring verification by microscopy
• Uniform • Pitting • Crevice • Filiform • Pack Rust • Galvanic • Lamellar	• Erosion • Cavitation • Fretting • Intergranular • Exfoliation • Dealloying (also known as selective leaching)	• Environmental cracking • Stress Corrosion Cracking (SCC) • Corrosion Fatigue • Hydrogen Embrittlement

1.2.1 Thermodynamics of corrosion

Thermodynamics is the main reason why materials react with their environment. Metals combine with other elements or ions present in their surroundings because the product formed is thermodynamically more stable. To understand the basics of corrosion and electrochemistry, it is important to understand what constitutes a corrosion cell and how it works [2,3]. An example of a corrosion cell can be found in figure 1.1, and its constituents are explained below:

- An anode, where the oxidation reaction happens (loss of metal due to loss of electrons).

$$M \rightarrow M^{n+} + ne^- \quad (1.1)$$

  Where M is the Metal, M^{n+} is the metal cation, and ne^- is the number of electrons.

- A cathode, where the reduction reaction occurs (consumption of electrons that 'protect' the material).

$$M^{n+} + ne^- \rightarrow M \quad (1.2)$$

- A metallic and electrolytic path between both electrodes that allows the passage of ions and electrons that participate in both reactions (anodic and cathodic).
- A potential difference that allows such reactions to happen.

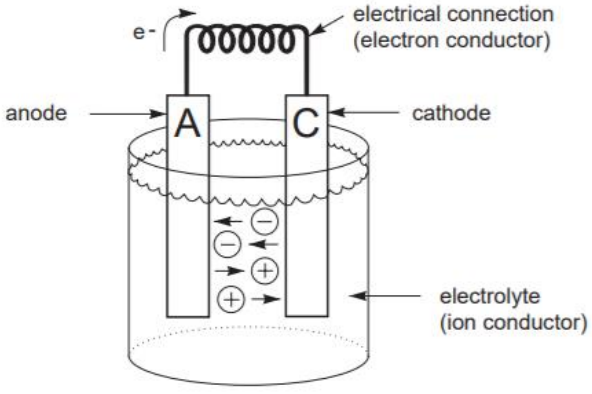

Figure 1.1 The components of an electrochemical corrosion cell [3].

The corrosion cell is driven by thermodynamics. The reactions between a metal and its environment happen spontaneously because they represent a lower energy

state for the element, and therefore a more stable form. From a thermodynamic point of view, a reaction is spontaneous if the change in Gibbs free energy is negative [1,3].

$$\Delta G<0 \tag{1.3}$$

Metals are commonly found in nature as oxides, minerals, or compounds because these forms are thermodynamically more stable. To obtain the metal of interest, a series of processes and the application of energy are needed to separate them (melting in a furnace, grinding, magnetic separation, electrolysis, etc.) depending on the metal and its properties. The result is commonly a pure metal in a metastable form that is prone to revert the process [4].

Considering a hypothetical reaction:

$$aA + mH^{+} + ne^{-} \leftrightarrow bB + dH2O \tag{1.4}$$

The change of free energy can be calculated from:

$$\Delta G = \Delta G^{0} + RTln\left[\frac{B^{b}(H_2O)^{d}}{A^{a}H^{+m}}\right] \tag{1.5}$$

Where, ΔG^{0} is the change of free energy in standard conditions, R represent the molar gas constant (8,3145 J/mol K), T is the temperature in K, and B, H_2O, A and H^{+} are the activities of the species that in the cases of diluted solutions can be approximate to the concentration (Henry's Law) [8].

For electrochemical reactions, the free energy of Gibbs (ΔG) can be related to the potential of the cell (E), as follows:

$$\Delta G = -nFE \tag{1.6}$$

Where, n is the number of electrons transferred in the cell reaction or half-reaction and F is the Faraday's constant (96480 C/mol).

Combining equations 1.5 and 1.6 results in a chemical-thermodynamical relationship that allows the calculation of the potential of a reaction (half-cell or full cell). This equation is known as the Nernst equation.:

$$\mathrm{E} = \mathrm{E}^0 + \frac{RT}{nF} ln \left[\frac{B^b (H_2O)^d}{A^a H^{+m}}\right] \quad (1.7)$$

Where, *E* is the potential of the reaction (can be of the full cell or half-cell), E^0 is the standard cell potential (which can be obtained from the galvanic series), *R* is the molar gas constant, *T* is the temperature (K), *B*, H_2O, *A* and H^+ are the activities of the species, *b*, *d*, *a* and *m* are the stochiometric coefficients [8]. Assuming *T* is room temperature (298 K), *R* and *F* are known numbers, and using logarithmic mathematical properties the equation 1.7 can be written as:

$$\mathrm{E} = \mathrm{E}^0 - \frac{0.0592}{n} log \left[\frac{B^b}{A^a}\right] - \frac{m}{n} 0.0592 pH \quad (1.8)$$

The last equation can be used to calculate the potential of the cell or even the half-cell (reduction or oxidation) if only the half-reactions are considered. It is important to note that the potential value calculated would describe an equilibrium state.

Applying the Nernst equation, Marcel Pourbaix studied the tendency of several metals to corrode in water. As a result of his investigation, he developed *E* vs. *pH* diagrams that show the equilibrium between metal and products in water. The most important contribution of these diagrams is the ability to identify whether a metal in an aqueous environment would be spontaneously immune, passivated, or corroded when the potential (*E*) and *pH* are known. These diagrams have become a valuable tool for scientists and engineers to quickly predict the possible outcome of a corrosive process when some data is available [4,8].

Figure 1.2 shows an example of the usefulness of the Pourbaix diagram for the Fe-H_2O system, and how it relates the products with the stability (corrosion, immunity, and passivation). In acidic pH, iron can transition from immunity to corrosion at specific potentials. For neutral and a wide range of alkaline pH, iron can transition from immunity to passivation and form an oxide film of Fe_3O_4 or Fe_2O_3, but corrosion is also possible at higher potentials. Similarly, another corrosive region can be seen at pH=14, so iron can be in immunity, corrosion, or passivity depending on the pH level.

Pourbaix diagrams are useful for assessing how a particular material will behave in aqueous environments, but they are not without limitations. Some of these limitations include [8]:

- The diagrams describe an equilibrium state, and most systems are not in equilibrium.
- Even when a metal is in the passivation zone, it does not mean that it is protected by its oxide film. The level of protection depends on the properties of the oxide layer and the electrolyte composition and concentration.
- The pH of the diagram may not consider the pH in restricted or confined areas such as pits or crevices, where the behaviour can be completely different due to a lack of oxygen in the microenvironment.
- They do not show any data related to the kinetics of the reaction, which is a very important engineering parameter.

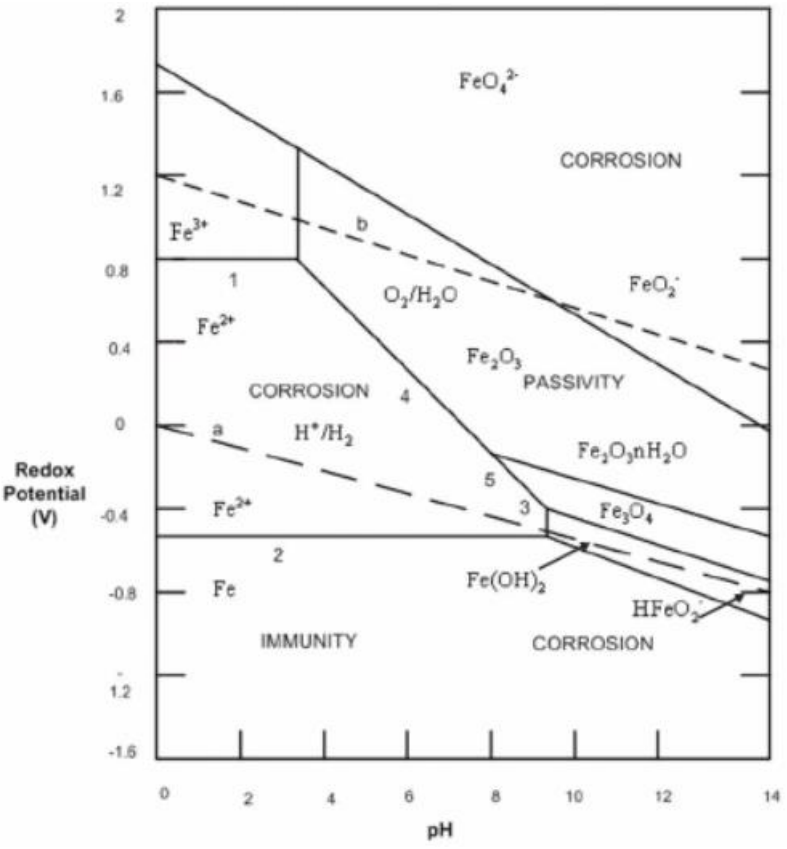

Figure 1.2 Schematic Diagram E vs pH for Fe in water [4].

1.2.2 Kinetics of corrosion

As mentioned previously the thermodynamic theories used to explain the corrosive process (Gibbs free energy and Nernst equation) do not take into account the kinetics, which has been defined as a critical point that cannot be dismissed.

As seen in previous examples, the reduction and oxidation reactions (REDOX) on the surface of the cathode and anode electrodes involve the movement of electrons. The movement of positive or negative electric particles generates an electric current, which can be measured and is proportional to the rate of the reaction. Normally, this current (I) is associated with the area of the electrode (A) and is known as current density (i), where:

$$i = I/A \tag{1.9}$$

The current density is a measure of how fast or slow the corrosion reaction is occurring. Such a parameter is affected by the temperature of the environment, the concentration of the electrolyte, and the presence of impurities. As the temperature increases, the current density increases, and as the concentration of the electrolyte increases, the current density also increases.

Considering that in an equilibrium condition the current generated by the oxidation reaction (i_a) is equal to the current generated by the reduction reaction (i_c) and the net flow of current is equal to zero [4].

$$i_{\text{Oxidation}} = i_{reduction} = i_0 \tag{1.10}$$

$$i_{Oxidation} - i_{reduction} = 0 \tag{1.11}$$

i_0 is the current density of exchange at the potential of equilibrium (E_0) and is commonly dependant of the reaction, the concentration of the reactants, the electrode, the temperature, and surface roughness [4].

The current density of corrosion (i_{corr}) is similar to i_0, with the difference being the nature of the cathodic and anodic reactions. For example, If the anodic reaction is:

$$M \rightarrow M^{2+} + 2e^- \tag{1.12}$$

The cathodic reaction might be:

$$2H^+ + 2e^- \rightarrow H_2 \quad (1.13)$$

At the corrosion potential E_{corr}, the rate of the anodic reaction is the same as the rate of the cathodic reaction, and therefore the current flow is the same in both directions. As a result, the net current is zero.

$$\text{At } E_{corr} \qquad i_{total} = i_a - i_c = 0 \quad (1.14)$$

$$i_a = i_c = i_{corr} \quad (1.15)$$

In non-equilibrium conditions, the net current is not equal to zero, and therefore a current flows from or to the electrode. The variation of the potential *E* caused by the application of an external current to the electrode is known as polarisation. The magnitude of the deviation is called the overpotential (η) and is directly proportional to the current density (*i*) [4].

- If the η>0, the overpotential applied is positive and a net anodic current flows in the electrode.
- If the η<0, the overpotential is negative and a net cathodic current flows in the electrode.

Polarising electrodes is a technique used to study the kinetics of the corrosive process. In fact, the dependency of the current density (*i*) when a variation of the potential (*E*) is applied is usually studied in the *E* vs. Log(*i)* charts. The use of these charts has helped to better understand the behaviour of materials with active/passive characteristics in different conditions (temperature, concentration, alloying elements, etc.) [1,4].

For metals with active/passive behaviour such as Fe, Cr, Ni, Ti, etc, the *E* vs Log(*i)* charts have shown how the variation in potential can change the state of the material (critical, active, passive, or transpassive). As shown in figure 1.3 [4].

The stability of the material is characterised by different zones, linked to the potential and current values highlighted in the figure 1.3. In the active region, the anodic and cathodic polarisation intersects at E_{corr}. If the material is polarised in the noble direction from E_{corr}, it is observed that the rate of metal dissolution increases as a function of the potential. The highest rate of corrosion is achieved at a

maximum current density, called the critical current density ($i_{critical}$), which is the maximum dissolution rate of the metal in the active region. The potential corresponding to $i_{critical}$ is called the primary passive potential (E_{pp}) and represents the transition from the active to the passive state for a metal [4].

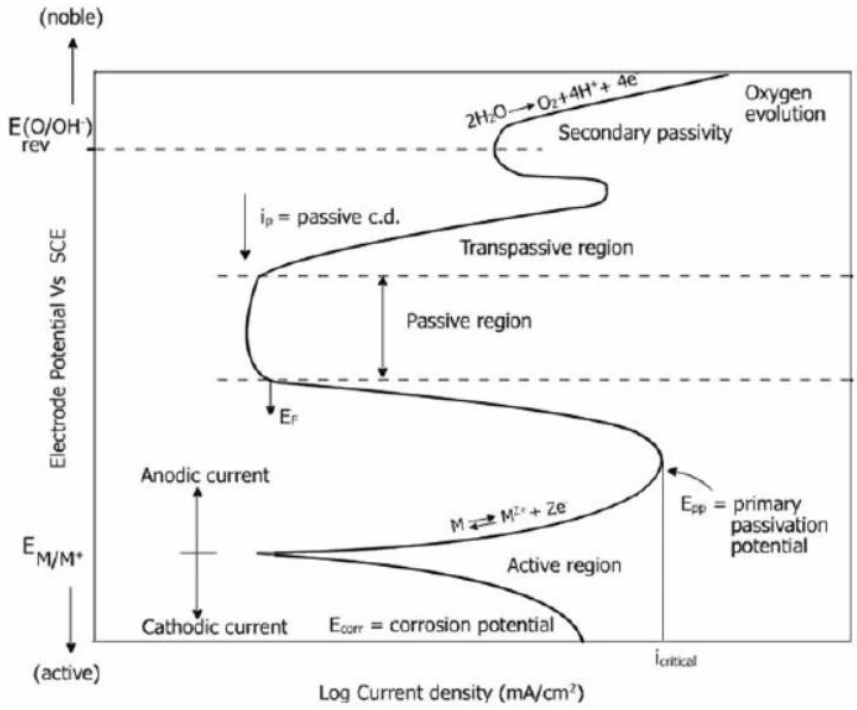

Figure 1.3 Schematic polarization diagram for an active – passive metal [4].

The current density (Log *i*) starts to decrease beyond E_{pp}, which is commonly attributed to the formation of a stable protective film on the surface (passive region). Beyond E_{pp} the current continues to decrease until it drops to a value several orders of magnitude lower than $i_{critical}$, which is known as passive current density (i_p), considered the minimum value of current to keep the metal in a passive state. The potential at which the current becomes virtually independent of potential and remains virtually stationary is called the flade potential (E_F) and represents the full passivity on the metal surface due to oxide film formation [4].

Once passivity has initiated, i_p is required to maintain the metal in a passive state. At i_p the metal dissolution occurs at a constant rate, and it is expected that the passive film gets thicker. However, surface films are heterogeneous and non-uniform, due to the presence of inclusions and other impurities, resulting in regions where the film becomes less thick. The dissolution of metal starts at these points,

and the process of film repair takes place only if the corrosion potential of the film exceeds the passivation potential E_{pp} [4].

If localised regions of the oxide film cannot be repaired, there is a sudden increase in the current density, this translates into a local dissolution of the metal due to breakdown of passive film on the metal surface. The potential where this takes place, is known as E_{pit} or pitting potential, and potentials above this value characterise a material in a transpassive region [4].

1.3 Localised corrosion

Localised corrosion is a type of corrosion where the attack occurs at localised sites on the metal surface. While the remaining area of the material shows little or no signs of corrosion. Examples of localised corrosion are: Intergranular corrosion, pitting and crevice corrosion.

1.3.1 Intergranular corrosion

Intergranular corrosion is the preferential corrosion at the grain boundaries (GB) of a metal when the material is in a specific corrosive environment. The GB acts as the joint between different crystalline grains, and a localised corrosive attack on them can dissolve material, resulting in a detriment of the mechanical properties such as strength and ductility. The phenomenon has been identified in several metals and alloys at different conditions, but it is commonly studied in austenitic stainless steels [1,4].

1.3.1.1 Intergranular corrosion in austenitic stainless steels

Stainless steels are classified based on their dominant microstructure, which can be ferritic, austenitic, martensitic, or duplex. Schaeffler diagrams offer a valuable tool to estimate the expected microstructure in a stainless-steel alloy. This is achieved by considering the combined effects of key alloying elements through the concept of nickel (Ni) equivalents and chromium (Cr) equivalents. These equivalents account for the austenite-stabilising and ferrite-stabilising tendencies of the elements. However, Schaeffler diagrams have limitations in their scope, excluding nitrogen as austenite stabiliser or the microstructural effect of cooling rates and thermal

history. Figure 1.4 illustrates an example of a Schaeffler diagram for some common stainless-steel grades [9].

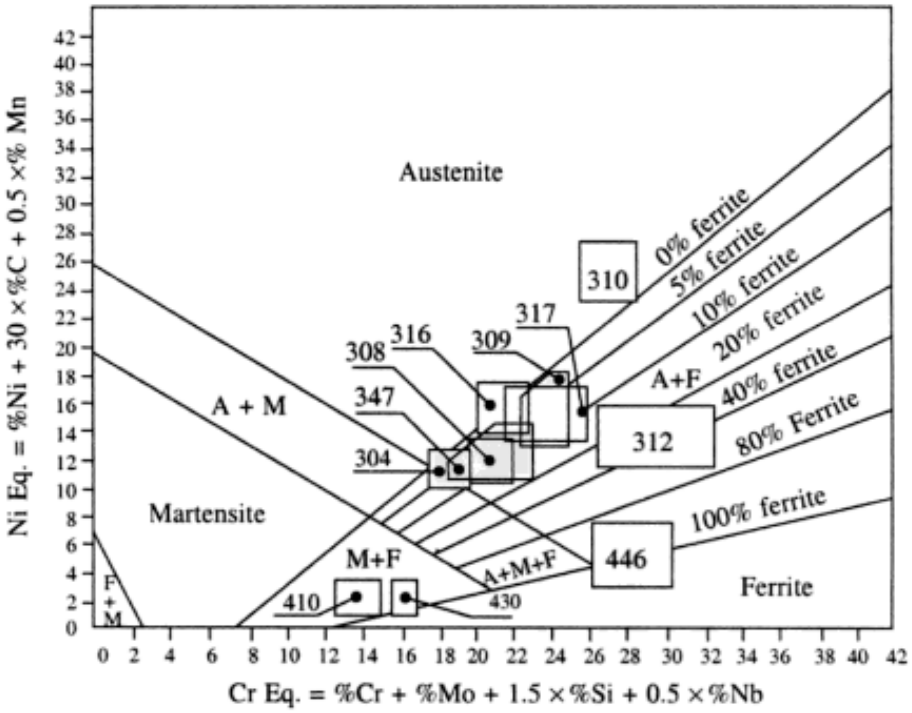

Figure 1.4 Schaeffler diagram for some common stainless-steel grades [9].

Austenitic stainless steels are widely used in several industries due to their diverse and versatile properties. Being non-magnetic, having good formability, good weldability, and high temperature resistance. Their austenitic (FCC, face-centred cubic) structure is tough and provides them acceptable ductility. They are also known for keeping their mechanical properties at elevated temperatures, which is a critical aspect in highly demanding facilities such as nuclear plants [10].

The typical compositions in an austenitic stainless steel contain between 16 and 25% chromium, which is the main responsible of their high corrosion resistance. In the same way, the nickel and nitrogen content help to stabilise the austenitic phase, which shapes most of their mechanical properties. Their different grades are known to withstand normal corrosive environments, and even the most corrosion-resistant grades can operate in boiling seawater conditions. However, over time it has been identified that they are susceptible to some types of localised corrosion in the presence of aggressive ions such as chlorides [Cl^-], which can lead to catastrophic and sudden failures such as Stress Corrosion Cracking [10].

It has also been identified that sensitisation promotes intergranular corrosion in austenitic stainless steels. Sensitisation is a phenomenon that occurs when the steel is heated and then slowly cooled down in a range of temperatures between 550-850 °C. At this temperature, carbon diffuses towards the grain boundaries, promoting the formation of $M_{23}C_6$, where M might be chromium. The precipitation of chromium carbides makes the surrounding areas ''depleted'' of the element (Cr) and therefore susceptible to corrosion. For this reason, it is very important to control heat treatments in susceptible alloys or the heat affected zone (HAZ), a product of weld joints [4,10].

It has been discovered that the addition of certain alloying elements like Niobium or Titanium mitigate the susceptibility to intergranular corrosion. Pardo et al. [11] showed how increasing the quantity of Ti in stainless steel (SS) 316 grade promotes better intergranular corrosion resistance. This behaviour was explained due to the formation of Titanium carbides, which reduces the production of $Cr_{23}C_6$. In addition, a higher content of chromium and a tight content of the carbon helps to control this phenomenon [10,11].

1.3.2 Pitting corrosion

Pitting corrosion is a localised type of corrosion where a small area of the metal surface is attacked preferentially, forming small cavities or pits while the rest of the surface shows no signs of corrosion. The pit may propagate through the entire wall thickness of the material, leading to leaks or failure of components despite a low weight loss [1,4]. This behaviour makes pitting one of the most dangerous types of corrosion.

Pits may have several characteristic sizes and shapes (circular, square, pyramidical and hexagonal), but the actual shape beneath the surface may be quite different. For this reason, it is often recommended to cross section the pit and corroborate its shape and depth. Variations of cross-sectioned pits are shown below in figure 1.5.

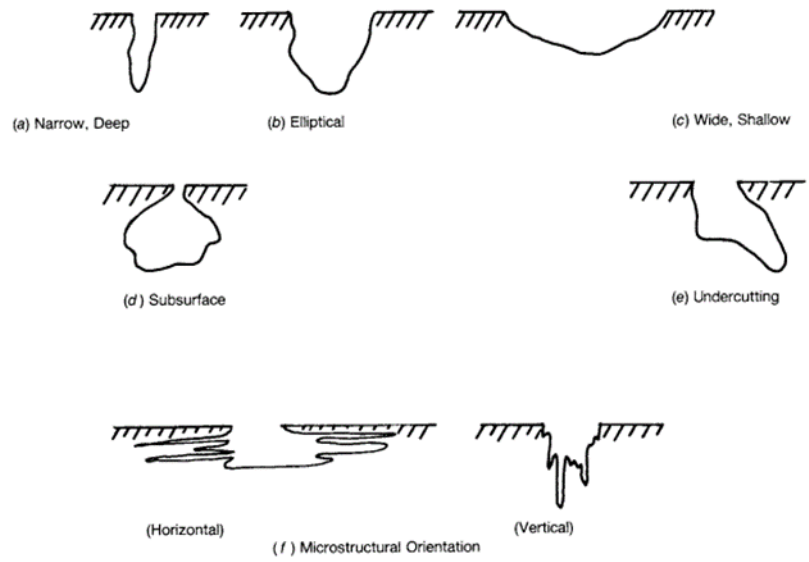

Figure 1.5 Schematic diagram of the various shapes of pits shown in cross section [12].

As mentioned previously, pitting corrosion occurs when the potential is above E_{pit}. This value depends on the concentration of aggressive ions (such as chlorides), and it has been reported that higher concentrations of these elements will result in a lower pitting potential, making the material susceptible to this phenomenon [13].

Alloying elements also play a major role in the pitting corrosion potential. It is known that molybdenum (Mo), chromium (Cr), nickel (Ni), vanadium (V), silicon (Si), nitrogen (N), silver (Ag), and other elements can increase the pitting potential. In the same way, the presence of ions such as hydroxide (OH^-), sulfate (SO_4^-), hypochlorite (ClO^-), and carbonate (CO_3^-) in the environment can raise E_{pit}. It has also been seen that the addition of nitrates and chromates in solutions with chlorides inhibits the pitting process [14].

The temperature also influences the kinetics. As a rule, higher temperatures translate into higher reaction rates, and therefore, accelerates the pitting process.

In the same way, heat treatment and cold working can change the microstructure and properties of stainless steels. Their effect on pitting resistance depends on the direct consequences of these processes. For example, if they promote chromium depletion, it would be expected that the material would have a weaker response the pitting process [4,10,11].

Another factor that has been identified is the stagnant condition of the electrolyte, which can lead to a change of concentration and pH and contribute to the formation of pits. This is because a difference in environments can create a concentration cell, which can start the pitting process by rupturing the passive film and creating a small anodic zone [1,4].

The pitting process can also start at grain boundaries, so the grain size is a factor to consider. In fact, A. Abbasi Aghuy and others [15], reported that grain size reduction increases metastable pit stability for austenitic stainless steel 304L.

1.3.2.1 Pitting corrosion initiation and growth

The pitting corrosion phenomenon is typically initiated by a localised rupture of the oxide protective film on the surface of the metal. This can be caused by mechanical damage, heterogeneities on the surface, or the presence of precipitates and inclusions [1,4].

In addition, the pitting process is related to the presence of aggressive ions such as Cl^-, Br^-, I^-, etc in the electrolyte. Several authors have reported that chloride ions influence the breakdown of the metal passivity by displacing oxygen and forming hydroxy-chloride metal complexes, increasing the solubility of the surface oxide film [16,17]

Fontana and Greene [18] developed a qualitative model that describes crevice corrosion initiation and propagation of stainless steel in neutral halide solutions. The model is also accepted as a mechanism to explain pitting corrosion in metals and alloys. It can be divided into four stages described below, and illustrated in figure 1.6 [19]:

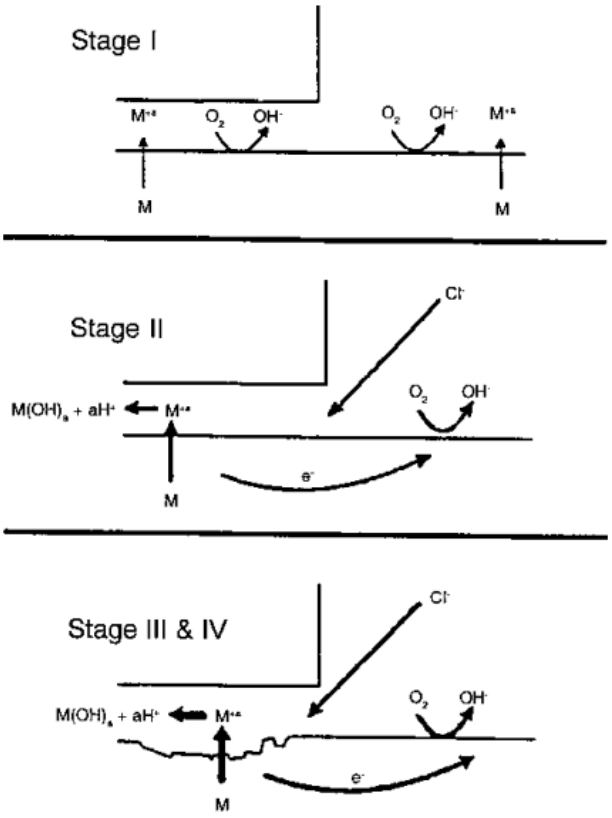

Figure 1.6 Schematic of Fontana and Greene model for crevice corrosion initiation of stainless steels in aerated Cl^- solution [19].

- Stage I: Once the pitting is started due to the rupture of the passive film, the alloying elements will dissolve stoichiometrically in proportion to their composition in the metal (equation 1.16). For example, in stainless steel Fe, Ni, and Cr will dissolve into the solution constituting the anodic reaction. To keep the equilibrium, the system would require a cathodic reaction, such as oxygen reduction (equation1.17), which occurs both inside and outside the pit. However, due to restricted diffusion towards the occluded site, oxygen becomes depleted inside the cavity, creating the physical separation of anode and cathode.

$$M \rightleftharpoons M^{2+} + 2e^- \quad (1.16)$$

$$O_2 + 2H_2O + 4e^- \rightleftharpoons 4OH^- \quad (1.17)$$

- Stage II: The continuous dissolution and accumulation of cations (Fe^{2+}, Cr^{3+}, Ni^{2+}, etc) inside the pit is balanced by the electromigration of anions from

the electrolyte. The most common anions are chlorides due to its high mobility, size, and availability in the bulk solution. The Cl^- will combine with the metal ions resulting in complex products (equation 1.18), which will be quickly hydrolysed (equation 1.19). The hydrolysis lowers the pH inside the pit through the production of hydrogen ions. This will eventually become a self-sustained process because a low pH will increase the passive current, promoting the Cl^- migration, increasing the rate of hydrolysis, translating into further decreases in pH inside the cavity.

$$2Cl^- + M^{2+} \rightleftharpoons MCl_2 \quad (1.18)$$

$$MCl_2 + 2H_2O \rightleftharpoons M(OH)_2 + 2H^+ + 2Cl^- \quad (1.19)$$

- Stage III: The environment inside the pit is characterised for a very low pH and a very high chloride concentration. In fact, Experiments carried out by Turnbull and Gardner [20] reported pH≤1 inside an artificial crevice. While Salamat et al. [21] mentioned that to develop a pH of 0.3 inside a crevice the Cl^- concentration will need to be >3 M to maintain the charge neutrality. Under such challenging conditions the passive layer of stainless steel will not be able to remain passive and the material will dissolve in a localised region.
- Stage IV: The pit propagation is stable due to the formation of a small anode zone on the surface characterised by metal dissolution, surrounded for a larger cathode area. The difference of areas (illustrated in figure 1.7) affects the rate of the reaction, leading to a sharp dissolution of the metal in the pit. This is because the corrosion products are formed in the anode and cannot spread on the cathode.

Furthermore, several researchers have found an empirical relation to describe the kinetics of pit growth, as can be seen in equation 1.20 [22].

$$y = kt^n \quad (1.20)$$

Where y is the pit depth, t is time, k is a constant dependent upon material and environment, and n is a numerical constant.

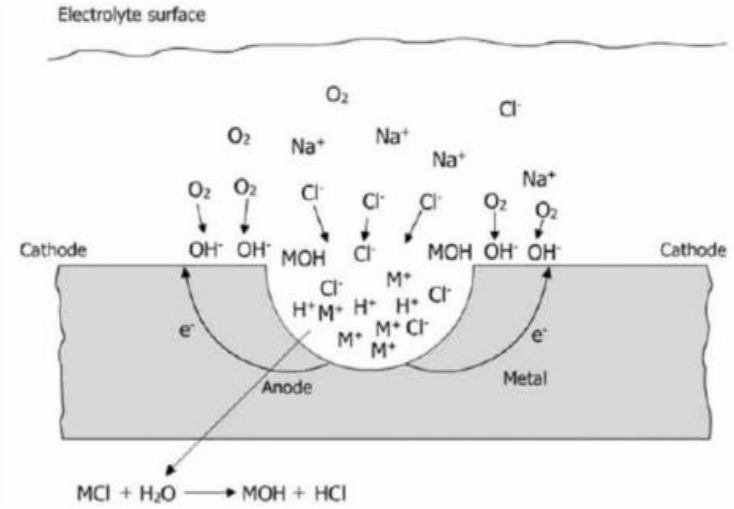

Figure 1.7 Schematic of a corrosion pit on a metal in an environment rich in chloride ions [4].

1.3.2.2 Effect of inclusions in the pitting process of steels

It has been demonstrated that heterogeneities on the surface, such as inclusions, play a major role in the initiation of pitting corrosion, increasing the probability of its occurrence. In the case of steels and stainless steels, MnS inclusions have been identified as preferential sites for pit nucleation and growth.

However, there is not agreement on the initiation mechanism involving the electrochemical reactions. Several authors have proposed different theories to support their observations [23-26]. The most notable of them can be summarised as follows:

- Eklund [23] observed the formation of elemental sulphur (S) and suggested that an initial dissolution of MnS would lead to the formation of sulfate (SO_4^{2-}) and H_2S. Subsequently, the anodic dissolution of H_2S would translate into the precipitation of S.
- Wranglen [24] proposed that the MnS dissolution is part of the anodic reactions inside the pit, which would lead into the formation of hydrogen sulphide (H_2S) and Mn^{2+} ions.
- Castle and Ke [25], considered the formation of HSO^{3-} from the oxidation of MnS and water, and the subsequent precipitation of sulphur once the HSO^{3-} combines with hydrogen ions in the solution.

- Lott and Alkire [26] suggested that the electrochemical dissolution of MnS produces thiosulfate ions ($S_2O_3^{2-}$).

Despite the lack of consensus on the mechanism by which the pitting process is initiated, it is agreed that the anodic dissolution of MnS will generate changes in the solution next to the inclusion, which could lead to the rupture of the passive film on stainless steel and the formation of a pit.

In addition, the size and orientation of the inclusions seem to affect the pitting process. Webb et al. [27] observed that large and shallow inclusions failed to initiate the pitting process, while narrow and deep inclusions were successful.

1.3.3 Stress Corrosion Cracking (SCC)

Stress Corrosion Cracking (SCC) is a type of localised corrosion that occurs when a material is subjected to tensile stress in a corrosive environment. It is characterised for the initiation and quick propagation of cracks in a chemical environment. Leading to sudden and unexpected failures of the material.

The three main factors that are necessary for SCC to occur are [1,3,4]:

- A corrosive environment: The environment must contain aggressive ions, such as chlorides, bromides, iodides, or thiosulfates. The concentration of these ions is also important, as higher concentrations increase the risk of SCC.
- A material susceptible: The material chemical composition, microstructure and heat treatment conditions would influence the phenomenon.
- Tensile stress: The material must be under tensile load, which can be applied due to service conditions, or residual, product of weld joints, cold work, or machining. It has been observed that the material may fracture at lower stress value than the yield strength and that compressive stress may reduce the effect of SCC.

There are three main types of SCC [1,3,4]:

- Chloride stress corrosion cracking (Cl-SCC): This is the most common type of SCC. It occurs in austenitic steels under tensile stress, in the presence of chloride ions, oxygen, and a specific temperature.
- Caustic stress corrosion cracking (C-SCC): This type of SCC occurs in steels in caustic environments where the hydroxide concentration is high. It has been reported in Inconel alloy tubes in alkaline solutions.
- Sulphide stress corrosion cracking (S-SCC): Occurs in steels in hydrogen sulphide environments. It is commonly reported in the oil drilling industry.

SCC cracks may initiate from surface irregularities, localised corrosion sites, or even from intergranular corrosion. The crack propagation reported can be intergranular (through the grain boundaries) or transgranular (across the grains). The type of crack propagation can vary depending on the material, environment, and stress level. For example, some researchers have reported in austenitic stainless steels a change of propagation (intergranular to transgranular or vice versa) when the temperature is increased or when the material is thermally sensitised [4,28].

1.3.3.1 Study of SCC in different types of steels

Several types of steels have been reported to be susceptible to SCC. These alloys are key for several industries where SCC could be a concern due to service requirements. Therefore, it is important to improve the understanding of this phenomenon to develop processes or preventive measures that can help to mitigate, identify, or avoid SCC.

Several researchers have taken different approaches to study SCC in different types of steels. They have found relevant parameters that shed some light on the variables and conditions that contribute to SCC. Some of the techniques used and findings can be summarised below:

- Alyousif and Nishimura [28], investigated SCC and hydrogen embrittlement (HE) for austenitic stainless steels 304, 310, and 316 in boiling saturated $MgCl_2$ solutions using a constant load method under different test temperatures, applied stress, and sensitisation. They reported the time to failure (*tf)* to characterise the performance of the materials and proposed a

mathematical model to predict the (*tf)* in chloride solution. Additionally, they observed that the type of crack propagation could change from intergranular to transgranular for SS 304 when the temperature is increased. While SS 316 can develop a mixture of intergranular and transgranular at a range of temperature, and alloy 310 showed a transgranular mode. They suggested that the intergranular propagation in 304 and 316 is the result of HE due to strain-induced formation of martensite in grain boundaries, while transgranular cracking took place by propagating cracks nucleated at slip steps by dissolution. They also mentioned that sensitised samples had a lower fracture susceptibility due to SCC and HE.

- Scatigno et al. [29], studied the effect of salt loading on the crack density for 5% pre-strained SS 304L samples under 60MPa uniaxial stress, using a 4-point bent beam, at 90°C, 70% RH for 480h. The researchers used different salt loads of $MgCl_2$ sprayed on the surface to induce an environment rich in chloride ions and found a direct correlation between density of cracking and a range of salt load. One important finding in this research was that the highest concentration of salt did not correlate with the highest density of cracks. The authors suggested that high levels of salt loading could increase the wet film thickness, limiting oxygen diffusion to the pits and preventing SCC initiation.
- Galvan-Martinez and others [30], studied the API X70 (high-strength low-alloy HSLA) pipeline steel exposed to a synthetic soil solution at room temperature and atmospheric pressure through slow strain rate tests (SSRT) while electrochemical noise (EN) measurements were carried out. They reported the highest corrosion rate while the material was in plastic deformation (before fracture).
- Bosch and colleagues [31], tested tapered samples of a developed high-Si duplex stainless steel, which simulated the grain boundary composition in neutron-irradiated stainless steels used in the Pressurised Water Reactors (PWR) and the Alloy 182 (which is a material present in many dissimilar metal welds in operating PWR). The tapered geometry allows to test a stress

gradient obtained through the gauge length, and therefore is possible to obtain a stress threshold for SCC in the initiation stage in a single sample.

- Zhou et al. [32], investigated the effect of grinding on the SCC response of 304L stainless steel in a in boiling saturated $MgCl_2$ solution. The samples were under external load applied using a four-point bent beam and the surface was grinded parallel or perpendicular to the load direction. The authors performed x-ray diffraction to measure the residual stresses due to the grinding operation. The results showed cracks initiated by a high level of tensile residual stress in the ground samples. They also mentioned that specimens ground along the loading direction were more susceptible and perpendicular more resistant to SCC.

Looking on the findings of these studies, it is evident that the synergistic negative effect of tensile loads and environment with aggressive ions in different steel alloys can lead to SCC. However, these research projects failed to provide a clear explanation on the role of the stress in the initiation of the SCC phenomenon.

1.3.3.2 The role of applied stress in the initiation of SCC

Research projects focused on the pit initiation under strain is scarce in the literature, explaining why the role of strain in the initiation of SCC remains unclear. A selection of the most relevant investigations on this topic in austenitic stainless steel 304 is summarised below:

- Isaacs [6], used the in-situ scanning vibrating electrode technique to study the relation between potential fluctuations and the initiation of intergranular stress corrosion cracking in diluted thiosulfate solutions for stressed and thermally sensitised 304 SS specimens. He reported that a sudden and extended potential decrease is related to the localised corrosion initiation and cracking propagation. Additionally, such corrosion sites were identified by emerging anodic current density peaks, while cracks that had repassivated did not act as reinitiation sites. His studies demonstrated that the in-situ scanning vibrating electrochemical technique can be used to

track the development of SCC by measuring the current distribution on surface.

- Suter and colleagues [33], used microelectrochemical cells to study pit initiation on three 304 SS samples with different sulphur and MnS inclusion content. The experiments were carried out in 1 M NaCl solutions with and without applied stress. They observed that polarised samples without inclusions did not exhibit pitting behaviour, even for samples under strain. However, areas tested with MnS inclusions showed stable pitting at about 400 mV; showing that applied stress shifted the pitting potential to values 150 mV more negative. The pitting process was also affected by the inclusion form and size. For large deep inclusions, active pitting was obtained, while shallow MnS inclusions showed metastable behaviour and did not initiate stable pitting. The dissolution of shallow MnS inclusions did not form a deep microcrevice between the MnS and the stainless-steel matrix. However, under applied stress, cracks formed within the shallow MnS inclusion and active pitting occurred. Their findings are summarised in figure 1.8.

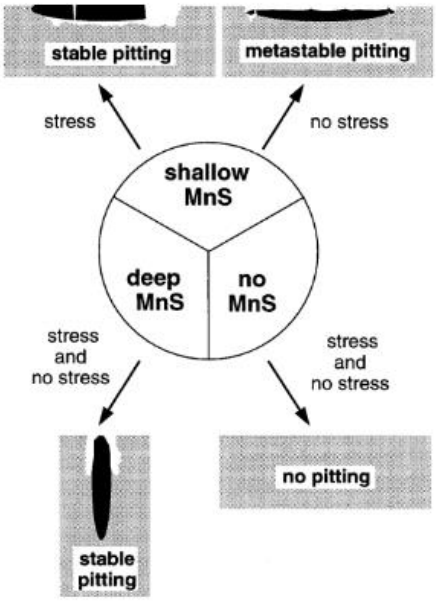

Figure 1.8 Types of pitting observed at MnS inclusions on 304 SS in 1 M NaCl with and without applied stress reported by Suter and others [33].

- Tokuda et al. [34], focused their research on the initiation of pitting in sensitised 304 SS, emphasising the synergistic effect of applied stress, Cr-depletion at grain boundaries, and inclusion dissolution. Their research was conducted by immersing samples with and without stress applied in 4 M $MgCl_2$ solution. They found that the occurrence of pitting would depend on the area exposed for non-stressed samples, while pitting initiated regardless of the area exposed for the stressed specimens. MnS inclusions were the preferred site for pits to develop. The authors also reported that the dissolution rates of MnS inclusions and sensitised grain boundaries were accelerated by applied stress when specimens were polarised.
- Shimahashi and colleagues [35], based their investigation in the effect of applied stress on the pit initiation behaviour of (Mn,Cr)S inclusions in 304 SS using microelectrochemical measurements. They found that under anodic polarisation, the MnS was selectively dissolved, and the inclusion changed to a CrS covered by an Cr-oxide film. In the same way, they found that stable pitting did not always occur when no-stress was applied, while the behaviour shifted to stable pitting in the potential range of the MnS dissolution once the specimens were under applied load. The authors also observed micro-cracks perpendicular to the tensile load and believe that such cracking initiated by the formation and rupture of the oxide film on the inclusion. A schematic of the theory described by the authors is shown in figure 1.9.
- Moore et al. [36], carried out investigations taking a new approach in the SCC study, focusing on the in-situ observation of crack initiation at the nanoscale. They used a high-speed atomic force microscopy (HS-AFM) on SS 304 samples which were loaded using a 3-point strain rig immersed in a rich chloride solution. The results reported by the authors showed an uplift of grain boundaries before cracking, suggesting that the cracking mechanism has a subsurface contribution. The investigation also revealed analysis by atom probe tomography of a crack tip which showed a layered oxide composition at the surface of the crack walls. These results had not been

reported before and open a window for new in-situ mapping of SCC during the initiation and propagation stage using diverse techniques.

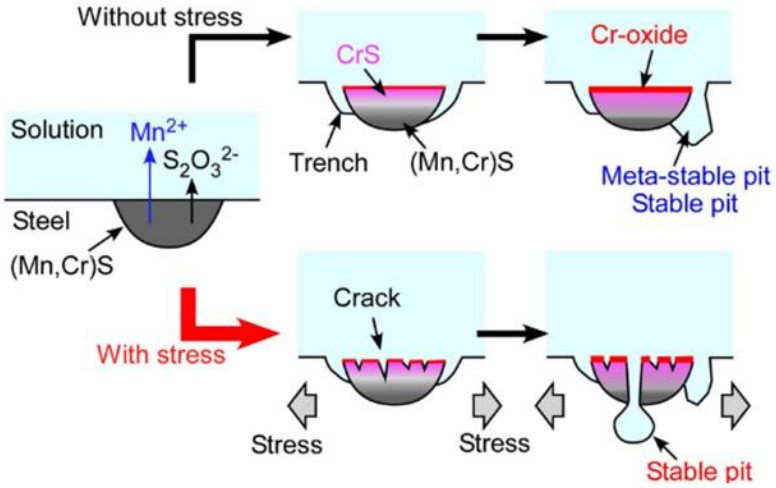

Figure 1.9 Schematic illustration of pit initiation mechanisms at (Mn,Cr)S inclusions with and without applied stress [35].

The findings of these studies suggest that applied stress plays a significant role in the initiation of SCC in 304 SS. However, the exact mechanism by which stress promotes pitting and crack initiation is still not fully understood. The use of the SVET to investigate pit initiation and propagation on a well-studied alloy like AISI 304, by comparing localised corrosion behaviour in both strained and non-strained samples, for specimens in both sensitised and annealed condition could contribute to the understanding of this phenomenon not just in austenitic steels, but in other alloys used in high impact industries such as the nuclear energy industry.

1.4 Nuclear industry in the UK

The nuclear power industry in the UK provided 16.1% of the electricity consumed in the country in 2020, making it the third-largest source of energy after natural gas and wind & solar renewables [37]. The history of nuclear power in Britain dates back to 1956, when the first plant at Calder Hall began operations. Since then, 19 nuclear power stations have been in service, 2 are currently under construction, and a few more are under consideration. However, 11 of the 19 plants have already closed, and 8 are expected to complete their life cycle between 2023 and 2035 [38].

As shown in table 1.2, the 19 nuclear power stations built in Britain can be divided into three different types of reactors: 11 Magnox reactors (which have all ceased operations), 7 Advanced Gas-cooled Reactors (AGRs), and 1 Pressurised Water Reactor (PWR). The AGRs and PWRs are still in service, and the AGR is the predominant reactor type, with a combined generation capacity of over 8,000 MW.

1.4.1 Advanced Gas-cooled reactors (AGR)

The Advanced Gas-cooled reactor (AGR) is a type of nuclear reactor that uses slightly enriched uranium dioxide (UO_2) as fuel in the form of cylindrical pellets, encapsulated within a bespoke grade of austenitic stainless-steel cladding tube, in a form known as fuel pin. The AGR is also characterised by using carbon dioxide gas (CO_2) as coolant to transfer heat from the reactor to the boilers, instead of water like the Pressurised Water Reactor (PWR) [39].

The fuel element of an AGR (figure 1.9) consists of 36 fuel pins surrounded by a graphite sleeve. The graphite acts as a moderator, decreasing the energy of what are known as fast neutrons to thermal neutrons, suitable for energy production. Depending on the AGR reactor, a different number of elements (seven or eight) are stacked and connected to form the 'stringer' which is loaded into the reactor [5,39].

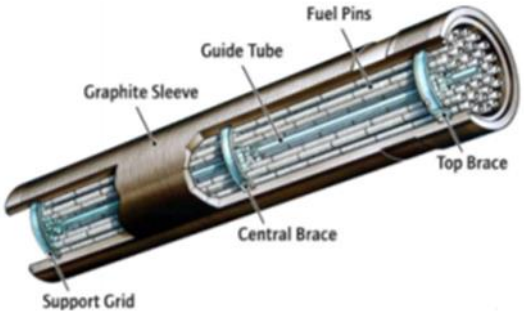

Figure 1.10 Fuel element example [5].

The fuel pins are subject to high temperatures in the reactor, and depending on their location in the element, they can reach temperatures between 350°C - 825°C in a CO_2 environment. Despite the cladding being a highly corrosion resistant alloy in a high temperature environment, the combined effect of a neutrons flux and temperature, produces a phenomenon known as Radiation Induced Segregation (RIS). RIS results in a depletion of chromium at grain boundaries, like the

sensitisation effect on austenitic stainless steel, which can make the cladding susceptible to different corrosive processes, and therefore compromise the integrity of the cladding [5,39,40].

Table 1.2 Nuclear power stations in the UK (1956 – 2035) [38].

Power Station	Opening Date	Closure Date	Installed Capacity (MW)	Current Status	Reactor Type
Calder Hall	1956	2003	220	Closed	Magnox
Chapelcross	1959	2004	196	Closed	Magnox
Berkeley	1962	1989	276	Closed	Magnox
Bradwell	1962	2002	242	Closed	Magnox
Hunterston A	1964	1989	180	Closed	Magnox
Dungeness A	1965	2006	450	Closed	Magnox
Trawsfynydd	1965	1991	470	Closed	Magnox
Hinkley Point A	1965	2000	500	Closed	Magnox
Sizewell A	1966	2006	420	Closed	Magnox
Oldbury	1967	2012	434	Closed	Magnox
Wylfa	1971	2015	980	Closed	Magnox
Hinkley Point B	1976	2023	1061	Operational	AGR
Hunterston B	1976	2023	1074	Operational	AGR
Hartlepool	1983	2024	1207	Operational	AGR
Heysham I	1983	2024	1179	Operational	AGR
Dungeness B	1983	2028	1120	Operational	AGR
Heysham II	1988	2030	1254	Operational	AGR
Torness	1988	2030	1250	Operational	AGR
Sizewell B	1995	2035	1216	Operational	PWR
Hinkley Point C1	2025	2086	1630	In construction	EPR
Hinkley Point C2	2026	2087	1630	In construction	EPR
Sizewell C	2030 - 2035	2090-2095	3340	Proposed	Hualong one
Bradwell B	2030 - 2035	2090-2095	2300	Proposed	Hualong one

1.4.1.1 Fuel Cladding material in AGR

The nuclear fuel cladding material, as previously mentioned, is a bespoke stainless-steel grade designated as 20Cr-25Ni-Nb (detailed chemical composition can be seen

in Table 1.3). This alloy exhibits an austenitic microstructure, which can be verified with the Schaffler diagram (figure 1.4), using the nickel (Ni) and chromium (Cr) equivalent concept. The niobium (Nb) acts as a stabiliser for the austenitic matrix, producing NbC precipitates, which enhance the material's high-temperature mechanical properties, making it resistant to creep [40].

Table 1.3 20Cr-25Ni-Nb stainless steel typical composition (wt%) [41].

Cr	Ni	N	C	Mn	Si	S	Nb	Ta	Fe
20.12	25	0.016	0.049	0.62	0.57	0.004	0.7	0.006	Balance

During service, the cladding materials in AGRs interact with a high CO_2 (coolant) environment at a range of high temperatures, that depending on the location of the element in the stringer can reach 350 °C – 825 °C. This can lead to different types of oxidation processes in the material, including [5]:

- Elements irradiated at temperatures higher than >700 °C: A continuous and well-adhered chromia layer grows on the surface.
- Elements at the lowest temperature regions of the stringer, around 350-400 °C: An iron-rich oxide film is formed.
- Elements at intermediate temperatures (between 350 °C - 700 °C): Both oxides can grow, with a thinner chromium layer progressively forming, which has protective properties and limits the cladding oxidation rate.

In addition of the oxidation process, radiation induced segregation (RIS) has been observed in AGR cladding materials. RIS is a non-equilibrium effect, that occurs when a neutron flux at high temperature generates atomic displacement of interstitial atoms and forms vacancies. Such defects in the crystal lattice sequentially diffuse to the grain boundaries, exchanging positions with alloying elements, which is known as the inverse Kirkendall effect.

The RIS process leads to the redistribution of alloying elements at the microstructure level, and its dependant on the elements' diffusivity. Cr and Fe

atoms have higher diffusivity rate, and therefore become depleted at grain boundaries. On the other hand, elements with a lower diffusivity rate such as Ni and Si, become enriched at grain boundaries [5,42].

It is well known that the role of Cr in austenitic stainless steel is to provide a non-porous, self-healing, stable and adherent chromium oxide (Cr_2O_3) layer which acts as a barrier between the material and the surroundings [43]. However, the depletion of Cr at grain boundaries due to RIS mirrors the effect of sensitisation, potentially leaving the GB sites with a composition lower than 12 wt. %, which has been reported to diminish the capability to produce a stable chromium oxide passive film. Resulting in a material prone to intergranular corrosion [44].

Localised corrosion in austenitic stainless steels has been linked to aggressive ions such as chlorides [3,4,45]. Whilst chlorides, are not an issue for the cladding integrity during reactor operation, they are tightly controlled in spent fuel ponds. Once the burn-up time has been completed (typically 5 years), spent fuel is stored in cooling ponds for a minimum period of 100 days, where water chemistry control is maintained at ≤0 5 ppm Cl^- at an elevated pH of 11.4. In demineralised water, at higher pH IGC has been witnessed for fuel irradiated >15 $GWd \cdot t^{-1}$ [5,46-48]

1.4.1.2 Spent nuclear fuel cladding alloy and concerns on its integrity

Given that spent nuclear fuel cladding is the primary barrier for fission product release from spent fuels, it is important that it maintains its structural integrity over the operational period. In the past, spent fuel cladding was typically shipped to the Thermal Oxide Reprocessing Plant (THORP) at Sellafield in Cumbria to be reprocessed. In this plant uranium could be recycled to form new fuel and any highly active fission products would be disposed as high-level waste. The UK decided that once existing contracts were completed, reprocessing operations would cease in 2018 at THORP with the plant transitioning into a long-term pond store for spent AGR fuel [43,44].

As a result, AGR spent fuel is currently being stored in long-term pond storage. However, these ponds can contain traces of aggressive ions, which can make localised corrosion possible. Immersion tests on whole pins showed that the

samples failed within 80 to 350 days at chloride concentrations between 1 and 100 ppm [48]. It is known that after years of reactor service, the pellets swell, leading to a hoop stress on the cladding wall, and the fuel cladding can have residual stresses arising from cold work during manufacture. These have the opportunity to create a driving force for Stress Corrosion Cracking if sufficiently sensitised in the presence of sufficient aggressive anions [49].

However, in the early 1980s, several investigations were carried out to identify a suitable corrosion inhibitor to be added to the ponds, being Sodium Hydroxide (NaOH) selected for its efficiency. Several experimental investigations on the effect of NaOH in cladding materials have shown that it can be effective in inhibiting the corrosive process when added to the electrolyte, specifically when dosing the pH between 11.4-11.5 and the temperature is not higher than 60 °C. The addition of NaOH to raise the pH has provided a safe management of the SNF for over 20 years and is currently the preferred technique to ensure the integrity of AGR spent fuel pins [5,40,50,51].

In the future, it is expected that spent fuel stocks will rise from 1,000-2,000 tonnes to 5,000-6,000 tonnes by 2040. Currently, the SNF is stored in long-term pond storage, until a Geological Disposal Facility (GDF) is built. NaOH dosing of pond water has been demonstrated as a safe way of managing SNF cladding integrity, however, there is insufficient operating experience past three decades, and it is expected that long term storage may be required until 2075 [5, 48].

As mentioned previously, the main concern for spent nuclear fuel (SNF) integrity is the detrimental effect of radiation-induced sensitisation (RIS) on 20Cr/25Ni/Nb cladding alloy. It is known that RIS makes the grain boundaries significantly more susceptible to localised corrosion than the grains. Recent studies published by Clark et al. [52], confirmed intergranular corrosion (IGC) attack in the sensitised condition of this alloy, suggesting that NbC particles in the matrix can form preferential anodic metal dissolution sites, creating initiation points for IGC. Even though the results are not conclusive, it is believed that these carbides can induce micro-galvanic coupling between NbC and the austenitic phase, resulting in the initiation of the localised attack observed.

To gather additional information on the possible galvanic effect between the cladding alloy and its Cr-depleted grain boundary, this research project will study coupons made of a simulated sensitised grain boundary material electron beam welded to the 20Cr/25Ni/Nb stainless steel. The experiments will focus on the relative nobility of the regions (including the weld between the two different alloys) and its relationship with the corrosion behaviour when the coupons are immersed in a chloride-rich solution while studied with the scanning vibrating electrode technique (SVET).

Chapter 2

2. Experimental Details

2.1 Stainless steel AISI 304 specimens and conditions

2.1.1 Material

Austenitic stainless-steel grade AISI 304 sheets of 10 cm x 10 cm and 0.914 mm thickness were provided by Goodfellow Cambridge LTD, supplied in annealed condition. The standard chemical composition reported by the supplier can be found in table 2.1, it is important to highlight that the exact C content is unknown.

To study the sensitisation effect on this material and compare it with the as received (or annealed) condition, some of the AISI 304 sheets were heated at 600 °C for 50 hours followed by water quench. Such heat treatment promotes the precipitation of chromium carbides at grain boundaries [50], allowing a comparison of the corrosion behaviour of the sensitised and as-received materials to be made.

To reveal the microstructure of the material, electrolytic etching was carried out. This was done using an ATM Kristall 680 apparatus, applying a DC potential of 15 V for a period of 75 seconds while the samples were immersed in oxalic acid 10% (w/v) [53].

Table 2.1 AISI 304 composition (wt%) - provided by Goodfellow Cambridge LTD.

Cr	Ni	N	C	Mn	Si	S	P	Fe
17-19.5	8-10.5	≤0.11	≤0.07	≤2.0	≤1.0	≤0.015	≤0.045	Balance

2.1.2 Environment

To promote the localised corrosion behaviour without needing to externally polarise 304 SS specimens, aqueous $MgCl_2$ solutions of different concentrations were chosen as the corrosive environment. To prepare the solutions, Sigma-Aldrich

M2670 magnesium chloride hexahydrate BioXtra ≥99% was used, dissolved in 18 MΩ.cm distilled water. The solutions prepared had four different concentrations: 1 M, 2 M, 3 M, and 4 M.

2.1.3 Tensile load

A three-point strain rig was designed and made of AISI 316 (figure 2.1 and figure 2.2) to apply a tensile load on the samples. The rig produces a deflection on a rectangular specimen once the bolts are screwed down, where the relationship between deflection and the tensile load on the outer surface can be estimated using equation 2.1, which is obtained from ASTM G39 [54]. However, such a relationship only remains valid in the elastic regime of the material and therefore values of stress above the yield point cannot be calculated accurately using this equation [54]. AISI 304 sheets (both as received and thermally sensitised) were cut to size and subsequently machined to create samples which would fit in the strain rig.

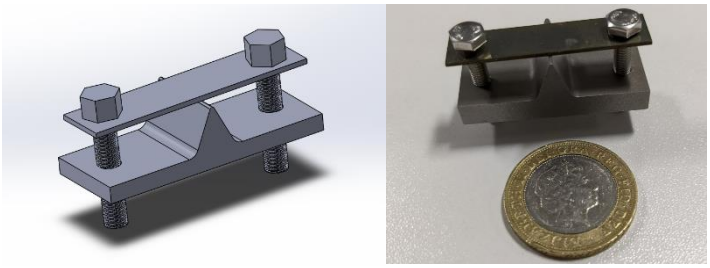

Figure 2.1 Three-point strain rig (left 3D design, right prototype).

$$\sigma = \frac{6Ety}{H^2} \tag{2.1}$$

Where: σ = Maximum tensile stress, E = Young's modulus, t = Specimen thickness, y = Maximum deflection, and H = Distance between outer supports. Subsequently, the dimensions t and y, were taken using a digital calliper Mitutoyo 500-196-30 and E was assumed to be 200 GPa (as reported by Goodfellow Cambridge LTD).

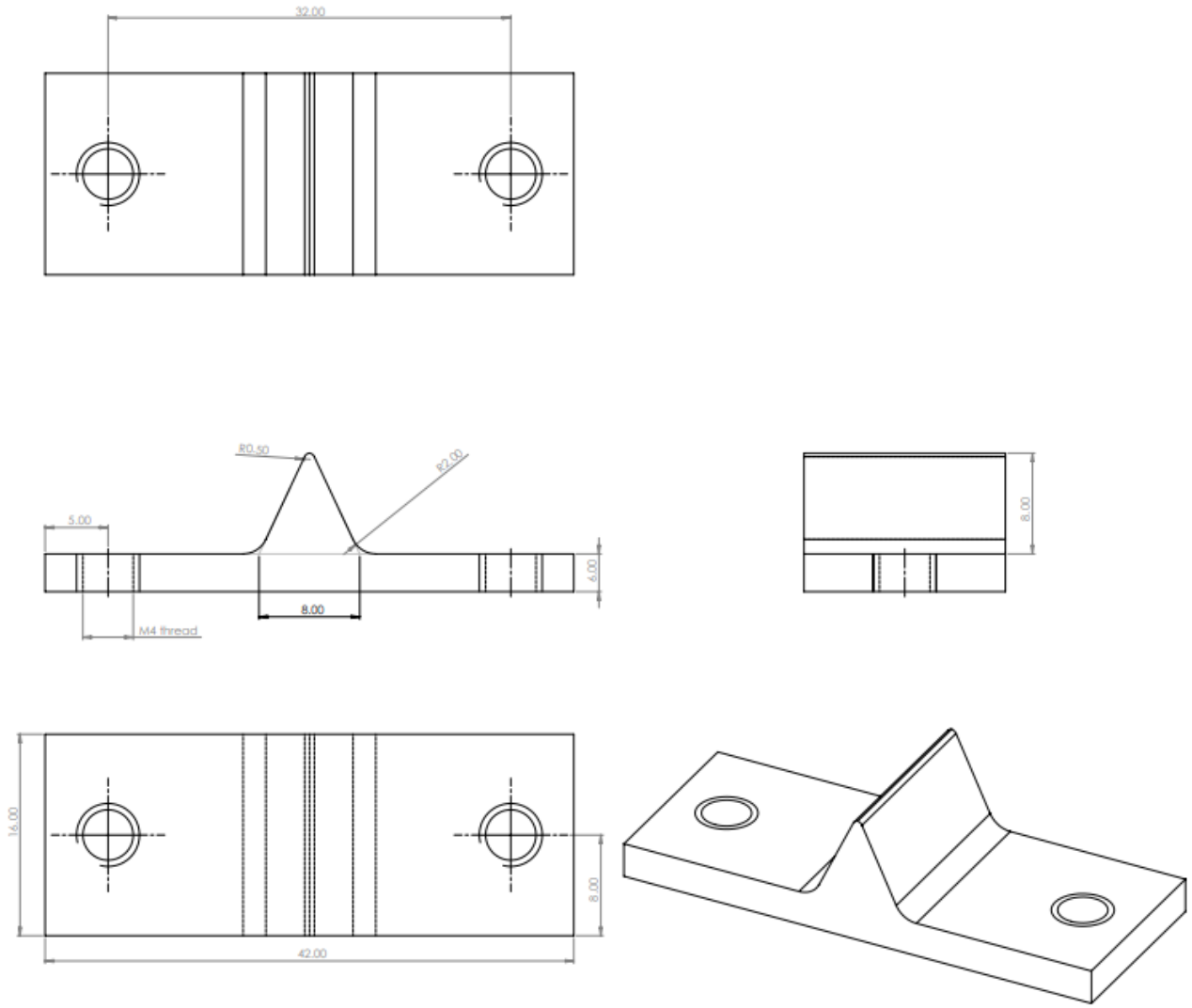

Figure 2.2 Three-point strain rig plot (units in millimetres)

2.2 Droplet test

Droplet tests were carried out using AISI 304 coupons both in the as received and thermally sensitised conditions, with the aim of determining a concentration threshold whereby spontaneous formation of corrosion pits on the surface was possible without the application of external polarisation.

The samples were abraded using a succession of SiC papers of decreasing grit-size (120, 400, 600 and 1200), followed by polishing with diamond suspensions (6 µm, 3 µm, and 1 µm). The polishing process was stopped once the surface of the metal had a mirror finish and there were no scratches visible on the surface.

The droplet tests were done by placing nine (unstrained condition) or six (strained condition) droplets of 5 µl of $MgCl_2$ (1 M, 2 M, 3 M and 4 M) on the surface of polished non-strained and strained (with the 3-point strain rig) samples of AISI 304 (as received and sensitised). Like the relative humidity determines the concentration in the droplet, the specimens were contained in covered petri dishes with 50 ml reservoir solution of the same concentration as the droplet, to ensure equilibrium between the droplet and its environment. The apparatus used for the droplet corrosion experiments can be seen in figure 2.3.

The tests were done at room temperature and for a period of 50 h. The specimens were observed with an optical microscope Zeiss Axio Imager Z2M at 0 h, 24 h and 50 h, aiming to photograph the pitting process at different stages of the experiment. After this step, the samples were removed from the petri dish, rinsed with distilled water and ethanol, and dried with hot air. The areas where the droplets were initially placed were analysed again under a microscope, and pictures of the regions were taken, with a focus on pits or localised corrosion sites. In addition, dimensions such as the diameter of the pits were determined using the measuring capabilities available on the microscope.

Due to the accumulation of corrosion products on the vicinities of the pits, it was necessary to remove them. To achieve this the samples were immersed in 10% w/v oxalic acid at 50°C for 1 hour as per guidance in BS EN ISO 8407 [55].

Subsequently, the samples where the initiation and growth of pits occurred were analysed with a Zeiss Evo LS25 Scanning Electron Microscope (SEM), to obtain images with higher resolution and better detail of the corrosion features.

2.3 Uniaxial tensile test

Despite the mechanical properties being reported by the supplier, uniaxial tensile tests were performed to determine the mechanical properties of both AISI 304 materials (as received and thermally sensitised). The tests were carried out on five sub-sized specimens made of each material, designed following ASTM E8/E8M guidance [56], except for the thickness, which was 0.914 mm instead of 6 mm, due to the limitations of the AISI 304 sheet geometry.

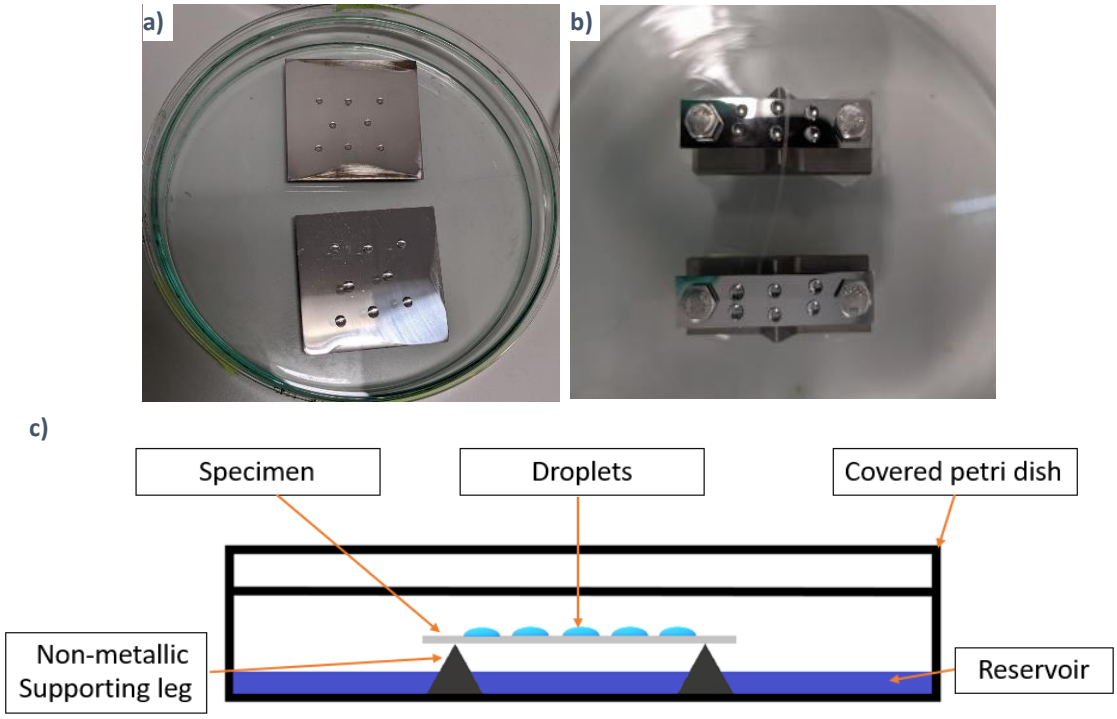

Figure 2.3. Example of droplet test on SS 304 samples. a). Non- strained conditions, b) Strained conditions, c) Cross-sectional set-up for non-strained samples.

The tests were performed using a HTE Hounsfield universal tensile test machine at room temperature with a speed of 3 mm/min. The dimensions of the samples were taken with a digital calliper Mitutoyo 500-196-30 and, the yield point was determined with the 0.2% offset strain method. Also, there was not extensometer used in the experiment, and therefore the distance between grips was taken as the initial length for the strain calculations. A photograph taken during one of the tests is shown in figure 2.4.

2.3.1 Uniaxial tensile test on samples with pits nucleated on surface

In the same way, additional tensile tests were performed on three samples of each material with corrosion pits on the surface, which were nucleated by following the same droplet test procedure described in section 2.2 with the difference that only a single droplet of 4 M $MgCl_2$ with a 6 µL volume was placed at the centre of the sample, and the surface preparation was less rigorous. The aim of this test was to determine if a small cavity was able to alter the mechanical properties of the

material. In addition, photographs were taken before and after the test using a Zeiss Axio Imager Z2M microscope.

Figure 2.4 Example of a AISI 304 specimen under tensile test.

2.4 Scanning Vibrating Electrode Technique (SVET)

SVET was first applied in corrosion research in the early 1980s and subsequently has been employed in the investigation of different types of corrosion phenomena such as galvanic corrosion, pitting corrosion, corrosion performance of coatings, etc. [57].

The SVET equipment used in this research project was developed and built 'in-house' at Swansea University, a schematic diagram highlighting the main features is shown in figure 2.5 [58]. This device uses a vibrating Platinum electrode made of a short segment of 125 µm diameter wire sealed in glass, commonly referred as a 'probe', which oscillates at a fixed amplitude and frequency in the *z* direction. In addition, this apparatus employs a second reference electrode of larger area (2.5 cm^2) and lower impedance, made of Ag/AgCl foil which is located at 5 cm distance from the probe acting as the instrument earth.

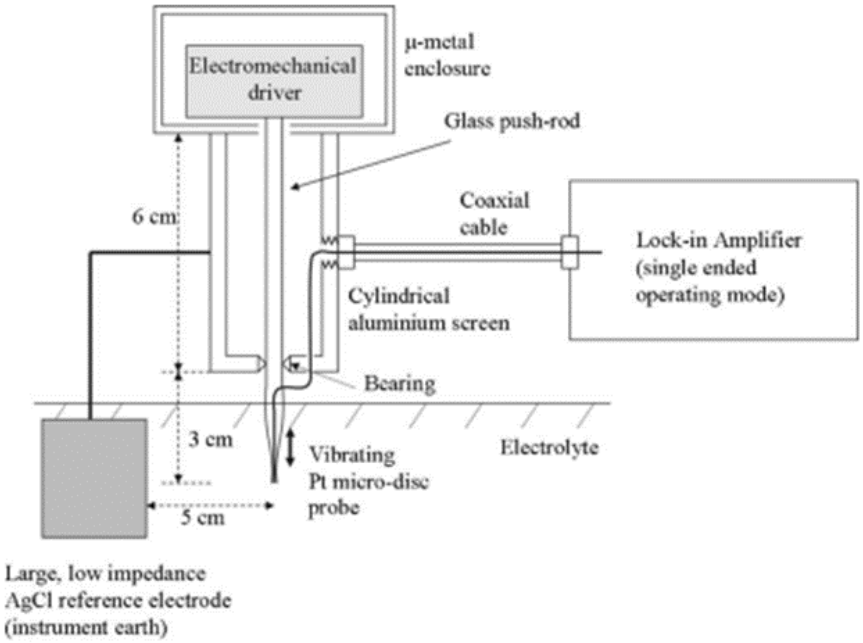

Figure 2.5. Schematic representations of the SVET probe assembly [58].

The device is designed such that the vibrating probe can be moved in 100 μm steps (length) in the *x* and *y* planes over distances of up to several cm. When the probe oscillates it can intersect equipotential lines in the *z* plane, measuring the change of potential gradient. Such changes in potential derive from an external source, such as the electrochemical reaction on the surface of a metal actively corroding in the same solution, making possible to study localised corrosion behaviour in-situ, as shown in figure 2.6.

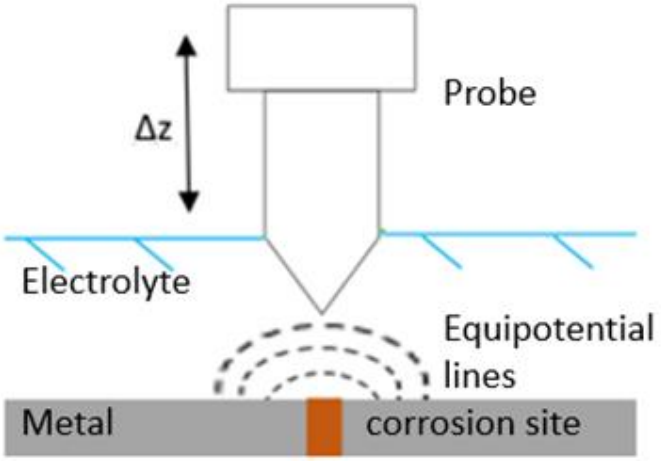

Figure 2.6. Example of the SVET use in the study of corrosion.

2.4.1 SVET Calibration

Before starting every experiment, the probe was immersed in 2 M HCl solution for a period of 5 minutes, followed by rinsing with distilled water, ensuring the removal of any contaminants present on the surface. Subsequently, the calibration of the equipment started with setting up the lock-in amplifier frequency to 140 Hz, the amplitude to 0.015 V, and the sensitivity to 100 µV, using a similar approach to the one described by McMurray et al. in their research [59].

The second part of the calibration procedure consisted in ensuring that the lock-in amplifier was in the appropriate phase for the readings. To establish this a bespoke two-compartment tube cell, the working solution, and an external source of current (galvanostat) were used. The two-compartment cell has two separate Platinum electrodes embedded, one facing the inside and another the outside of the vessel.

The bespoke two-compartment tube cell was then placed in a bigger tank and the working solution was poured inside such that it covered the smaller tube but did not overflow the bigger one. Then the probe was placed inside the smaller tube, immersing it to 10 mm depth, the AgCl reference electrode was also put in contact with the bulk solution and the Pt electrodes were connected to the positive and negative poles of the galvanostat. The setup is shown schematically in figures 2.7 and 2.8.

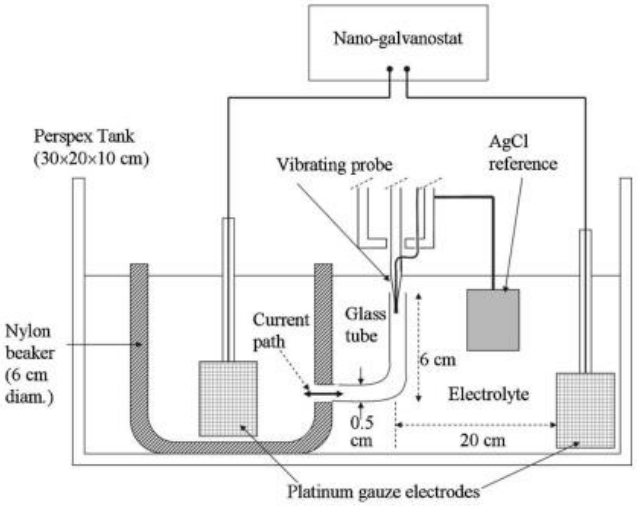

Figure 2.7. SVET setup calibration with a two-compartment tube cell [58].

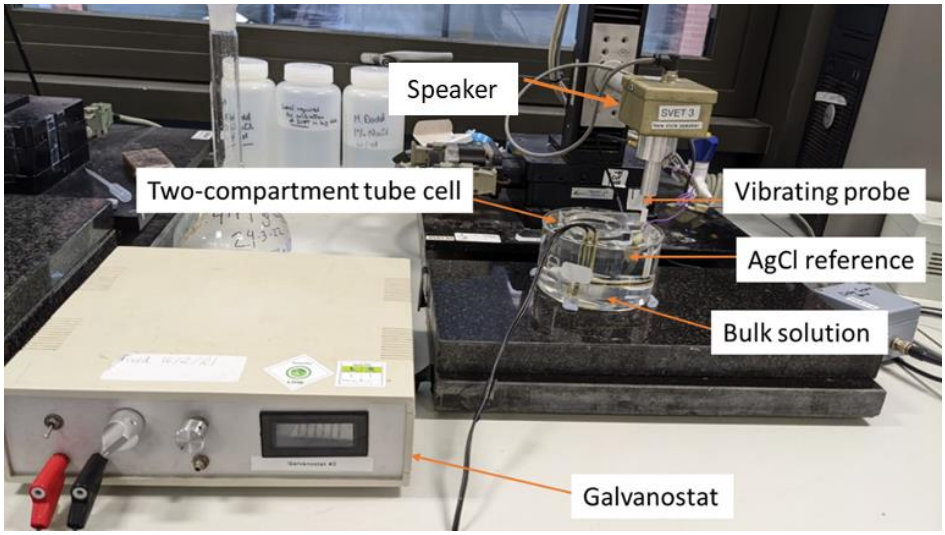

Figure 2.8 SVET calibration setup.

Once the galvanostat applies some current to the system, the only route for the flux of ionic current is through the small tube area, where the SVET probe is vibrating, making it possible to correlate the applied current with the voltage readings on the lock-in amplifier. Furthermore, taking into consideration that the small tube radius is known and considering that the current is constant across the tube area, it is possible to correlate the nanovolt readings to current density [58].

Consequently, a current sweep was applied to the system; first from 50 µA to 0 µA, while the nanovolt readings were recorded. Once the zero point was reached, the electrode connections on the galvanostat were swapped, meaning the positive electrode would be the negative and vice versa. The current sweep then was carried out from 0 µA to - 50 µA, again recording the nanovolt readings.

The current values were then divided by the small tube area, resulting in current density. Then such values were plotted against the potential gradient obtained, resulting in a linear relationship. By using the gradient obtained from this calibration, nanovolt readings from SVET are able to be correlated to values of current density (figure 2.9).

It is important to highlight that an appropriate calibration ensures an accurate signal reading during the SVET experiments. The lock-in amplifier uses sinusoidal signals, a wrong phase of 180 ° with the SVET speaker setup can result in values

with the inverse signs (positive or negative), meaning that anodes and cathodes would be inverted. This calibration procedure was performed each time the equipment was used, independently if the solution had the same concentration of a previous tests.

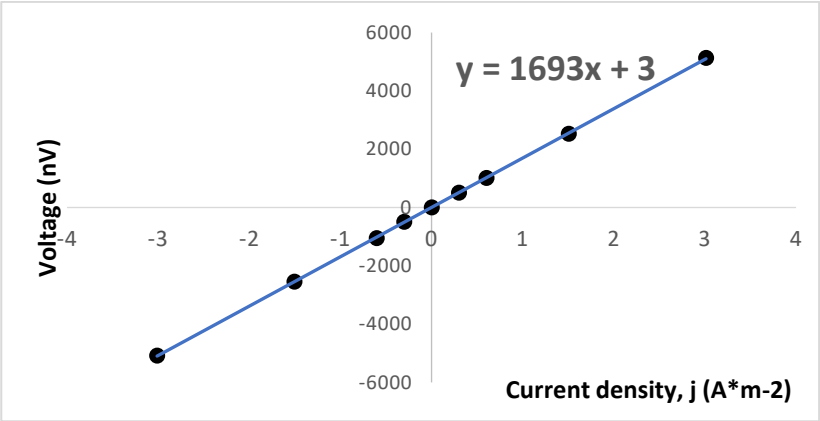

Figure 2.9. Example of a typical SVET calibration plot for a 4 M $MgCl_2$ solution.

2.4.2 SVET height scan profile

The distance between the vibrating probe and the metal surface to be studied has been demonstrated to have a significant influence on SVET readings [59]. For this reason, during the duration of the experiment it was imperative that all the measuring points of the surface were completed at an appropriate distance and scanned at the same height, so they could be correlated. The SVET used in these experiments has a secondary mode for height scan that allows to the apparatus to identify when the vibrating probe touches a surface by measuring the change in inductance between the SVET probe speaker and a reference speaker within a bridge type circuit. Once the surface has been detected, the instrument software maintains the same distance between sample and probe for the duration of the scan. Such software had two height profiling options, described below:

- Planar interpolation: First it was necessary to define the scanning area dimensions, giving the co-ordinates of the four corners in the *x* and *y* plane of the metal surface to be examined. Once this was completed the SVET took height readings at these 4 points and the software interpolated the *z* distance between them, creating a plane and adjusting the height linearly to

measure points in between. This setup was used successfully for flat specimens, such as the non-strained AISI 304 samples, because the surface must be free from irregularities, otherwise the probe could have contacted the surface or any imperfection on it, leading to instrumental artefacts.

- 3D height scanning: This mode also required four coordinates to be defined in the *x* and *y* plane. The SVET would take into account the difference and take readings at determined points between them. This allowed topography of the sample surface to be followed independently of its shape, being the ideal setup to scan the convex samples under strain in the three-point strain rig. For the experiments performed, the SVET was programmed to take readings in 100 µm steps, and an example of the surface profiled by the software using this technique can be seen in figure 2.10. Detailed information on the 3D height scan mode can be found in the work of Wilson [60].

Once the surface to be scanned was defined by the linear interpolation method or the 3D height scanning, the SVET was then programmed to scan the same area by positioning the vibrating probe at a distance of 150 µm in the *z* plane above the surface, thus permitting a reasonable spatial resolution whilst avoiding physical contact with the metal surface.

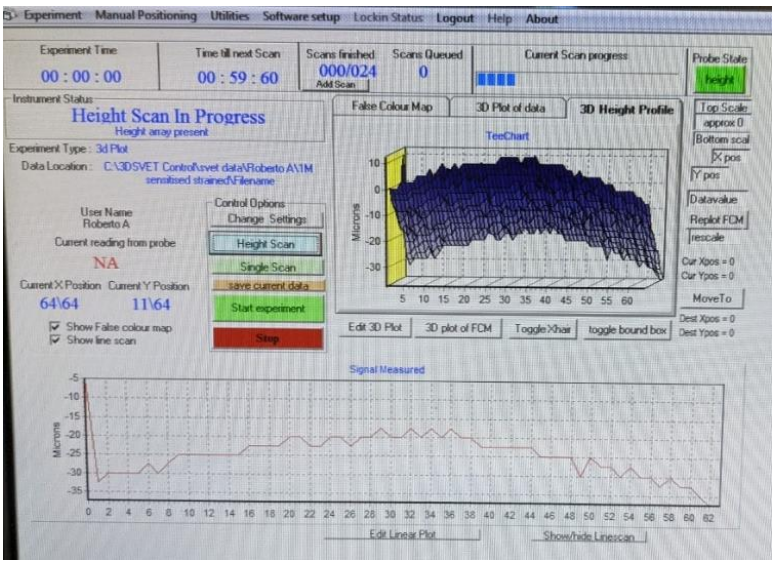

Figure 2.10 SVET 3D height scan modelling.

2.4.3 SVET experiments

Once the calibration and height profiling steps were completed, the SVET experiments were started. The tests were performed on AISI 304 stainless steel in the as received and sensitised condition, immersed in a solution of 4 M $MgCl_2$ which proved to be able to induce pitting corrosion under open circuit (unpolarised) conditions. To determine the effect of external load the specimens were tested in both strained and non-strained conditions.

Test specimens were ground down with SiC paper (120, 400, 600 and 1200), followed by polishing with diamond suspension 6 µm, 3 µm, and 1 µm. To isolate the scanning region, the surface was covered with polytetrafluoroethylene (PTFE) 5490 tape provided by 3M LTD, leaving an uncovered area of approximately 35 mm^2.

The experiments were carried out for a period of 24 hours, with a frequency of 1 scan per hour at room temperature. It is important to highlight that the metallic bolts used in the three-point strain rig (as seen in figure 2.1) were swapped for nylon bolts (as seen in figure 2.11). This change avoided electrical contact between specimen and the rig and a possible interference with the corrosion phenomenon in the exposed area, while they were immersed in the same electrolyte.

Once the experiment was completed, the sample was removed and rinsed with DI water and ethanol, dried with hot air and examined under an optical microscope to analyse any pit or corrosion site that may have developed on surface. If the sample had any pits, it was then immersed in oxalic acid to remove corrosion products on the vicinities. In addition, examination at higher magnification was completed using SEM and Keyence VHX-1000 digital microscope, which permitted a depth profile of the pit to be obtained.

As mentioned in section 2.4.1, the data obtained during the scans needed to be transformed, such that the potential values are divided by the slope obtained during the calibration experiment, converting the nV values to $A \cdot cm^{-2}$. Once finished, the results were processed using Surfer™ mapping software, producing a 3D map of the current density values in the *x* and *y* plane.

When localised corrosion had occurred during the experiments, such maps showed pit-like features as anodic peaks, making it possible to study changes in pitting current density values throughout the experiment duration.

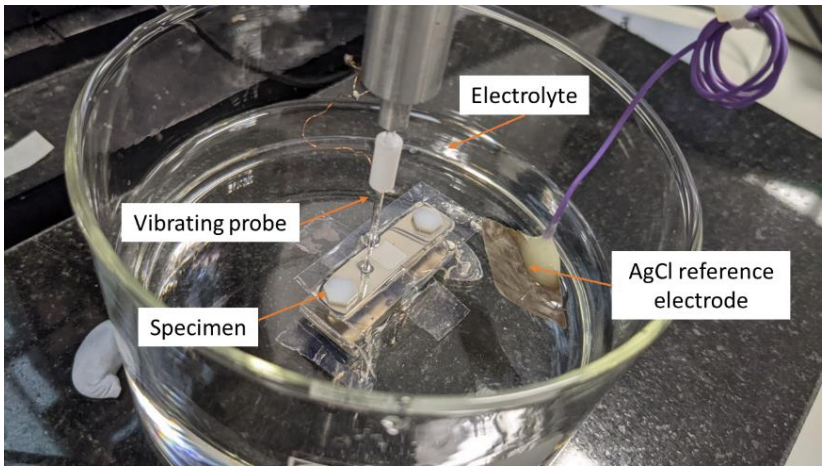

Figure 2.11 SVET experimental setup for a strained sample using the three-point strain rig.

2.5 DC Electrochemistry

A series of electrochemical experiments were performed on AISI 304 material in the as received and thermally sensitised form to determine the effect of stress on pitting corrosion susceptibility. Tests were completed on samples in non-strained and strained conditions using the same three-point strain rig shown in figure 2.1.

A Gamry Interface 1010E potentiostat was used to perform the Open Circuit Potential (OCP) and potentiodynamic polarization measurements on the samples. A solution made of 1 M $MgCl_2$ was selected as the electrolyte, the specimens were ground down using SiC paper (120, 400, 600 and 1200), rinsed with distilled water followed by ethanol, and dried with hot air. To isolate the area of contact between the material and the electrolyte, the coupons were covered with PTFE 5490 tape, such that only an area of approximately 36 mm^2 in the centre of one face was exposed to the electrolyte. To ensure electrical isolation between the samples and the three-point strain rig, additional layers of PTFE tape were added on the surface of the rig, specifically at the mid-point.

2.5.1 OCP measurement

The OCP experiments were completed at room temperature, for a period of 60 minutes prior to starting a potentiodynamic polarization experiment. For the measurements, a two-electrode cell was used, consisting of the sample coupon (acting as working electrode) and a saturated calomel electrode (SCE) as reference electrode. The potential difference between both electrodes was measured by the potentiostat as a function of time and the value was equal to the corrosion potential (E_{corr}) of the metal.

2.5.2 Potentiodynamic polarisation curves

The potentiodynamic polarization tests were carried out using the same electrolyte and temperature as previously, with the difference that a three-cell electrode was employed. The electrodes were configured as follows: the stainless-steel coupon as the working electrode, SCE the reference and a Platinum (Pt) gauze was used as counter electrode.

Once the OCP measurements were finished, usually obtaining a relatively stable value of E_{corr}, the potentiostat was programmed to polarise the sample applying a difference of potential of -300 mV more negative than E_{corr}, this was then increased at constant increments of 0.1667 mV/s. The potential sweep was carried out up to a value of +700 mV more positive than E_{corr}.

While the polarisation sweep was carried out, the variation of current was also recorded by the potentiostat, making possible to plot *E* vs Log *i*, obtaining the characteristic polarization curves for the materials studied, as exemplified in figure 1.3.

2.6 Coupons of 20Cr/25Ni/Nb – 45 Fe/45Ni/10Cr

Coupons of 20Cr/25Ni/Nb electron beam welded to a simulant sensitised grain boundary alloy 45Fe/45Ni/10Cr in a 3:1 area proportion were provided by the National Nuclear Laboratory (NNL).

The 20Cr/25Ni/Nb stainless steel is the same alloy used in the cladding material to encapsulate the UO_2 fuel pellets used in the fission process inside the AGR, and prior to welding was annealed at 930 °C in a 4% H_2 in Argon mix for 1 hr. Such a

heat treatment was aimed at stress relief within the material after the sheet rolling process. In the same way, the simulant grain boundary material was cut into 1 mm thick pieces by bandsaw, and hot rolled (900 °C). These pieces were then annealed at 1000 °C. This simulant grain boundary composition aimed to mimic the effect of the RIS at grain boundaries, obtaining a lower quantity of Cr and Fe while increasing the Si and Ni content.

Such coupons were previously tested and irradiated for 1219 hr (Co-60 gamma irradiation) with the flask at up to 50° C, in air + 700 vpm H_2O conditions, and were provided for electrochemical characterisation using DC electrochemical techniques, SVET and Scanning Kelvin Probe (SKP).

2.6.1 DC Electrochemistry - Coupons of 20Cr/25Ni/Nb – 45Fe/45Ni/10Cr

A Gamry Reference 600+ potentiostat was used to perform OCP and potentiodynamic polarization curves on the coupons. The electrolyte was a solution of 1 M NaCl and the reference electrode was a SCE. The specimens were ground down using SiC paper (120, 400, 600 and 1200), rinsed with distilled water followed by ethanol, and dried with hot air. In separate experiments three different areas of the welded specimen were isolated, such that the corrosion behaviour these different regions of the coupon could be investigated separately, as detailed below and shown in figure 2.12:

a) 20Cr/25Ni/Nb or cladding alloy with a surface area of 100 mm^2.

b) 20Cr/25Ni/Nb-Weld-45Fe/45Ni/10Cr or Cladding-weld-simulant with a surface area of 100 mm^2.

c) 45Fe/45Ni/10Cr or simulant grain boundary with a surface area of 100 mm^2.

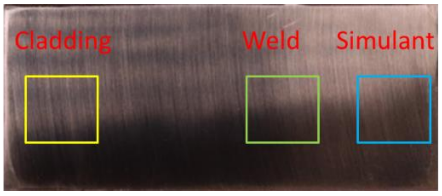

Figure 2.12. Location of the three different test regions for coupons of 20Cr/25Ni/Nb – 45Fe/45Ni/10Cr. Yellow square cladding material, Green square Cladding welded to the simulant, and Blue square simulant material.

To isolate the area of contact in the coupon, the samples were covered with PTFE 5490 tape, such that only the area of interest was exposed and immerse in the electrolyte.

Similarly, to the procedure described in 2.5.1 and 2.5.2, E_{corr} was measured by OCP for 30 minutes prior to the potentiodynamic test. Then, the potentiostat was programmed to polarise the sample applying a difference of potential of -300 mV more negative than the E_{corr} which was then increased by constant increments of 0.1667 mV/s. The sweep was carried out up to a value of +700 mV more positive than $E_{corr.}$

2.6.2 SVET - Coupons of 20Cr/25Ni/Nb – 45 Fe/45Ni/10Cr

For SVET experiments carried out on a welded coupon sample, the electrolyte used was 1 M NaCl at room temperature. Test specimens were abraded using SiC paper (120, 400, 600 and 1200), rinsed with distilled water followed by ethanol, and dried with hot air. Then PTFE tape was placed on the surface to isolate an area of 100 mm^2 that covered a region constituted of 20Cr/25Ni/Nb – Weld - 45 Fe/45Ni/10Cr, such that both alloy types had the same area exposed.

The calibration and height profile followed the same steps described in 2.4.1 and 2.4.2 for flat specimens, and the experiment was carried out for 24 h. At the conclusion, the specimen was removed and rinsed with DI water and ethanol, dried with hot air and examined under a microscope. Once finished, current density maps were obtained.

As the coupons were likely to act as a galvanic couple, the corrosion potential under OCP conditions was measured in a different experiment for a sample with the same characteristics. The aim was to correlate the results with the data obtained by the SVET. To accomplish this, it was necessary to weld a small section of wire to one of the coupon's sides, enabling its connection to a potentiostat.

2.6.3 Scanning Kelvin Probe (SKP)

The Scanning Kelvin Probe is a non-contact and highly sensitive electrochemical scanning probe technique, which can measure the difference of surface potential of

conducting specimens that are connected to the probe, without the need for bulk electrolyte.

The SKP probe vibrates perpendicular to the surface of a metal at a determined distance, and along with the dielectric medium between both materials (air), forms the components of a parallel plate capacitor. It is known that when two different metals are in electrical contact, a flow of charge between the two materials to equilibrate their Fermi levels occurs. The result of this process is the formation of a potential difference (known as volta potential $\Delta\psi$) between the outer surfaces of the two materials [61,62].

The capacitance for a parallel capacitor follows the relation:

$$C = \frac{\varepsilon_0 \varepsilon A}{d} \tag{2.1}$$

Where, C is the capacitance, ε_0 is the permittivity in the vacuum, ε is the dielectric constant of the capacitor, A is the area of the capacitor, d is the distance between capacitor plates.

Taking in consideration that ε_0, ε and A are constant values, the capacitance is inversely proportional to the distance between plates. In the case of the SKP, the probe is attached to an electromechanical vibrator (or loudspeaker) which makes it vibrate perpendicular to the surface of the specimen at a determined frequency and amplitude. If the probe vibrates, the distance between the capacitors is subjected to a sinusoidal change, and this in turn produces a periodic change in capacitance thus generating an AC current signal in the circuit connecting the two capacitor plates [61,62]. The AC current signal is subsequently converted into an AC voltage signal using dc-biased transimpedance amplifier. A lock-in amplifier is used to supply the alternating voltage (at 280 Hz) which provides the drive signal for probe vibration and detects the AC voltage output, allowing the volta potential to be measured in conjunction with an analogue integrator circuit [61,62]. This supplies an external DC voltage with the same magnitude that needs to be applied to the system, such that the net current of the system is zero. This reverse bias

potential (U_{null}) nulls the current flowing in the circuit connecting both probe and specimen so the Fermi levels return to their original positions [61], such that:

$$-U_{null} = \Delta\psi \qquad (2.2)$$

2.6.3.1 SKP setup and calibration

The SKP used in these experiments is an apparatus designed and built at Swansea University. The probe and the samples are maintained inside a stainless-steel chamber, which is used to keep the humidity controlled (in conjunction with a suitable saturated salt solution reservoir), also working as a barrier for electrostatic, electromagnetic, and external noise. The Kelvin probe is made of a 125 µm gold wire attached to the loudspeaker by a glass capillarity push rod and is vibrated at an amplitude of ± 10 µm. To convert the current to voltage, the sample to be tested is connected to a convertor. The sample is located on a stage attached to a stepper motor that can be moved in the three planes, making it possible to control the distance between both probe and specimen surface and measure $\Delta\psi$ over the required area of the surface. An illustration of the equipment is shown in figure 2.13.

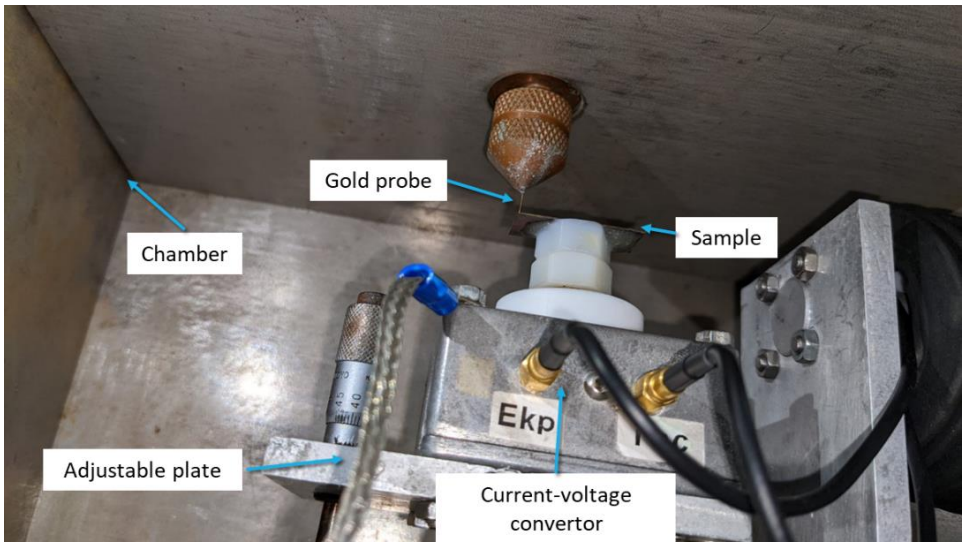

Figure 2.13 SKP experiment setup.

As mentioned by Williams and McMurray, the relationship between E_{corr} and $\Delta\psi$ for a bare metal interface follows the following relation [63]:

$$E_{corr} = \Delta\psi_{sol}^{ref} + A \quad (2.3)$$

For this reason, it is imperative to obtain values of constant *A*. Therefore, prior to use the SKP is calibrated in terms of electrode potential, which can be done using the Cu/Cu^{2+} (0.5 M) redox couple. It is known that the E_{corr} value for the Copper calibration cell is +0.32 V vs SHE. If a value for $\Delta\psi_{sol}^{ref}$ for the Cu/Cu^{2+} redox couple is established by positioning the vibrating gold probe over the surface of the meniscus of the of the Cu^{2+} (0.5 M) electrolyte in contact with Cu, then equation 2.3 can be used to determine the value of constant *A*. Such a value then can be added to every raw data point collected afterwards in the experiment to produce E_{corr} distributions.

2.6.3.2 SKP for coupons 20Cr/25Ni/Nb – 45 Fe/45Ni/10Cr

The aim to test the coupons using SKP was to gather additional information about the nobility of the different areas of the coupon under humid conditions. Prior the start of the test the probe was immersed in a solution of 2 M HCl for a couple of minutes, followed by rinsing with DI water which ensured the removal of any corrosion product/contamination. The sample surface was ground down using SiC paper (120, 400, 600 and 1200), followed by polishing with diamond suspension (6 µm, 3 µm and 1 µm), then it was rinsed with distilled water and ethanol, and dried with hot air.

After mounting the specimen on the SKP stage, the gold vibrating probe was positioned at 100 µm above the surface, and the software was configured to record measurements in 50 µm steps in the y direction for a length of 12 mm, repeating the sequence on seven lines spaced by 1 mm. To maintain a fixed relative humidity (RH) in the chamber of around 95%, a reservoir containing an aqueous solution of 5% NaCl was placed inside the chamber. It is important to mention that prior the start of the test, the chamber was sealed, and the SKP was programmed to take measurements once an hour for 24h.

2.7 List of experiments performed

A list of the samples and conditions tested can be found in table 2.2.

Table 2.2 Samples tested, techniques and conditions.

Material	Droplet test	SVET	Potentiodynamic polarisation curves	SKP
AISI 304 As received non-strained	1 M, 2 M, 3 M and 4 M $MgCl_2$	3 M and 4 M $MgCl_2$	1 M NaCl	-
AISI 304 As received strained	1 M, 2 M, 3 M and 4 M $MgCl_2$	3 M and 4 M $MgCl_2$	1 M NaCl	-
AISI 304 Sensitised non-strained	1 M, 2 M, 3 M and 4 M $MgCl_2$	3 M and 4 M $MgCl_2$	1 M NaCl	-
AISI 304 Sensitised strained	1 M, 2 M, 3 M and 4 M $MgCl_2$	3 M and 4 M $MgCl_2$	1 M NaCl	-
20Cr/25Ni/Nb – 45Fe/45Ni/10Cr	-	1 M NaCl	1 M NaCl	5% NaCl

Chapter 3

3. In-situ mapping of localised corrosion under the effect of strain using a scanning vibrating electrode technique

3.1 Introduction

The pitting corrosion process of austenitic stainless-steel grade 304 was investigated under strained and non-strained conditions in $MgCl_2$ aqueous solutions of different concentrations. To compare the effect of sensitisation, experiments were conducted on annealed (or as received) and thermally sensitised samples. The material and conditions were selected to produce material that could be used as a proxy for specific nuclear applications.

The experiments included:

- Droplet tests - using different chloride concentrations to identify whether applied strain produced pitting at a lower concentration than observed in the absence of strain.
- Polarisation - to identify differences in pitting potentials in the presence/absence of strain.
- SVET - to investigate any differences in pit initiation and propagation under full immersion conditions observed in the presence/absence of strain.
- Post-test examination with a light microscope, SEM (scanning electron microscope) and height-depth digital microscope to study the pit morphology and distribution.

Before reporting and discussing the experiments focused on corrosion behaviour, it is important to present the results of the tensile test (shown in table 3.1) and microstructural analysis (shown in figure 3.1).

As shown in table 3.1, the sensitisation heat treatment had a slight detrimental effect on the mechanical properties of SS 304. This negative effect resulted in a less resilient material with a lower yield point and decreased plasticity.

Table 3.1 Tensile test result for AISI 304 (as received and sensitised).

Material	Yield point (MPa)	UTS (MPa)	Max elongation
AISI 304 (as received)	296 ± 61	680 ± 39	0.73 ± 0.06
AISI 304 thermally sensitised	276 ± 46	674 ± 13	0.65 ± 0.05

As mentioned in section 2.1.3, the stress in the outer layer applied with the three-point strain rig can be calculated using equation 2.1. In the experiments conducted in this research project, the maximum deflection value (y) was fixed to be equal to 0.35 mm for all the strained experiments.

Solving equation 2.1 with t = 0.914 mm, H = 32 mm, E = 200 GPa, and y = 0.35 mm, the stress in the outer layer would be equal to 375 MPa. However, this value is above the yield point seen in table 3.1, and the equation 2.1 is not applicable. Therefore, it is considered that the material was under plastic deformation in the strained experiments, and it is not possible to accurately estimate the stress applied.

Figure 3.1 presents the microstructure of the tested samples as revealed by electro-etching with oxalic acid. The as-received sample (Figure 3.1a) exhibits a uniform grain structure with no apparent carbide precipitates at grain boundaries. Interestingly, the thermally sensitised specimen (Figure 3.1b) lacks a severe sensitised microstructure expected, despite some grains displaying darker features at the grain boundaries. Two potential explanations for this observation are:

- Material Composition: The supplied material might be AISI 304L instead of 304. AISI 304L has a lower carbon content, leading to improved resistance to sensitisation. Unfortunately, the lack of chemical analysis prevents confirmation, and the material's condition was assumed to be as ordered.
- Heat Treatment: The applied heat treatment conditions (temperature, time, etc) may not have been optimal to induce a fully sensitised microstructure.

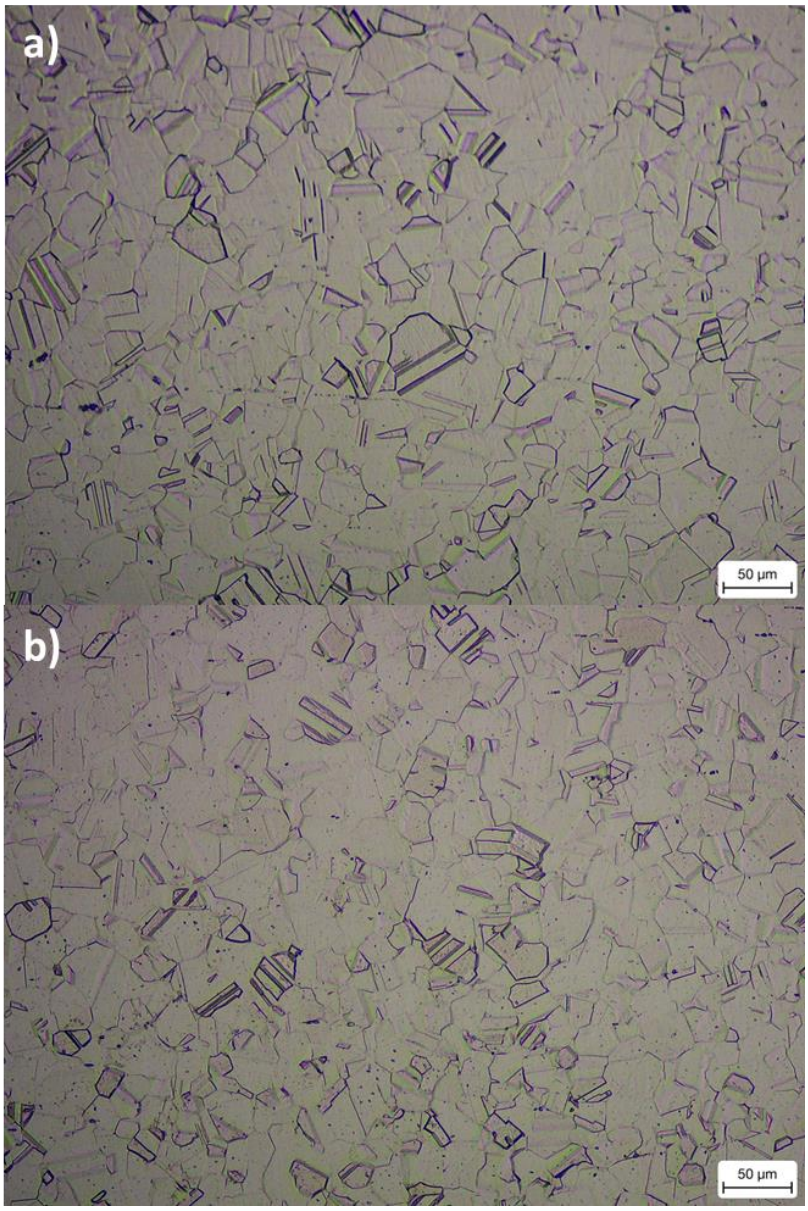

Figure 3.1. AISI 304 microstructure, a) As received, and b) thermally sensitised. Both images at 20X magnification obtained with an optical microscope.

Although the degree of sensitisation appears less severe than initially anticipated, the heat-treated samples are designated as "sensitised" for clarity in identification.

3.2 Droplet test

The deposition of droplets of aqueous salt solutions has been used by several researchers to study atmospheric pitting corrosion in stainless steels [64-68]. The corrosion mechanism in this case is different from the classic bulk electrolyte corrosion because of the thin and non-uniform geometric thickness of the droplet.

The corrosion is driven by the depletion of oxygen at the centre (anode) of the droplet compared to the edge (cathode). This phenomenon is known as the differential aeration cell.

The results of the droplet test for non-strained samples are shown in tables 3.2 and 3.3 (section 3.1.1). The results for strained specimens are shown in tables 3.4 and 3.5 (section 3.1.2).

3.2.1 Droplet test in non-strained conditions

Analysing table 3.2, it is noticeable that the pitting process is strongly dependent on the $MgCl_2$ concentration. No signs of pitting were observed for samples tested in 1 M and 2 M $MgCl_2$ solutions. However, 4 pits were found in 9 droplets for each material tested in 3 M $MgCl_2$, and at least 1 pit per droplet was found in tests performed in 4 M $MgCl_2$.

These results are consistent with previous studies that have shown the direct influence of chloride concentration on the pitting probability in droplet tests [64, 66]. It is expected that electrolytes with a concentration higher than a critical value will develop pitting corrosion.

Matsumi et al. [69] and Tsutsumi and colleagues. [70] reported that the critical chloride concentration for pitting in SS 304 was 6 M at room temperature (65% RH) when performing droplet tests. This value is in accordance with the results shown in table 3.2.

Also, Street et al. [71] performed electrochemical experiments on AISI 304 and showed that the passive current density increased significantly above 3 M $MgCl_2$, while the breakdown pitting corrosion potential (E_{pit}) dropped as the concentration increased above this value. This can explain the higher incidence of pitting when samples were tested in 4 M $MgCl_2$ in AISI 304.

It is important to note that the relative humidity (RH) was not a monitored parameter in the present study. Using a solution reservoir with the same concentration of the droplet applied on the surface of the SS samples (see figure 2.3), promoted an equilibrium in the relative humidity within the chamber, which

ensured that the $MgCl_2$ concentration did not change due to droplets gaining or losing water with time. This is one of the main differences between the experimental procedure reported in this investigation and the one followed by other researchers [64-71].

In the same way, table 3.3 shows that the pit diameter increased proportionally with the chloride concentration in the electrolyte. The heat treatment applied also influenced the pit diameter and depth, particularly for experiments carried out at 3 M $MgCl_2$ (see figure 3.2).

Table 3.2 Droplet test results for non-strained AISI 304 samples.

Droplet test @50 h 298 k	AIS 304 (As Received)	AISI 304 Thermally sensitised
1 M $MgCl_2$	0 pits in 9 droplets	0 pits in 9 droplets
2 M $MgCl_2$	0 pits in 9 droplets	0 pits in 9 droplets
3 M $MgCl_2$	4 pits in 9 droplets	4 pits in 9 droplets
4 M $MgCl_2$	9 pits in 9 droplets	10 pits in 9 droplets

Table 3.3 Average pit diameter comparison for non-strained AISI 304 samples.

Material	AISI 304 (As received)	AISI 304 thermally sensitised
3 M $MgCl_2$	4 pits 29 µm ± 9 µm	1 - pit 83 µm 3 pits - 24 µm ± 11 µm
4 M $MgCl_2$	133 µm ± 30 µm	138.0 µm ± 23 µm

The pit morphologies shown in figure 3.2 (a-b), suggest that the pits nucleated in as received samples with 3 M $MgCl_2$ solution, repassivated shortly after they initiated. This is because the rate at which metal ions escaped from the pit mouth was greater than the rate at which they were produced by anodic dissolution.

Galvele [72] explained that pit repassivation takes place when the rate of metal ion diffusion out of the pit is greater than the rate of metal ion production by anodic

dissolution when the pit stability is controlled by diffusion. In addition, it is known that pits are only stable when the maximum cathodic current is greater than the minimum anodic current required to support their growth [68]. Therefore, it seems that the conditions were not met to sustain stable pitting for the as-received material in 3 M $MgCl_2$ solution.

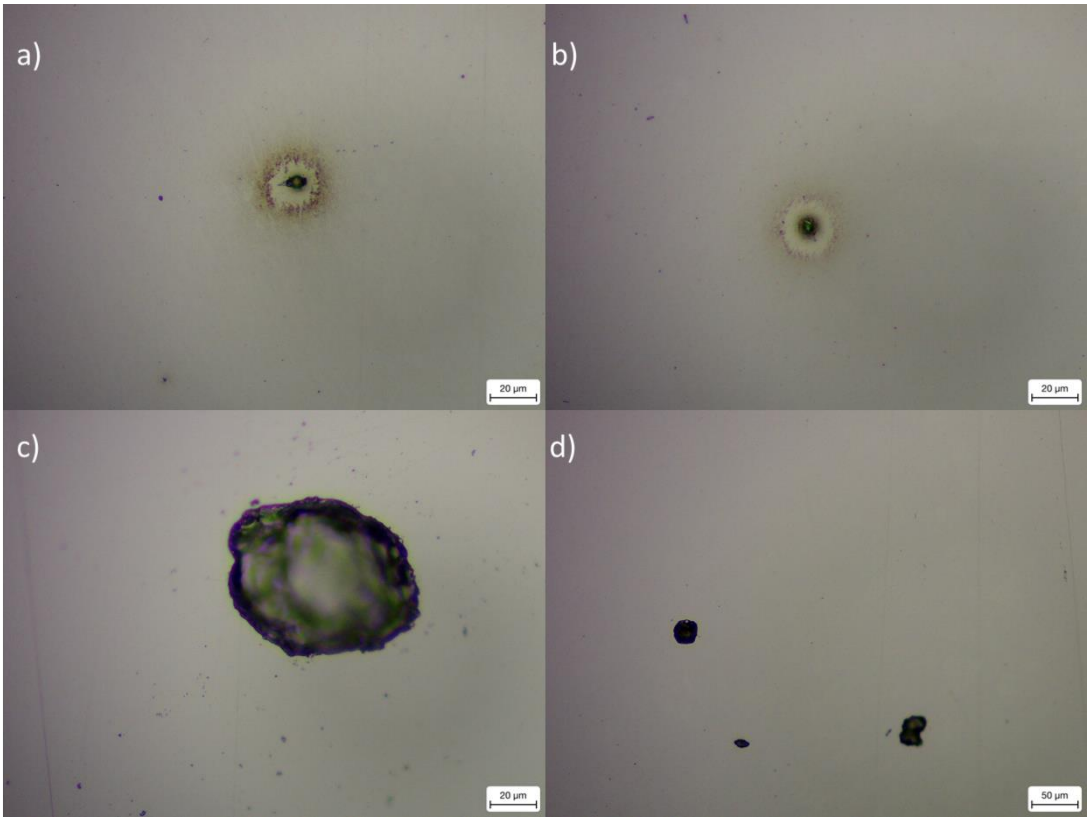

Figure 3.2 Pit morphology of SS 304 samples tested with 3 M $MgCl_2$ droplets in non-strained conditions, obtained with an optical microscope: a-b) SS 304 as received (50X), c) SS 304 sensitised (50X), d) SS 304 sensitised (20X).

Figure 3.2 (c-d) shows that the localised corrosion process was more active for the heat-treated specimens tested in 3 M $MgCl_2$. Being evident a higher dissolution of metal in the pit and even the nucleation of a colony of cavities (Figure 3.2-d). This behaviour exemplifies the negative effect produced by the heat treatment applied, possible formation of $Cr_{23}C_6$ precipitates at grain boundaries and depletion of Cr in the adjacent area [73,74].

The Cr depletion influences the breakdown pitting potential (E_{pit}), which decreases as a function of sensitisation [75], even for SS 304, which has a vast amount of Cr

(between 17 – 19.5% wt.) and a chromium oxide layer at the metal-electrolyte interface in mediums containing chlorides [76].

The pit morphologies obtained in samples tested in 4 M $MgCl_2$ were substantially different to the ones observed in 3 M $MgCl_2$. They are shown in detail in figure 3.3.

Analysing the different images in figure 3.3, it is noticeable that they had some similarities regardless of the heat treatment condition. The morphology observed can be summarised below:

- Figures 3.3-a and -d, have a shallow dish region with crystallographic etching (highlighted with the red dashes) and a deeper attacked side (yellow dash line) that can propagate inside the dish (-a) or outside (-b), such morphology was also observed by other researchers [66, 71].
- Figure 3.3-b had a large pit mouth (around 70 µm diameter) which might have consumed an initial shallow dish. This morphology was also observed by Street et al [71].
- Figure 3.3-c shows both a shallow dish region that developed crystallographic etching, and a close satellite pit with an open mouth. Street and others [71] observed a similar behaviour during their experiments. An explanation of why pits that nucleated next to each other do not necessarily grow at the same rate was given by Gou et al [68], who suggested that there is a competition among them and only one tends to grow eventually, this is due to a limited maximum cathodic current influenced by the droplet size. Additionally, this figure shows that the crystallographic etched dish is not a consequence of the propagation of an open pit mouth, being evident that the pit on the left does not have a surrounding etched dish, and the etched dished pit on the right does not have an obvious pit in its vicinities.

The disk-shape pit morphology is a common feature observed in pitting corrosion in austenitic stainless steel. There are several proposed theories to explain such phenomenon, including:

- Mair and Frankel [66] proposed that if the pit initiated at MnS site, the dissolution of such inclusions lead to Sulphur precipitation on the surface

adjacent. Such adsorbed layer increases the dissolution of metal due to a decrease in metal/metal bond strength and impedes repassivation. Resulting in a circular area around the initial defect, growing radially and downward at a constant current density.

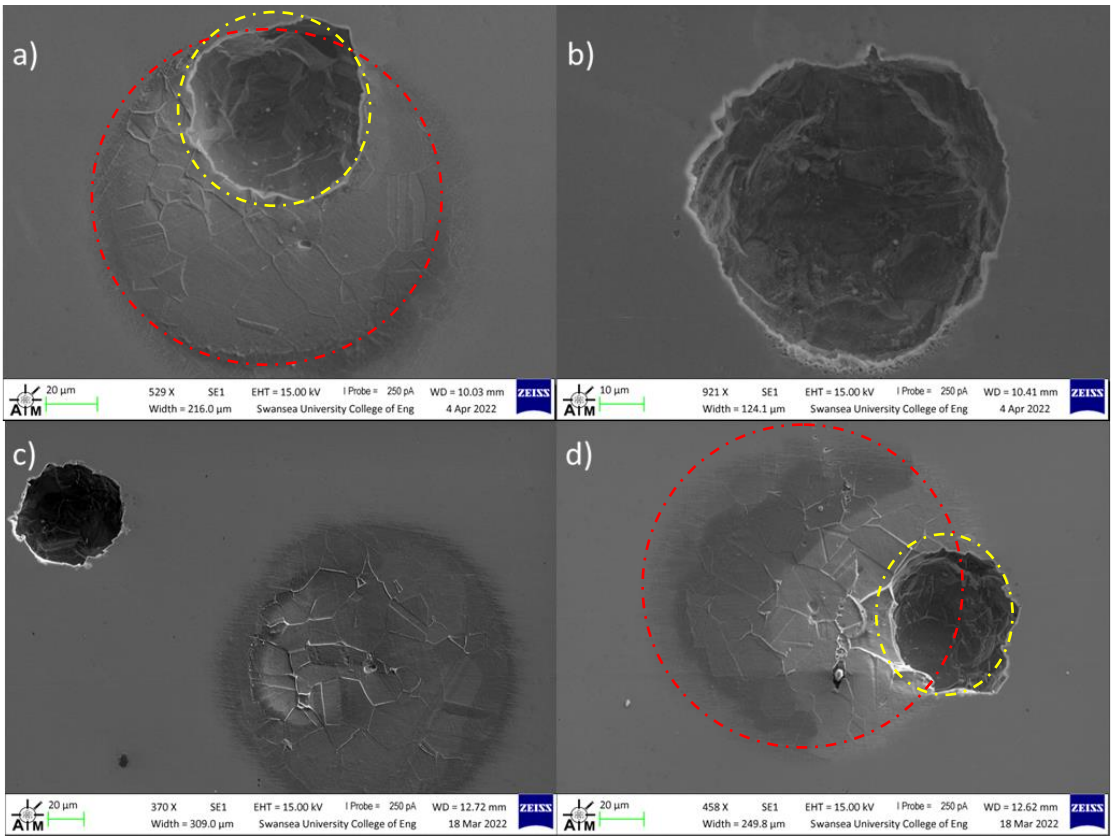

Figure 3.3 Pit morphology of SS 304 samples tested with 4 M $MgCl_2$ droplets in non-strained conditions, obtained with SEM at different magnifications: a-b) SS 304 (as received), c-d) SS 304 (sensitised).

- Hastuty and others [67], mentioned a mechanism that causes radial growth by hydrolysis of MnS inclusions after going through a thiosulfate intermediate stage, which can cause radial growth of pits for Stainless Steel 430.
- Street and others [71], proposed that the shallow dish regions grow via enhanced dissolution of the passive film, while the open pit mouth attack takes place with active dissolution of the bare metal surface. They also reported that the size of the shallow dish was affected by the location of the

pit within the droplet, however there is not an explanation regarding the circumferential morphology.

- Davenport et al. [77], reported that the morphology of atmospheric corrosion pits in austenitic stainless steel 304 was influenced by the presence of retained delta ferrite in the microstructure, with the formation of circular layered pit morphology attributed to the preferential attack of the ferrite phase, and horizontal stripes on the end grain and side grain of the plate. Such horizontal stripes were seen in some of the pits and can be seen in figure 3.3-c.

The negative effect of manganese sulphide inclusions on the pitting behaviour for stainless steels 304 is widely reported in several articles [5,33-35,66-67]. However, the experiments performed in this investigation did not include an in-depth microstructural examination. Therefore, it is not possible to confirm that the observed morphology was influenced by these inclusions, or to support the effect of retained delta ferrite on the morphology reported by Davenport et al. [77].

As mentioned above, the pit morphology of the annealed and sensitised AISI 304 samples shared some similarities. However, some of the pits that grew in the heat-treated material showed features that could not be found in the as received form. Such differences are shown in figures 3.4 and 3.5.

Comparing figures 3.4 a-b and 3.4 c-d, it is noticeable that the propagation can be different in some of the heat-treated samples. The presence of microcavities inside the pit mouth in the sensitised material (figure 3.4 c-d) suggests a vertical and non-uniform propagation (see figure 1.4). The as received material, on the other hand, appears to show a uniform wide-shallow or elliptical growth (see figure 1.4).

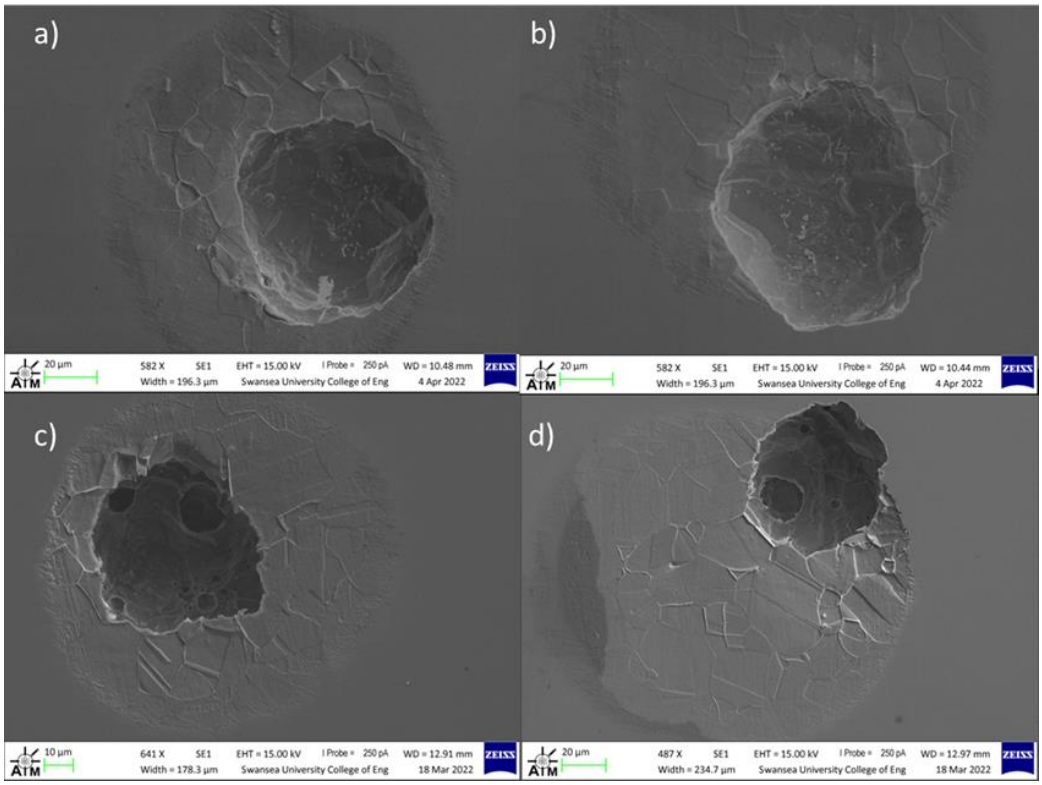

Figure 3.4 Pit morphology of SS 304 samples tested with 4 M $MgCl_2$ droplets in non-strained conditions. Obtained with SEM at different magnifications: a-b) SS 304 (as received), c-d) SS 304 (sensitised).

In the same way, figure 3.5 shows detailed pictures at grain boundaries sites for the sensitised material, confirming the presence of voids along them. These features were not observed in any of the pits nucleated in the as received specimens, and it is believed they are a consequence of the heat treatment applied.

In fact, Moore et al. [36] experiments using HS-AFM, demonstrated that $Cr_{23}C_6$ carbides can be preferentially dissolved in rich chloride solutions, leaving behind microcavities. Suggesting that voids observed in figure 3.5 are related to the chromium carbides dissolution.

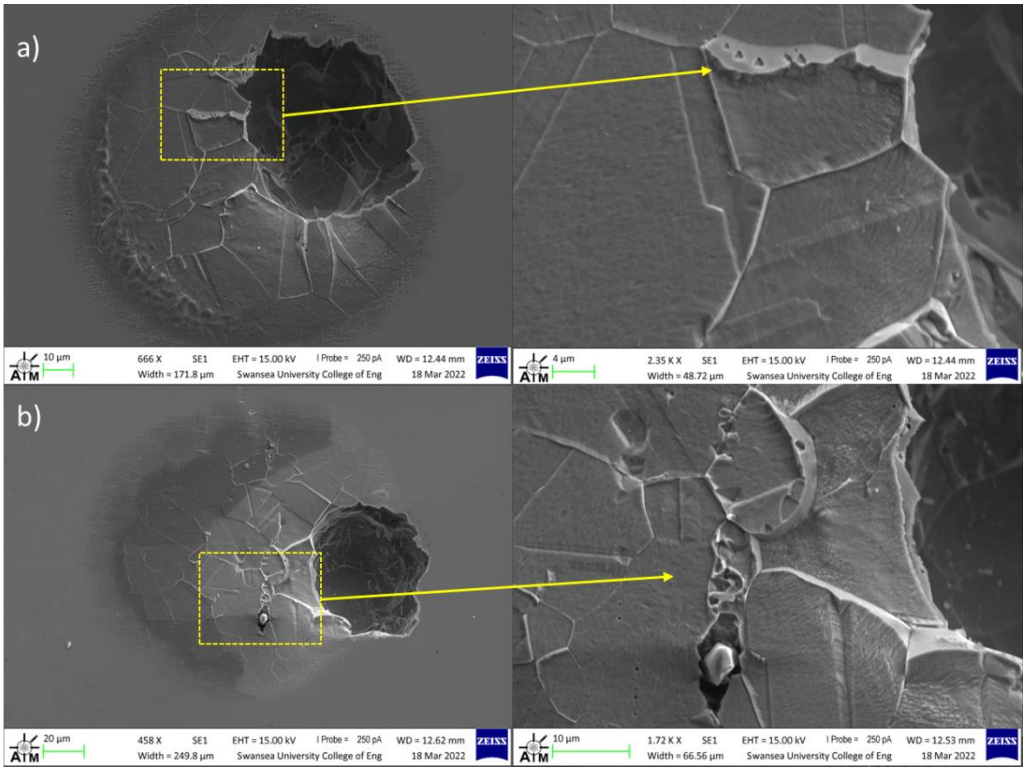

Figure 3.5 Pit morphology of sensitised SS 304 samples tested with 4 M $MgCl_2$ droplets in non-strained conditions. Obtained with SEM at different magnifications and highlighting microcavities found along grain boundaries.

3.2.2 Droplet test in strained conditions

As mentioned previously, the study of atmospheric corrosion using a droplet test is a technique widely used by several researchers studying the pitting corrosion process. However, the literature for droplet test on samples under strain is scarce, highlighting the need for new research to identify the effect of stress in the early stages of the pitting process.

The results of the droplet tests on strained conditions are summarised in tables 3.4 and 3.5. The data showed in table 3.4 reveals that the pitting process is strongly dependant on the chloride concentration of the electrolyte, exhibiting stable pitting for tests carried out in 4 M $MgCl_2$. In addition, one pit was reported in 1 M $MgCl_2$ for the sensitised sample, one pit for the as received specimen in 2 M $MgCl_2$, and surprisingly no pits were observed in 3 M $MgCl_2$ for both materials. This evidences a different behaviour to the one observed in the droplet test in non-strained conditions.

Table 3.4 Droplet test results for strained AISI 304 samples.

Droplet test @50 h 298 k	AIS 304 (As Received)	AISI 304 Thermally sensitised
1 M $MgCl_2$	0 pits in 6 droplets	1 pit in 6 droplets
2 M $MgCl_2$	1 pit in 6 droplets	0 pits in 6 droplets
3 M $MgCl_2$	0 pits in 6 droplets	0 pits in 6 droplets
4 M $MgCl_2$	6 pits in 6 droplets	10 pits in 6 droplets

Table 3.5 Average pit diameter comparison for strained AISI 304 samples.

Material	AISI 304 (As received)	AISI 304 thermally sensitised
1 M $MgCl_2$	---	70 µm
2 M $MgCl_2$	22 µm	----
4 M $MgCl_2$	132 µm ± 13 µm	6 pits: 103 µm ± 17 µm 4 pits: 21 µm ± 3 µm

The results in tables 3.2 and 3.4 suggest that samples under strain can nucleate pits at lower chloride concentrations than samples in non-strained conditions. This behaviour has also been reported by other researchers. For example, X. Zhao et al. [78] found that applied strain on duplex stainless steel 2205 decreased the critical chloride concentration for pitting and increased the pitting probability for the specimens. Y. Hou et al. [79] also found that U-bending deformation promoted the initiation, frequency, and growth rate of metastable pits in alloy 2205.

However, Jones et al. [80,81] reported that applied stress does not significantly increase the number of nucleation sites on SS 304. This is not in accordance with the results in tables 3.4 and 3.2, especially for strained sensitised samples tested in 4 M $MgCl_2$, where 10 pits were observed under 6 droplets, compared to 10 pits under 9 droplets in the non-strained condition (Table 3.2). It is important to note that the experiments by Jones et al. were carried out in immersion, with an applied potential, and at lower chloride concentrations. These factors may explain the different behaviours observed.

The reason behind the unsuccessful nucleation of pits for strained samples tested with 3 M $MgCl_2$ droplets is unclear. As mentioned previously, above 3 M $MgCl_2$, the breakdown pitting corrosion potential (E_{pit}) drops significantly [71]. Therefore, pitting would be expected for some of the samples tested at 3 M. One possibility is that manganese sulphide (MnS) inclusions were absent in the area where the droplet was deposited. Another possibility is that there were not enough Cr depleted areas at grain boundaries. Ida et al. [82] performed micro-scale polarization for a small area containing a single sensitised grain boundary without sulphide inclusions in 0.1 M NaCl. In their experiments, no pitting was observed at the sensitised grain boundary during polarization, suggesting that such inclusions are required for pitting to initiate. The absence of a detailed microstructural analysis in the present work meant it was not possible to verify the presence of MnS on the surface of the samples and correlate these results.

Regarding the results reported in table 3.5, it is noticeable that the pits nucleated on samples with concentrations lower than 4 M $MgCl_2$, had a smaller diameter. In addition, the heat treatment seems to influence more the number of pits than the diameter in tests performed at 4 M $MgCl_2$. In fact, specimens in the as-received condition had larger average diameters. A possible explanation for this behaviour might be that the competition between pits that nucleated under the same droplet not just limits it is propagation, it might also influence their diameter.

The micrographs showing the different morphologies obtained for droplet tests on samples under the effect of strain, are shown in figures 3.6 and 3.7.

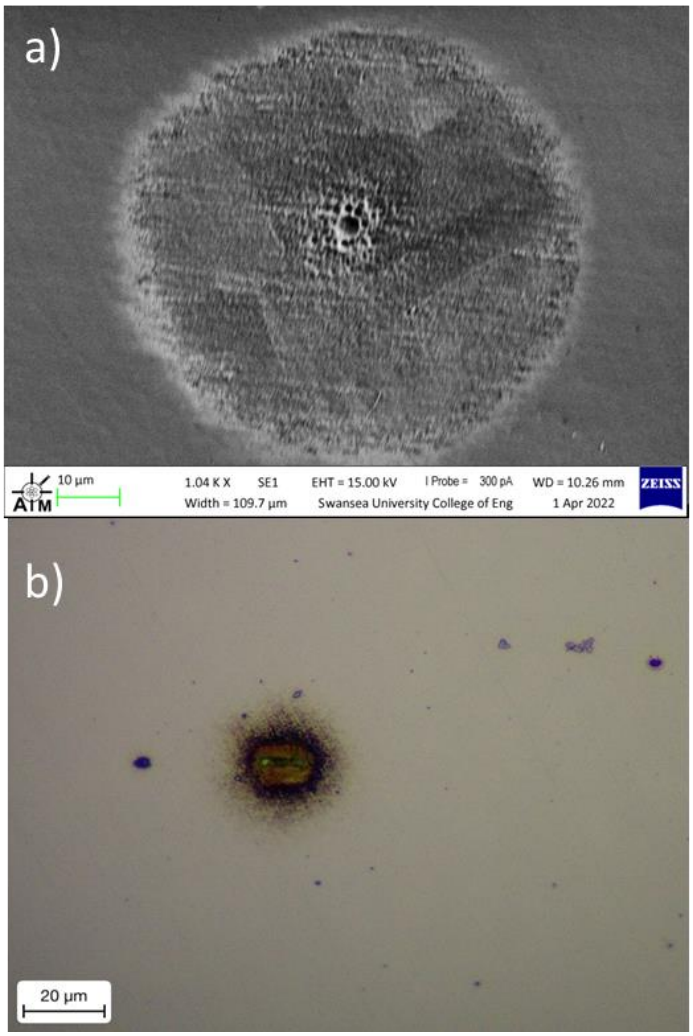

Figure 3.6 Pit morphology of SS 304 samples under strained conditions, a) 1 M $MgCl_2$ (sensitised) obtained with SEM, b) 2 M $MgCl_2$ (as received) obtained with an optical microscope (50X).

Analysing figure 3.6-a, it is perceptible that the pit initiated in the heat treated sample in 1 M $MgCl_2$ formed a shallow dish region with slightly crystallographic etching. The lack of material removal suggests that the pit was not active for a long period of time and repassivated shortly after initiation. Regarding the cluster of microcavities that can be seen inside one of the grains, an EDS performed failed to detect any traces of previous material present, therefore is not possible to determine if such voids were occupied by an inclusion.

Figure 3.6-b shows the pit obtained in the as-received conditions tested in 2 M $MgCl_2$. Again, the absence of material removal suggests that the pit repassivated soon after initiation.

The pits observed in strained samples tested with 4 M $MgCl_2$ droplets, share a similar morphology to the ones tested in the absence of strain. Once again, the heat treatment condition seems to have an influence on the number of pits nucleated but has a limited impact on the pit shape. Some of the pit morphologies observed for the strained samples are shown in figure 3.7.

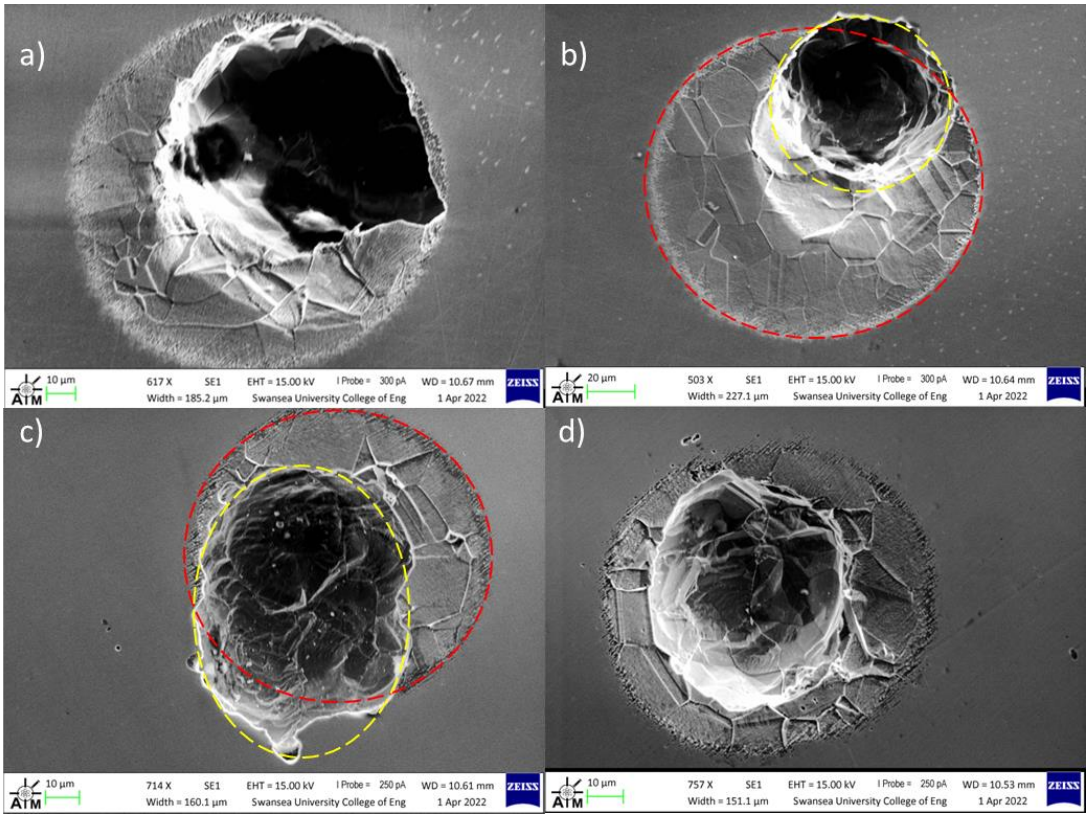

Figure 3.7 Pit morphology of SS 304 samples tested with 4 M $MgCl_2$ droplets in strained conditions, obtained with SEM at different magnifications. a-b) SS 304 (as received), c-d) SS 304 (sensitised).

Analysing figure 3.7, it is distinguishable that the pits obtained had the same disk-shape morphology with crystallographic etching (red dashed line in figure 3.6 b-c) observed in non-strained conditions (figure 3.3). Similarly, the propagation of the pits can be inside the disk-shape (figure 3.6-a-d) or outside (figure 3.6 b-c).

Regarding the number of pits nucleated in the sensitised samples tested with 4 M $MgCl_2$, it was observed that at least 2 of the droplets nucleated more than one pit. Once again, the multiple pit nucleation consisted in a colony of pits, with different diameters and depth, where one of the pits showed crystallographic etching and

others an open mouth. Such behaviour has been reported by other authors [71,83], and can be seen in figure 3.8.

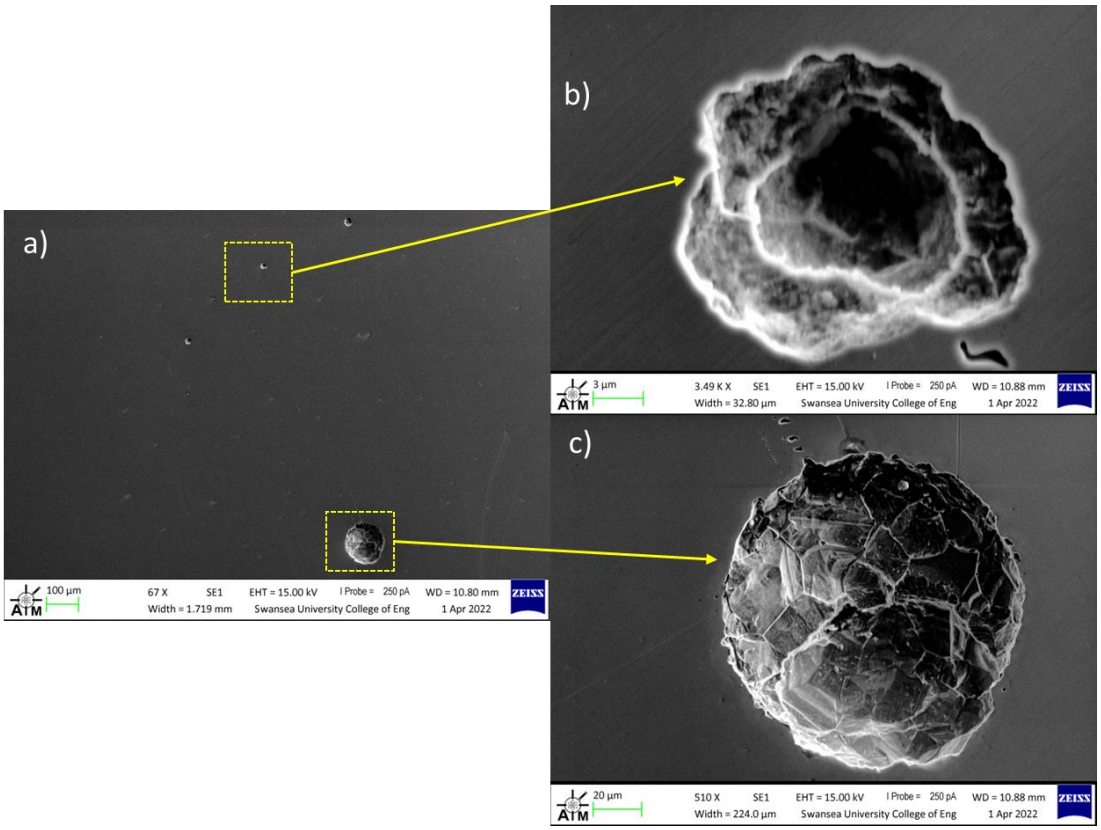

Figure 3.8 Pit morphology of SS 304 sensitised tested with 4 M $MgCl_2$ droplets in strained conditions, obtained with SEM at different magnifications. a) Colony of pits, b) Satellite pit, and c) Pit with crystallographic etching.

The presence of microcavities at the grain boundaries of sensitised material shown in figure 3.5, was also detected in the sensitised strained samples (figure 3.9). This reinforces the assumption that such cavities are a consequence of the heat treatment due to formation of chromium carbides that are preferentially dissolved in a chloride-rich environment [36].

Nakao et al. [84], performed similar droplet test experiments in sensitised and strained AISI 304 samples. In their investigation they deposited 20 mL droplets of 250 mM $MgCl_2$ at 35% RH and 50° C, such tests were performed for 72 hours. They reported that once the droplet evaporates it reached an equilibrium state in the chamber with a 10 M concentration, initiating pitting within the first hour. The

appearance of tiny cracks was reported after 12 h, which propagated normal to the tensile strain for the entire duration of the experiment.

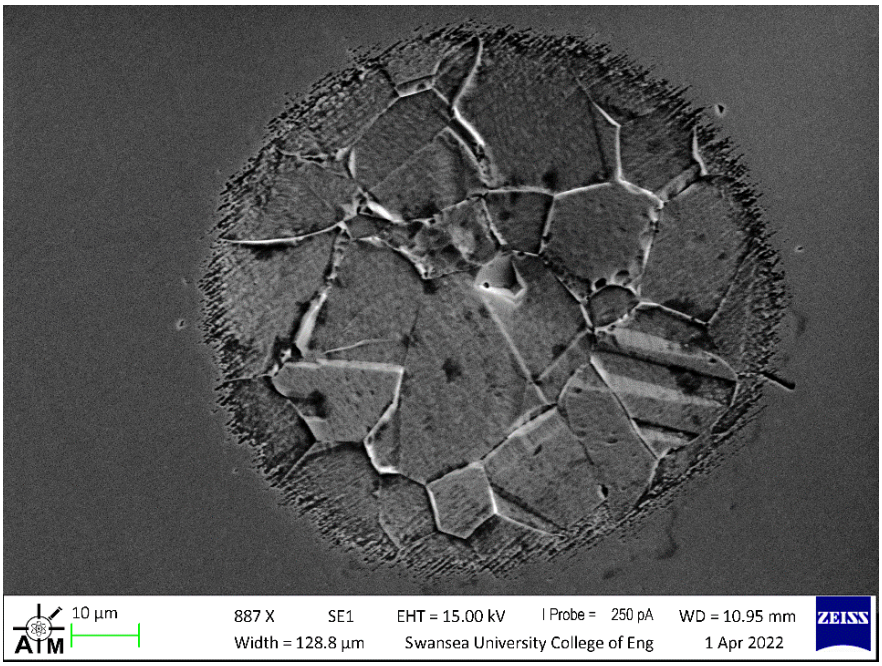

Figure 3.9 Pit morphology of SS 304 sensitised sample tested with 4 M $MgCl_2$ droplets in strained conditions, obtained with SEM.

Opposite to Nakao et al. results [84], the experiments performed in this research project failed to observe clear signs of cracking in the vicinity of the pit under strain conditions. Although some microcavities next to the pit can be seen figure 3.7-d or 3.8-b and c, there is not enough evidence that they are related to a cracking phenomenon.

The probability of observing stress corrosion cracking (SCC) in SS 304 under the effect of 'wetted' salts on U-bend specimens has been studied by different authors [85-91]. In their experiments, several parameters were controlled (salt deposition, RH, temperature, time, etc). Shoji and Ohnaka [86-88], performed their tests at room temperature for 24 months and observed SCC, while Prosek et al. [91] performed tests for 10 weeks reporting no SCC at 20 °C, and observing cracking if the temperature was increased to 30 or 40 °C. Therefore, it seems reasonable that droplet tests performed at room temperature would not show signs of cracking after just 50 h of testing, even though the electrolyte has a high chloride concentration and some of the samples were thermally sensitised.

3.2.3 Pitting process during droplet test

Although the localised corrosion behaviour within a droplet is well known to be influenced by differential aeration, characterised by cathodic activity located at the perimeter and anodic activity in the centre [64], in reality for the experiments performed here this did not seem to influence the location of the pits.

In fact, observing the pitting process with the microscope proved to be a challenging task because it was highly dependent on the location of the pit inside the droplet. It was noticed that most of the pits grew in between half the radius and the rim of the droplet, making it impossible to observe their development.

Fortunately, some of the pits nucleated in the sensitised material in non-strained conditions with 4 M $MgCl_2$, were located at the centre and the process could be observed at different stages. The results are shown in figure 3.10.

The time frame between droplet deposition and microscope surveillance was 1 to 5 minutes. As can be seen in figure 3.10-a, pitting had already been initiated by then, suggesting that 4 M $MgCl_2$ droplets can produce pitting soon after deposition. Analysing figure 3.10-a, it is notable that the formation of the disk-shape pit morphology without clear signs of crystallographic etching. Corrosion products can also be sighted at some distance from the pit.

After 24h of testing (figure 3.10-b), the characteristic crystallographic etching is evident and there are no further signs of diameter change or growth. In addition, it is noticeable that a second pit has formed in the vicinity, which seems to be in a more advance stage of growth. Once again, corrosion products seem to be located at a distance from both pits.

After 50 hours (figure 3.10-c), there is no apparent change in either pit. Analysing the process, it seems that the first pit repassivated at some point after the crystallographic etching. Regarding the second pit, the diameter remained unchanged, however it cannot be determined if it was still active. The figure also shows how the corrosion products are deposited at a radial distance from the pits.

Figure 3.10-d, was obtained with the SEM after the corrosion products were removed with oxalic acid 10% w/v, proving that such cleaning procedure did not alter the morphology of the pits.

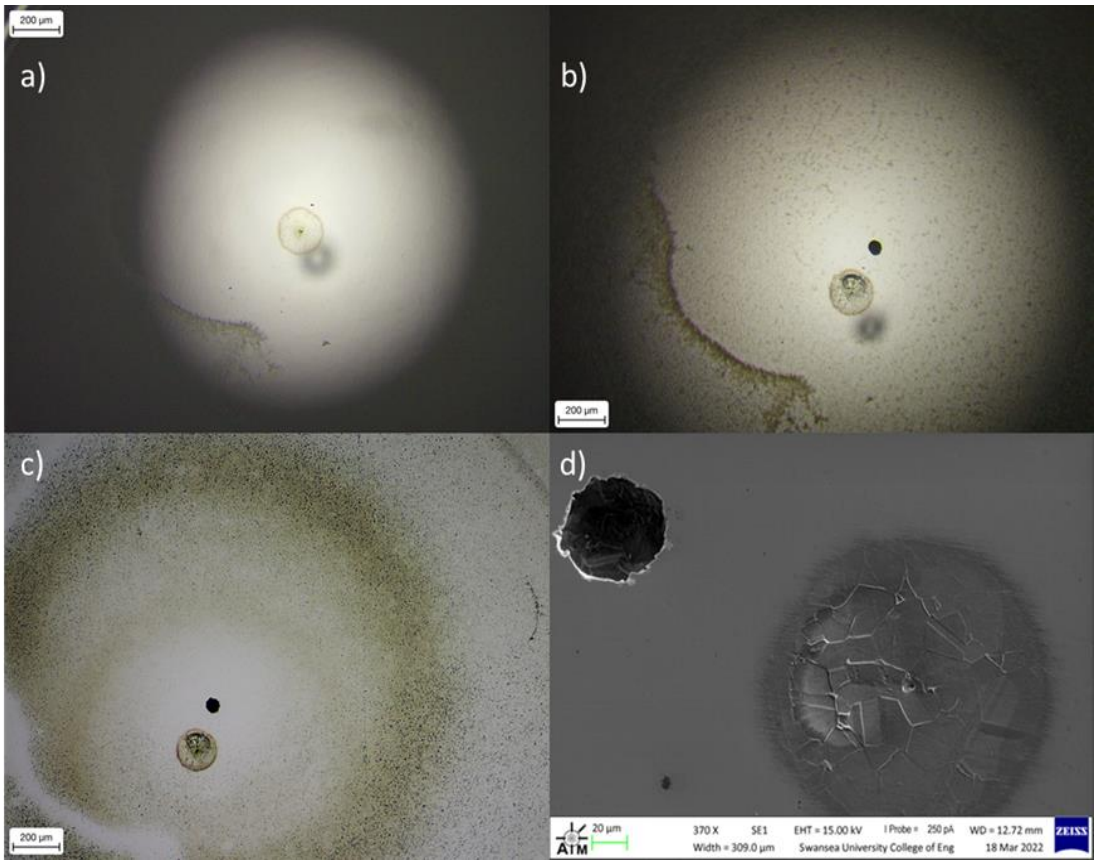

Figure 3.10 Different stages of the pitting process for the thermally sensitised SS 304 in non-strained condition tested with 4 M $MgCl_2$ droplets, a) at 0 h, b) at 24h, c) after 50 h, d) after cleaning with oxalic acid 10% w/v (obtained with SEM and rotated 90 °).

3.2.4 Uniaxial tensile test on samples with pits nucleated on surface

Uniaxial tensile test on samples with pits nucleated on the surface were performed for AISI 304 samples in the as received and thermally sensitised condition. The aim of this experiment was to observe if a single pit nucleated for a period of 50 hours using 4 M $MgCl_2$ droplets could influence the results for the mechanical properties and fracture mode of the samples.

The results of the mechanical test results are shown in table 3.6 (which also includes the values obtained in table 3.1) and images of the pits before and after the tensile test are shown in figure 3.12.

Comparing the results on table 3.6, it can be noted that samples that had a pit on the surface in the as received condition had an average yield point slightly higher (325 MPa vs 296 MPa), while the maximum elongation (0.68 vs 0.73) and the UTS (675 MPa vs 680 MPa) values were slightly lower.

Regarding thermally sensitised samples, the results for specimens tested with a pit nucleated on surface, had similar average values to the same material without a pit. The yield point was slightly lower (270 MPa vs. 276 MPa), while the UTS (682 MPa vs 674 MPa) and the maximum elongation (0.69 vs 0.65) were slightly higher.

Table 3.6 Tensile test results for AISI 304 (as received and sensitised) on samples with and without a pit nucleated on the surface.

Material	Yield point (MPa)	UTS (MPa)	Max. elongation
AISI 304 as received	296 ± 61	680 ± 39	0.73 ± 0.06
AISI 304 as received (with pit)	325 ± 21	675 ± 26	0.68 ± 0.04
AISI 304 thermally sensitised	276 ± 46	674 ± 13	0.65 ± 0.05
AISI 304 thermally sensitised (with pit)	270 ± 80	682 ± 56	0.69 ± 0.04

Even though the results reported in 3.6 reveal some differences for both materials, once the average results are compared considering the error reported, the influence of a single pit on the surface did not significantly influence the mechanical properties of the metal. This was also evident after analysing the fracture area of the samples and noting that none of the nucleated pits were involved in the fracture of the sample, as can be seen in figure 3.11.

It is known in the fracture mechanics theory that a minimum crack size is needed for the crack to propagate in a material under a given set of loading conditions. Therefore, the results obtained in table 3.6 and figure 3.11, suggests that the pit nucleated for a period of 50 hours with a 4 M $MgCl_2$ droplet did not reach the minimum critical size to propagate during the tensile test for both materials.

In the same way, the lack of cracking on strained samples during the droplet test (section 3.1.2) could be attributed to a similar reason, the pit did not grow large enough in 50 hours for cracks to emerge.

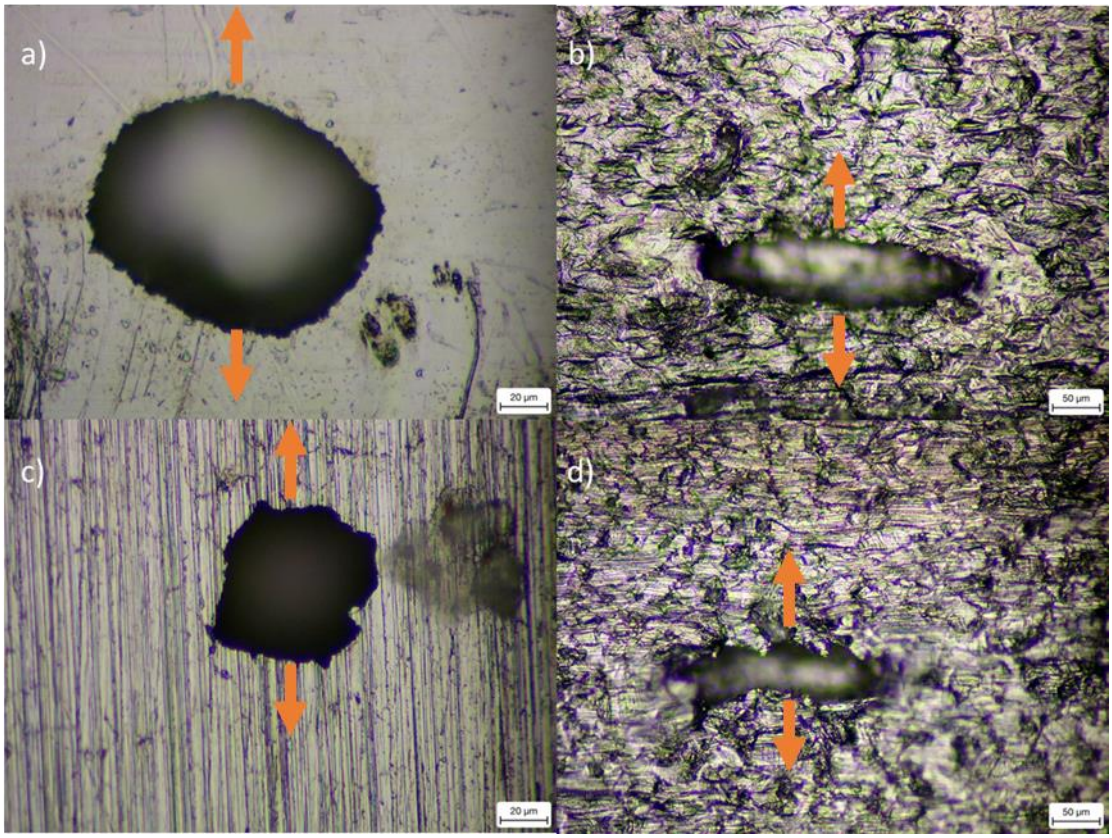

Figure 3.11 Pits nucleated on the surface of AISI 304 uniaxial tensile test specimens obtained with an optical microscope at different magnifications, a) Pit on as received material before the test, b) Pit on the as received material after the test, c) Pit on the sensitised sample before the test, d) Pit on the sensitised sample after the test. The orange arrows exemplify the tensile load applied during the test.

3.3 DC Electrochemical experiments

To obtain additional information on the effect of applied strain on the corrosion behaviour of stainless steel 304 in annealed and thermally sensitised conditions, potentiodynamic polarisation experiments were performed in 1 M NaCl, following the procedure described in section 2.5. A comparative data set of the behaviour observed is shown in figures 3.12 and 3.13.

Analysing figure 3.12, it is noticeable that for the as received sample, the application of strain reduced E_{corr} slightly, while having a more significant effect on the pitting potential (E_{pit}), which is reduced by at least 40 mV when strain is applied. Regarding the current density reported, the corrosion current density (I_{corr}) and the

critical pitting current density ($I_{critical}$) are higher for the strained sample. In the same way, it is shown that short-lived current transients in the passive region for both materials, however, they initiated at lower potentials for the strained material. These transients are commonly associated to metastable pitting due to the rupture of the passive Cr oxide film.

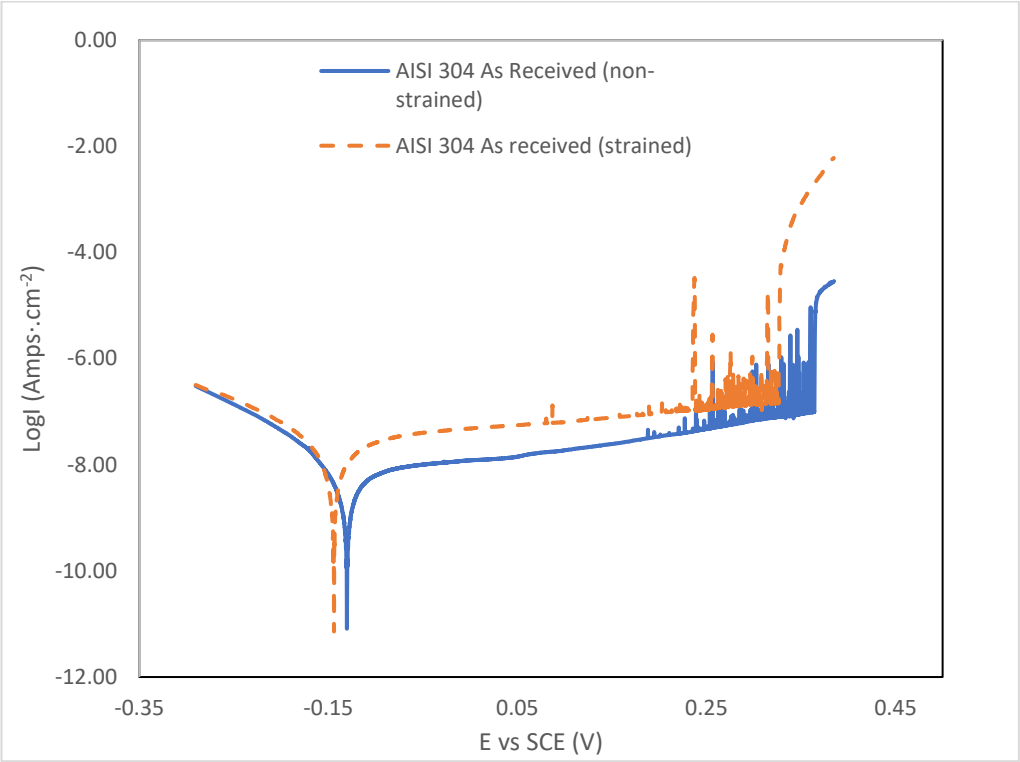

Figure 3.12 Potentiodynamic polarisation curves of AISI 304 in the as received condition in 1 M NaCl, for strained and non-strained samples.

On the other hand, figure 3.13 shows a similar behaviour for the sensitised sample. The strained specimen had a lower value of E_{corr} and E_{pit} was at least 70 mV lower. The values of current density were higher for the samples under load. Once again, current transients in the passive region can be seen at lower potentials for the samples under strain, even though the non-strained specimen showed larger current transients.

The notable decrease in the pitting potential for strained samples and the appearance of transients in the passive region at lower potentials, both independently of the heat treatment condition of the material, suggests that the

nucleation of non-stable pits at lower concentrations observed in the droplet test (section 3.1.1 and 3.1.2) was induced by the strain applied.

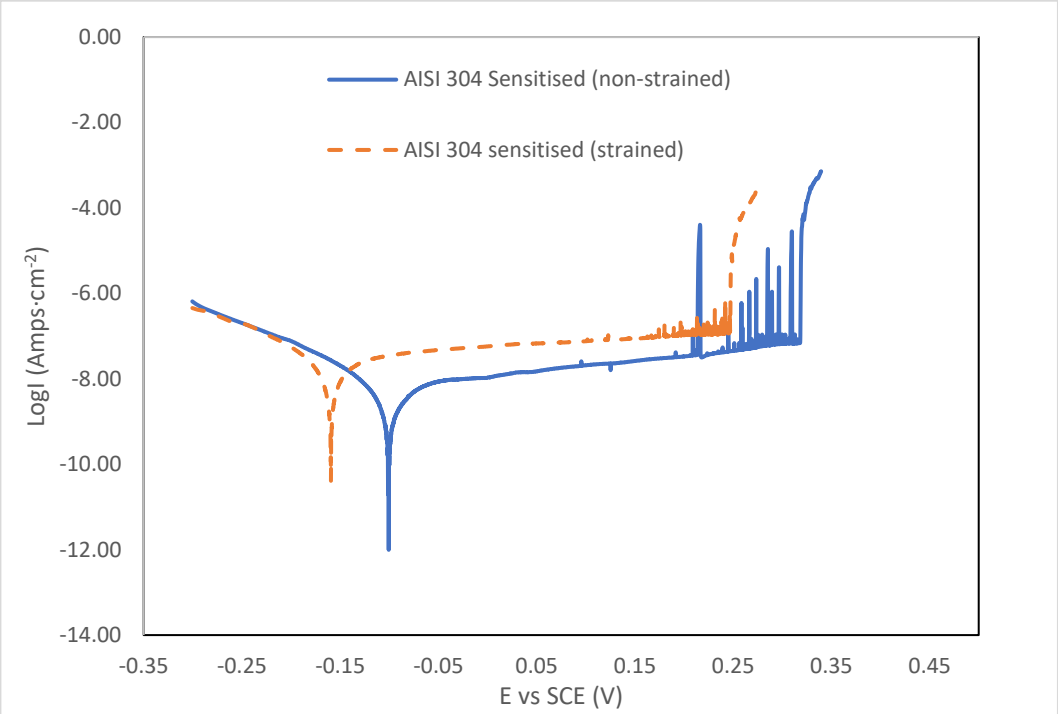

Figure 3.13 Potentiodynamic polarisation curves of AISI 304 in the thermally sensitised condition in 1 M NaCl for strained and non-strained samples.

The results shown above provide evidence that the pitting potential (E_{pit}) of thermally sensitised specimens decreases regardless of the strain applied, making them more susceptible to pitting. This is in accordance with other studies [75].

The results obtained in figures 3.12 and 3.13 are summarised in table 3.7, which shows that the strain applied also influence the change of potential 'ΔE' (E_{pit}-E_{corr}). This value is lower for samples under strain when compared with the non-strained specimens in the same heat treatment condition. Similarly, the results evidence that the sensitisation heat treatment decreases ΔE.

Table 3.7 Potential values obtained for AISI 304 annealed and thermally sensitised under strained and non-strained conditions in 1 M NaCl.

Material	AISI 304 as received non-strained	AISI 304 as received strained	AISI 304 sensitised non-strained	AISI 304 sensitised strained
E_{corr}	-130 mV	-144 mV	-101 mV	-159 mV
E_{pit}	364 mV	324 mV	318 mV	247 mV
ΔE	494 mV	468 mV	419 mV	406 mV

3.4 Scanning Vibrating Electrode Technique

The scanning vibrating electrode technique has previously been used by researchers to map the localised corrosion process in different alloys and conditions [6,52,92-96]. The current density maps obtained with this technique illustrate the anodic and cathodic reactions as they occur on the surface of a metal, allowing the development of the corrosion process to be observed over time.

The literature available employing SVET in samples under the effect of strain is quite scarce and just a few publications are available in corrosion scientific journals. A brief mention of such experiments can be seen below:

- Isaacs [6] was probably the first author to report the use of this technique to detect the appearance of cracks in SS 304 sensitised under strained conditions.
- Uchida and colleagues [95], were able to map the location of cracks in a single crystal of SS 304 under the effect of an external load using the SVET.
- Manhabosco et al. [96] used the SVET to study the behaviour of hot dip galvanised steel immersed in 0.01 M NaCl solutions, comparing the behaviour between pre-strained and strained samples.

Taking into consideration that the droplet tests results suggested that the concentration threshold whereby spontaneous formation of pits without external polarisation was above 3 M $MgCl_2$. It was decided that the experiments performed with SVET would be carried out in 3 M and 4 M $MgCl_2$ solutions, in full immersion conditions without external polarisation.

However, the SVET experiments performed on samples immersed in 3 M $MgCl_2$ did not show any sign of pitting, independently of the heat treatment condition or applied strain. The lack of pitting in immersed samples for 3 M $MgCl_2$, in contrast to the results observed for droplet tests, can be explained due to the absence of a differential aeration cell in full immersion conditions. For this reason, the obtained current density maps are not reported as they do not show any relevant information.

3.4.1 SVET experiments in 4 M $MgCl_2$

In contrast to the behaviour observed in samples immersed in 3 M $MgCl_2$, the tests performed in 4 M $MgCl_2$ resulted in the nucleation and growth of pits at the metal surface in all the configurations tested. The development of the pitting process was followed using the SVET technique, and the current density maps obtained are shown in figures 3.14, 3.16, 3.18 and 3.20.

The maps show the anodic activity (positive current density) represented in red, cathodic activity (negative current density) in blue, and neutral zones (near zero current density) in white. Post-examination of the samples confirmed pits in the same location of the anodic regions represented in the maps.

3.4.1.1 SVET - AISI 304 as received in non-strain and strained conditions

Analysing the current density maps for AISI 304 in non-strained (figure 3.14) and strained condition (figure 3.16), a large anodic peak was formed during the first scan, indicating that pitting corrosion started soon after immersion, regardless of the strain condition. It is important to highlight that for the strained sample, the pit nucleated next to the PTFE tape, suggesting some crevice influence. In the same manner, the strained sample showed a second anodic region of lower magnitude that can be observed in figure 3.16-a.

The successive scans completed afterwards showed a peak of current density at the same anodic location, however, the magnitude had a clear tendency to decrease. In fact, the second anodic region observed in the strained sample disappeared after the first scan, suggesting that it repassivated after initiation. The reduction of

activity in the different scans is also noticeable for cathodic regions in both materials.

The evolution of the maximum current density value in the anodic region is shown in figure 3.15 for the non-strained sample and figure 3.17 for the strained material.

Observing figures 3.15-a and 3.17-a it is noticeable that the maximum values decrease with the time and converge to a particular location in the *x*-direction, which might be linked to the pit propagation. A more detailed observation of this phenomenon is shown in figures 3.15-b and 3.17-b, where the peak current density is plotted through the duration of the experiment.

Figure 3.15-b shows how the current density in the non-strained material decreases sharply from ≈6.5 Am^{-2} to ≈1.5 Am^{-2} after just 1 hour of testing, with little variations through the rest of the experiment.

Regarding the strained sample, figure 3.17-b reveals that even though the current density values obtained are lower in magnitude compared to the non-strained specimen, the decrease is smoother through the time, suggesting a strain effect in the corrosion phenomenon and current density measured.

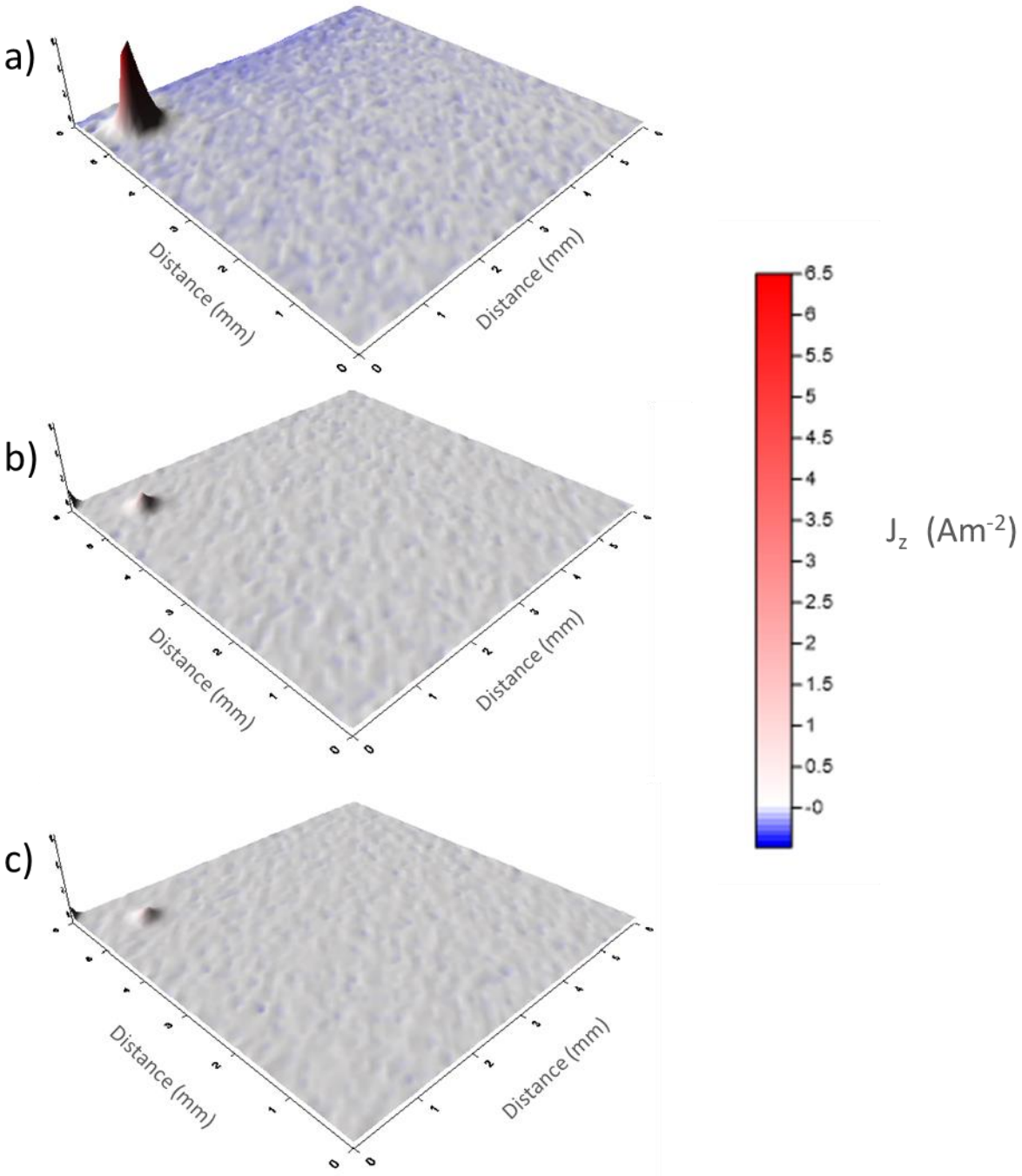

Figure 3.14. SVET current density maps for AISI 304 as received in non-strained conditions, immersed in 4 M $MgCl_2$, a) 0h, b) 6h, c) 24h.

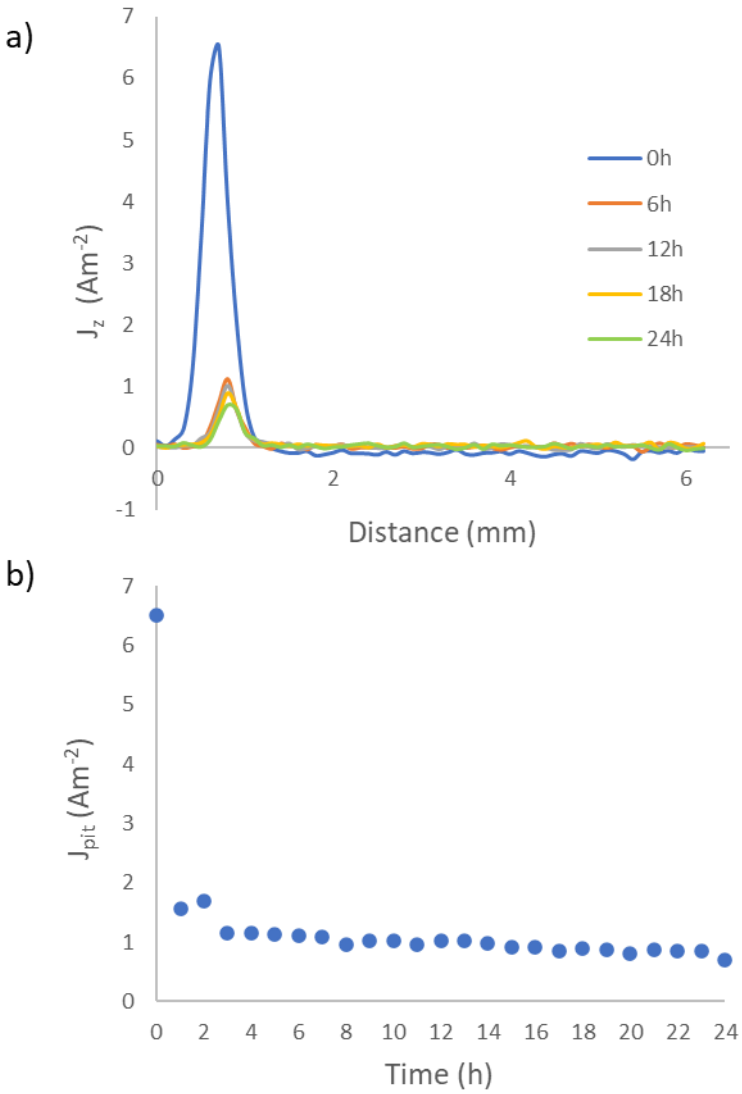

Figure 3.15. Evolution of SVET current density measurements (J_z) for AISI 304 as received in non-strained condition. a) Current density values in the cross-section of the highest anode location taken at different times, b) Maximum current density at the pit as a function of the time.

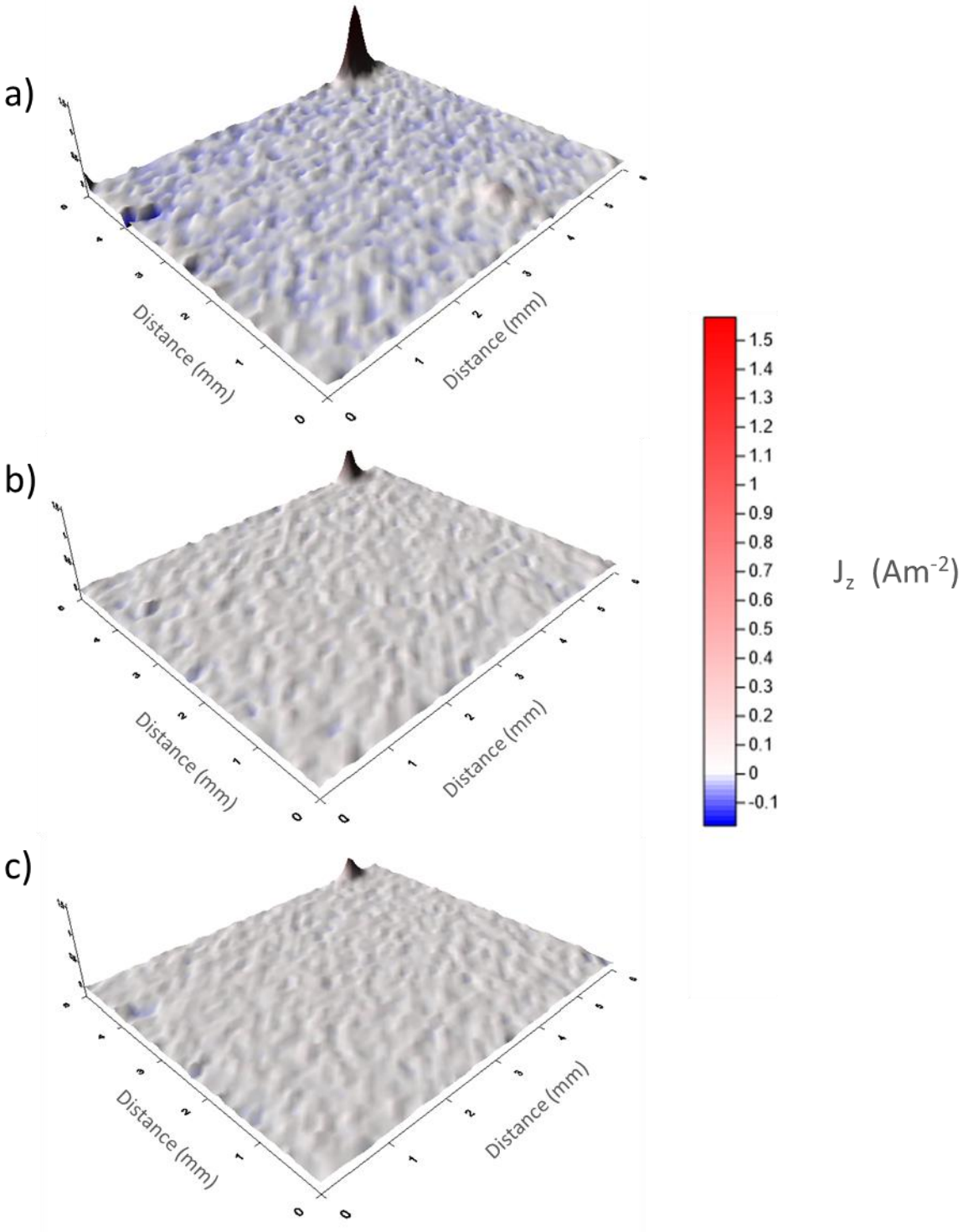

Figure 3.16. SVET current density maps for AISI 304 as received in strained condition immersed in 4 M $MgCl_2$, a) 0h, b) 6h, c) 24h.

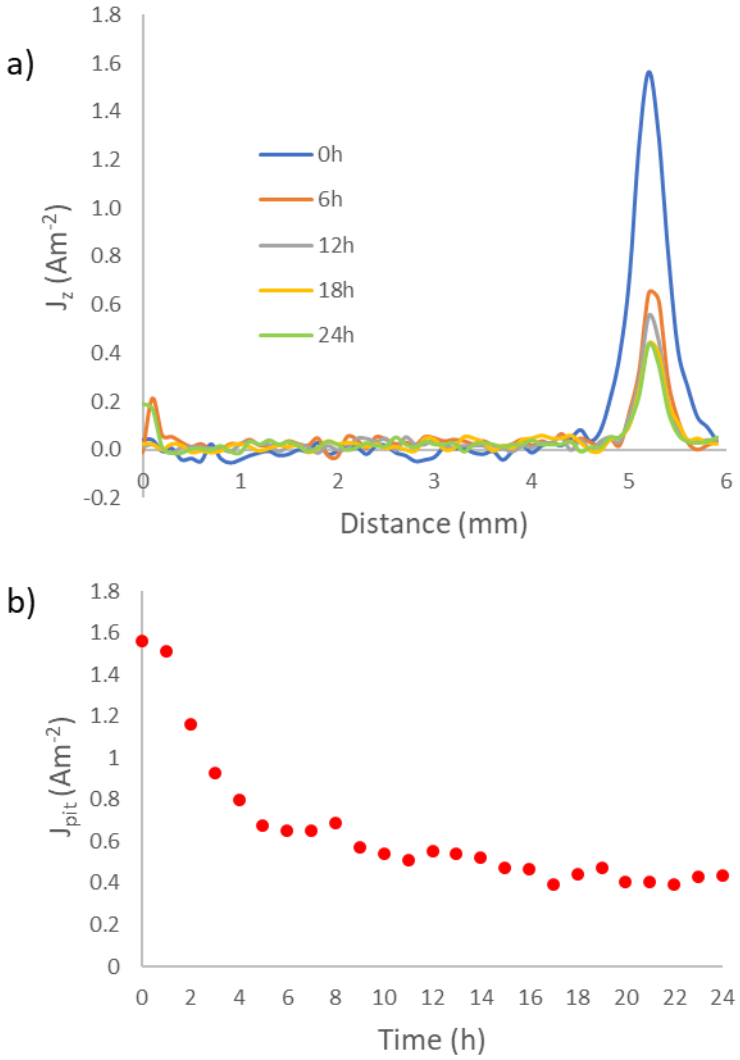

Figure 3.17. Evolution of SVET current density measurements (J_z) for AISI 304 as received in strained condition. a) Current density values in the cross-section of the highest anode location taken at different times, b) Maximum current density at the pit as a function of the time.

3.4.1.2 SVET - AISI 304 sensitised in non-strain and strained conditions

Similarly to the as received material a prominent anodic peak was observed during the first scan of the non-strained metal, with successive decrease of its magnitude as shown in figure 3.18. However, the strained sample (Figure 3.20) showed a different behaviour, and no localised corrosion was seen at 0 h. The pitting process started in between the first and the second scan, and it was not possible to determine the exact time of its appearance. Once again the magnitude of this peak

decreased over time. The reduction of activity in the cathodic regions can be also appreciated for both materials.

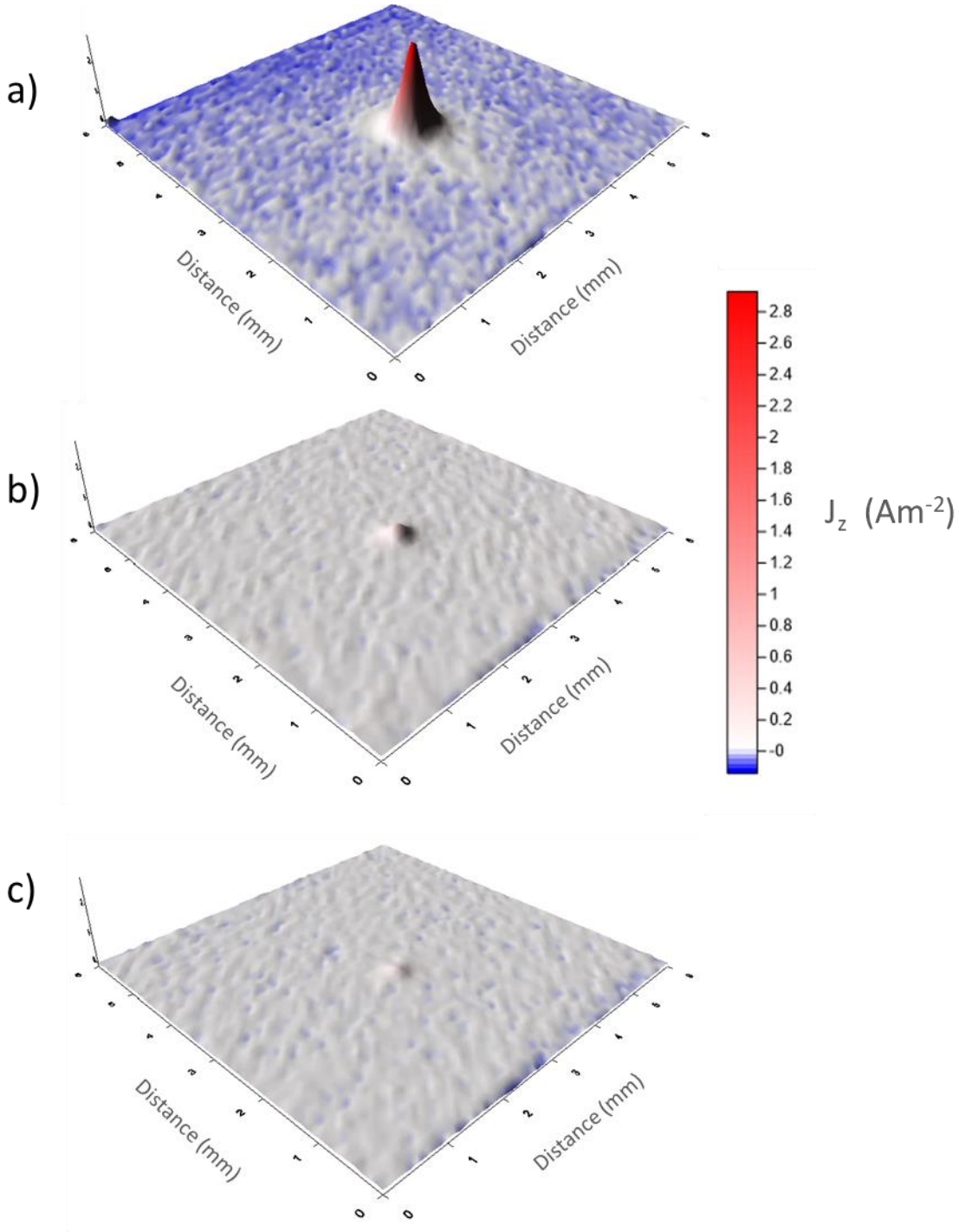

Figure 3.18. SVET current density maps for AISI 304 sensitised in non-strained condition immersed in 4 M $MgCl_2$, a) 0h, b) 6h, c) 24h.

No additional anodic areas were observed in the current density maps, even though post examination determined the presence of some additional pits. The morphology of such pits, in addition to the non-detection of their anodic current, suggests that they repassivated soon after initiation.

The evolution of the maximum current density values for the anodic region is shown in figure 3.19-a for the non-strained sample and figure 3.21-a for the strained material. Similarly to the as received material, the current density peaks decreased over time and appeared to converge to a location.

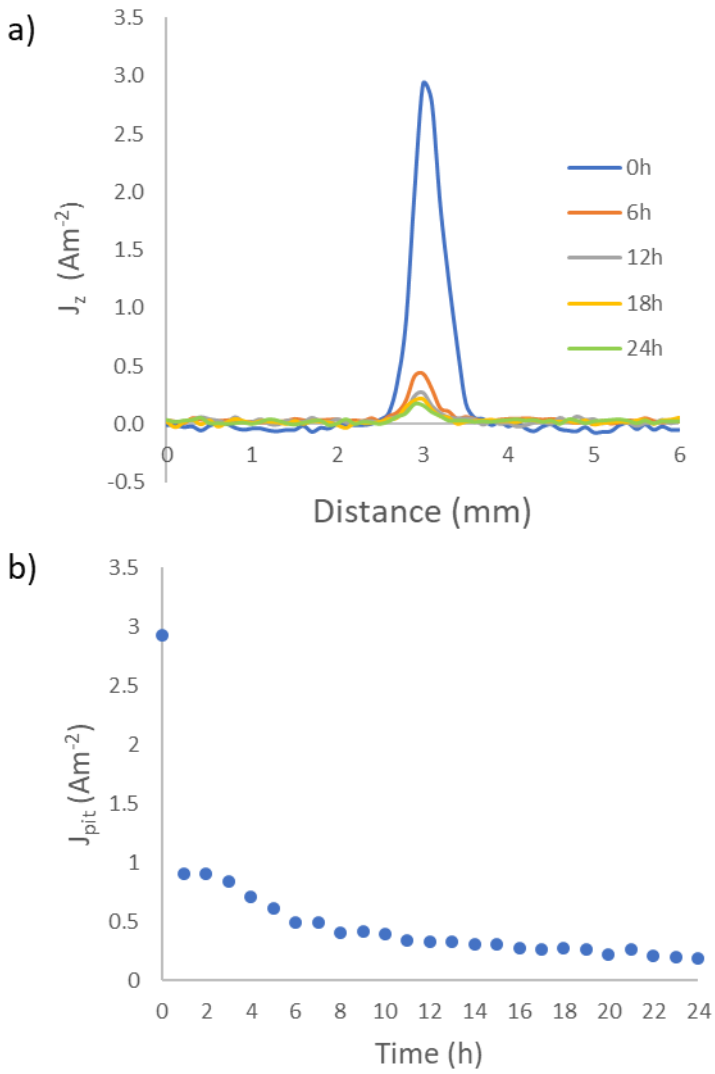

Figure 3.19. Evolution of SVET current density measurements (J_z) for AISI 304 sensitised in non-strained condition. a) Current density values in the cross-section of the highest anode location taken at different times, b) Maximum current density at the pit as a function of the time.

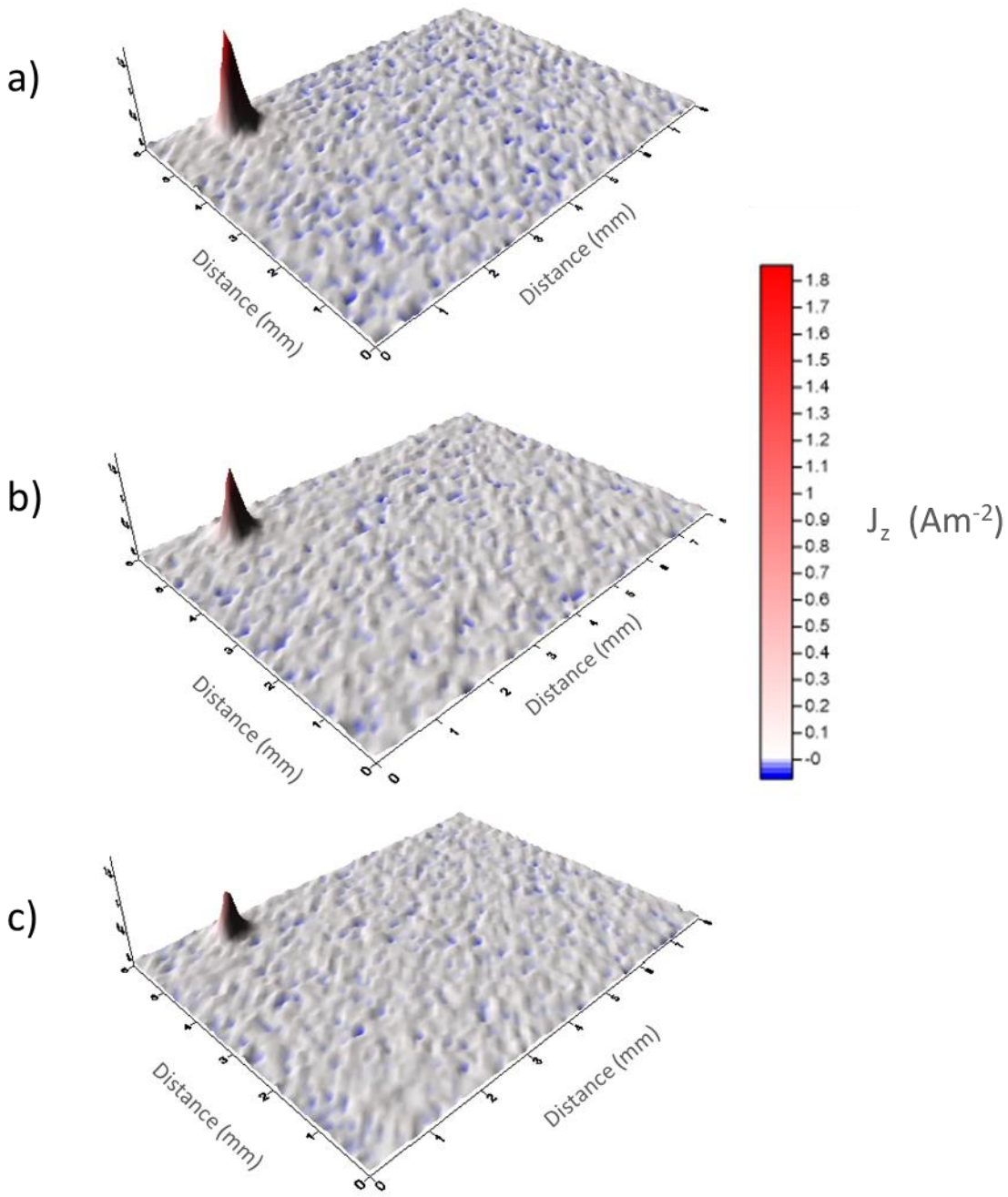

Figure 3.20. SVET current density maps for AISI 304 sensitised in strained condition immersed in 4 M $MgCl_2$, a) 1h, b) 6h, c) 24h.

Once again, the maximum peak value measured per scan showed a sharp decrease after the first hour for the non-strained material (figure 3.19-b). While the strained sample (figure 3.21-b) had overall a smooth decrease and even some increments of current density are appreciated between 6 and 10 hours, suggesting that the applied load was influencing the corrosion reactions on surface.

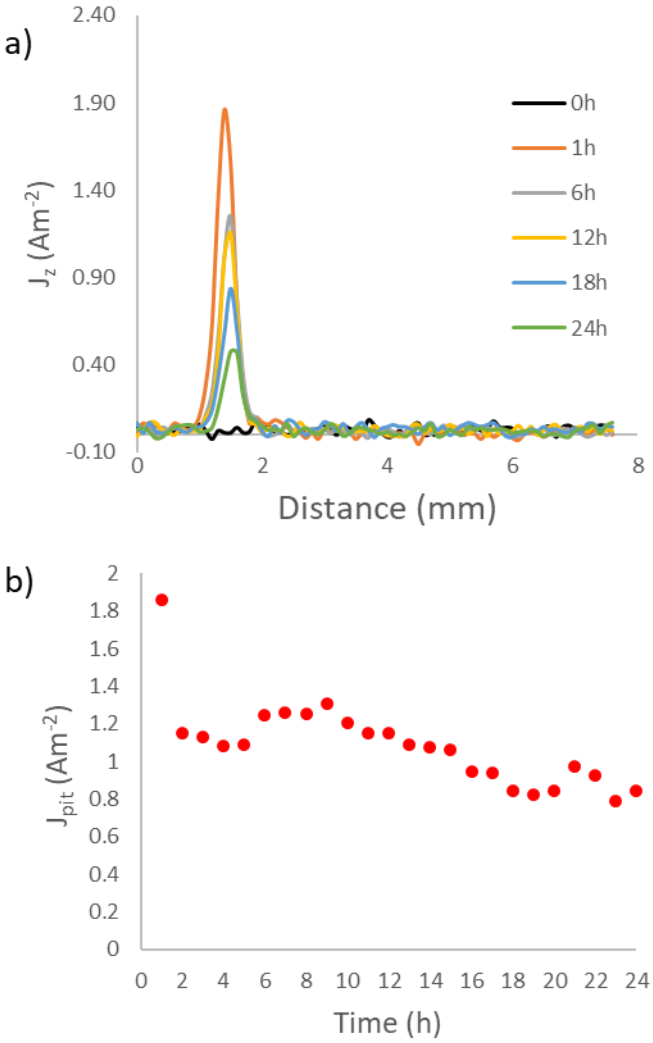

Figure 3.21. Evolution of SVET current density measurements (J_z) for AISI 304 sensitised in strained condition. a) Current density values in the cross-section of the anode location taken at different times, b) Maximum current density at the pit as a function of the time.

A recurring observation across all SVET current density maps, regardless of the tested condition, is a decrease in anodic activity over time. Since the cathode area remains constant, this phenomenon must be attributed to changes at the anode itself. A possible explanation is the precipitation of corrosion products near the pit mouth or repassivation of the surrounding area due to pH shifts. These products could impede ionic transport from the active pit-propagation front to the surface cathodes, thereby reducing the overall reaction rate overtime.

3.4.2 Pit morphology obtained during the SVET experiments

The pit morphology obtained during the SVET experiments for all the conditions tested can be divided into two categories. Pits that nucleated and remained active through the duration of the experiments (Figure 3.22) and pits that nucleated but repassivated (Figure 3.24).

Observing figure 3.22 it is noticeable that there are some similarities between the pits obtained in samples under immersion and those reported on the droplet test in 4 M $MgCl_2$. A disk-shaped area with evident crystallographic etching next to the propagation region of the pit can be observed in all the samples tested.

However, the diameters are significantly different between droplet test and immersion conditions, with the pits obtained in immersion at least 3 times larger. This may be attributed to the difference in exposed area. In the droplet tests, the pits that nucleated had a smaller cathodic region to sustain their growth, as well as limited electrolyte.

The current density measurements reported in figures 3.15-a, 3.17-a, 3.19-a and 3.21-a, suggested that the pit dimensions decreased with time. The pit morphology observed in figure 3.22 shows spiral attack that seems to converge into the propagation region of the pit for every material. Therefore, both behaviours seem to be related.

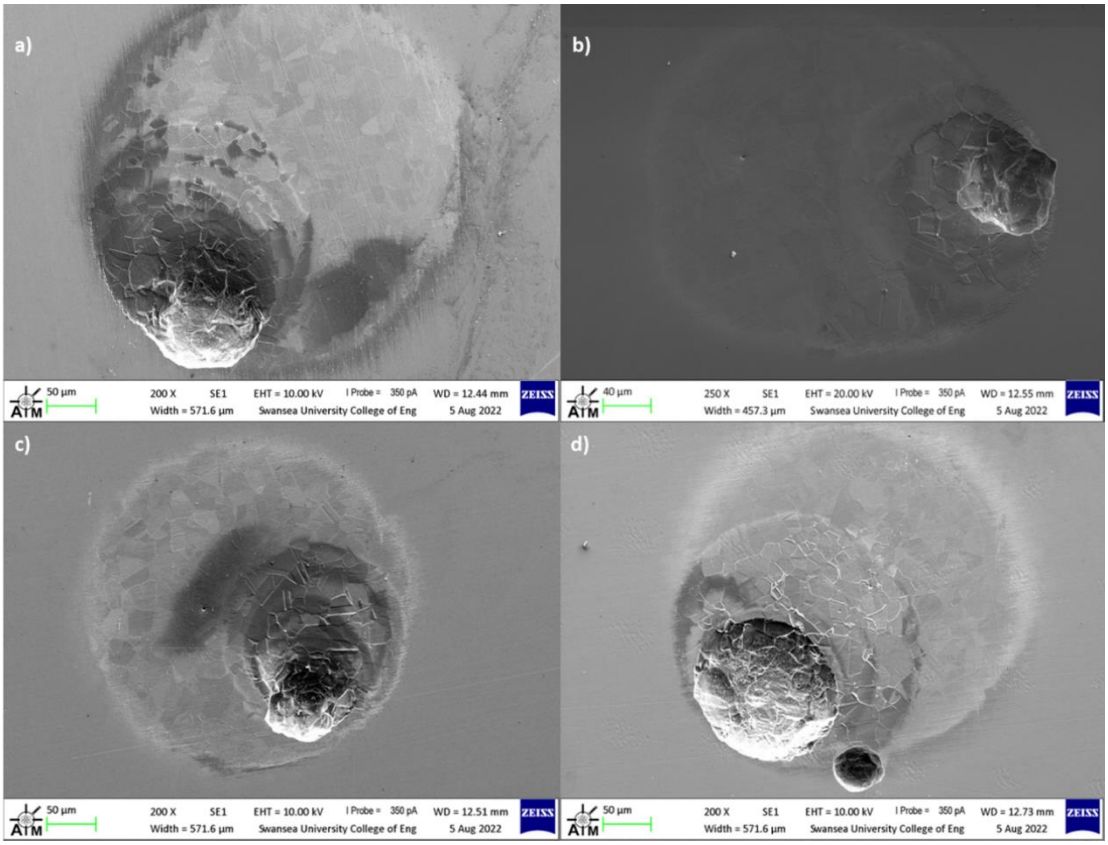

Figure 3.22 Pit morphology obtained during SVET experiments in 4 M $MgCl_2$, oserved with SEM at different magnifications. a) AISI 304 as received non-strained, b) AISI 304 as received strained, c) AISI 304 sensitised non-strained, d) AISI 304 sensitised strained.

The observed behaviour in the current density maps and the morphology obtained for all the materials tested, can be explained by the mechanism illustrated in Figure 3.23 and summarised below:

- 1 – Pit initiation on surface, which might occur due to the preferential attack of an inclusion (represented by a red rectangle). At this point, the rate of reactions is higher due to an extensive attack in the surroundings of the pit initiation site.
- 2 – Crystallographic etching at the surroundings of the inclusion. This may be due to enhanced dissolution of the passive film promoted by the acidic environment at the pit initiation site.
- 3 – Localised propagation of the pit at the inclusion site, where the acidic environment sustains the reactions. Due to the reduced area involved, the

rate at which the reactions occur on surface may decay, influencing the current density measurements.

- 4 and 5 – Further propagation of the pit where the anodic reaction can be sustained. The results suggest that just the front of propagation remains active while the surroundings passivate, resulting in an ''spiral'' like attack. The decay in the current density may be due to the reduced area involved, the increase in the distance between the active surface and the vibrating probe (which is known can alter the magnitude of the readings recorded by the SVET), corrosion products hindering ionic transport from the pit bottom to the surface or a combination of all.

On the other hand, figure 3.24 confirms the assumption that secondary pits that nucleated in some of the samples did not remain active for a long period of time, explaining the difficulties to track the current density values associated. Analysing the different images, it is notable the crystallographic etching and the presence of some voids inside the grain, due to the possible dissolution of MnS inclusions. Additionally, some microcavities can be observed alongside the grain boundaries for the sensitised material in strained condition (Figure 3.24-d), suggesting the effect of chromium carbide precipitation and dissolution.

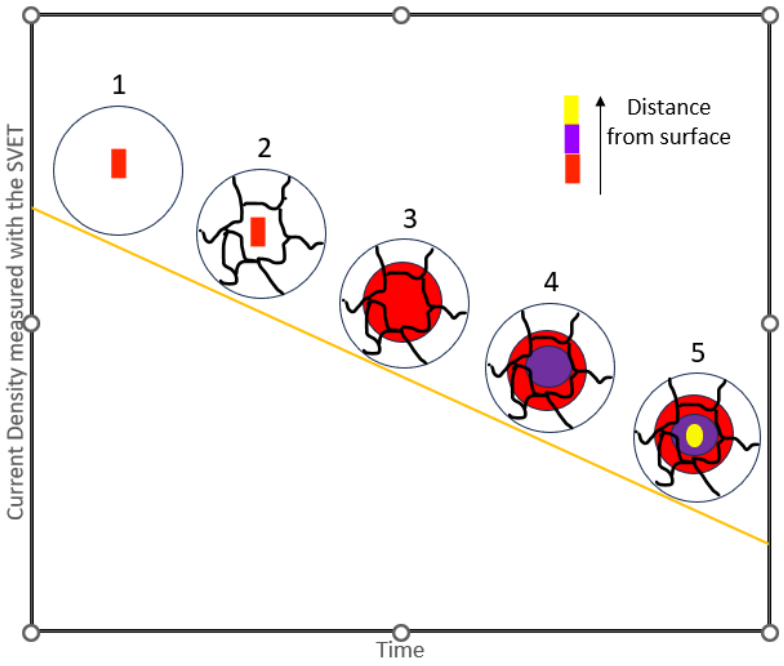

Figure 3.23. Current density variation and its relationship with the pit morphology.

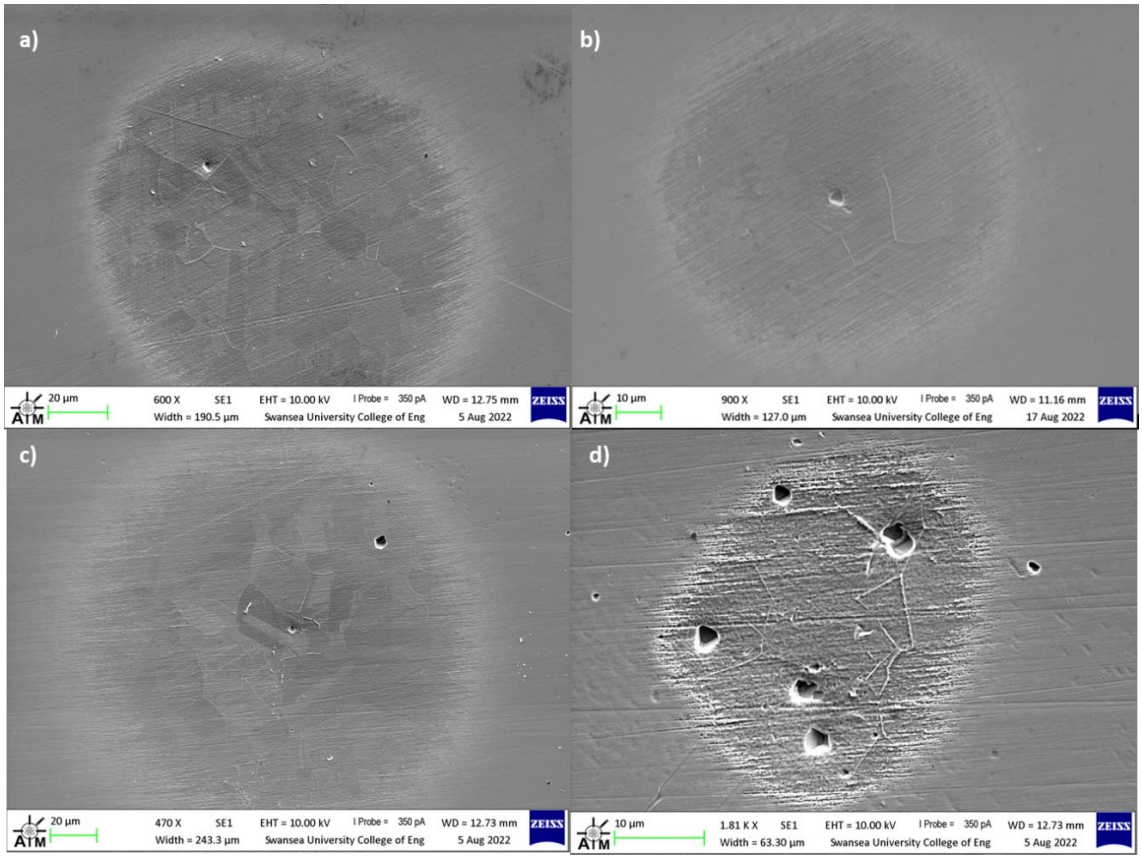

Figure 3.24 Pit morphology obtained during SVET experiments in 4 M $MgCl_2$, obtained with SEM at different magnifications. a) SS 304 as received strained, b) SS 304 sensitised non-strained, c-d) SS 304 sensitised strained.

Even though pits were obtained under strained conditions for both materials, none of the pits showed signs of intergranular stress corrosion cracking. In comparison, other researchers who observed SCC in SS 304 in non-polarised conditions, needed to implement different approaches to be able to promote cracking. For example:

- Isaacs [6] experiments with a vibrating electrode were able to observe cracking in SS 304 after adding a platinum wire to boost the cathodic area and sustain the cathodic reaction.
- Uchida et al [95] conducted experiments in a single crystal of SS 304 with a preferential orientation, which might ay have influenced in the cracking observed.
- Moore et al [97] observed cracking in their experiments in SS 304 immersed in 395 ppm sodium thiosulfate during the first day. However, prior to the

strain application, the samples were left in the same solution for a period of 6 days.

Taking this into consideration, it seems that the reduced exposure time of the samples to the 4 M $MgCl_2$ solution and the decision not to perturb the experiment using external features to boost the anodic or cathodic reaction, may have influenced in the non-proliferation of cracks.

3.4.3 Effect of strain in the current density measurements obtained with the SVET

In their studies Manhabosco et al. [96] compared the current density magnitude values between pre-strained and strained hot-dip galvanised steel samples, showing how strained specimens had a higher current density value. However, this research project did not follow the same approach. The results suggested that the value recorded by the SVET is highly dependent on the time and comparing the absolute values could give the wrong picture.

Instead, it is proposed to study the effect of strain by normalising the values, following equation 3.1.

$$\beta = \frac{J_{pit}}{J_{pit\,max}} \tag{3.1}$$

Where J_{pit} is the maximum current density measured per scan and $J_{pit\ max}$, is the maximum current density obtained. The values of β as a function of time are illustrated in figure 3.25.

Figure 3.25 show a significant lower rate of decay for both materials under the effect of strain. For the as-received material in non-strained conditions, the value decays by around 85 % in the first 24 hours, while the strained sample has a reduction of approximately 70 % at the same time. Regarding the sensitised metal, the non-strained material decreases around 90 % after 23 hours, while the strained material decays around 50 % in the same time frame.

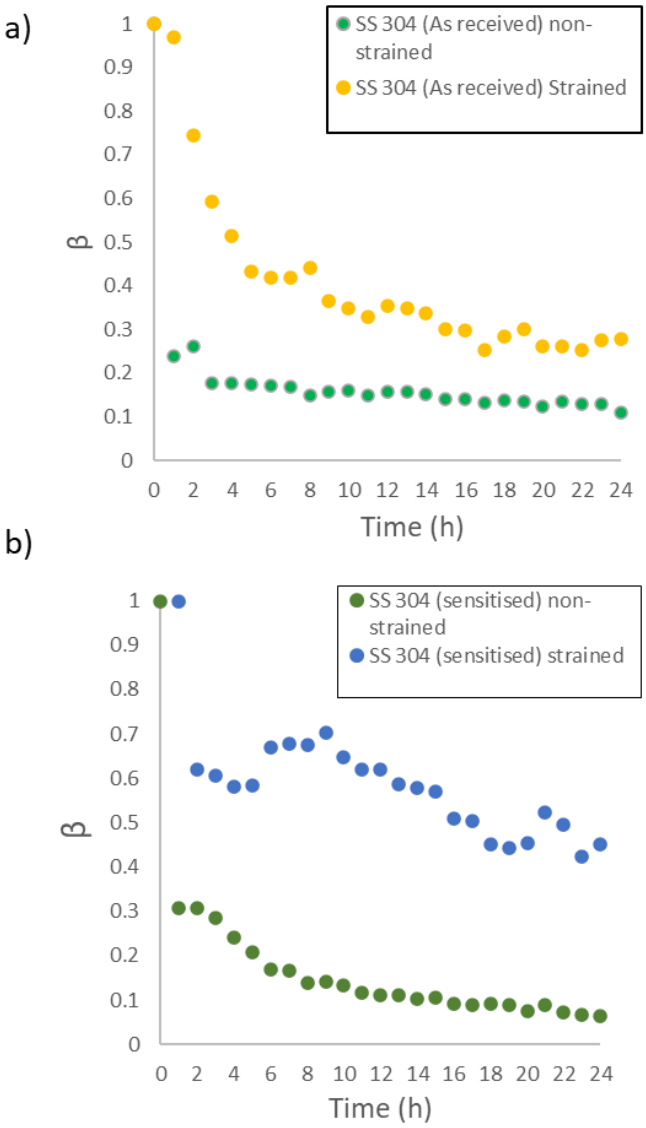

Figure 3.25 Effect of strain in the current density values obtained at pit sites, a) As received material, b) Thermally sensitised.

A different way to observe the effect of strain on the localised corrosion process was through the study of the pits with the digital height-depth microscope. The analysis was focused on the pits that remained active for the whole duration of the experiment. The results are summarised below and can be observed in figure 3.26.

- As received material: In non-strained conditions the pit had a depth of 20 µm in comparison to the 27 µm reported for the strained material.
- Sensitised material: In non-strained conditions, the pit had a depth of 26 µm in comparison to the 29 µm reported for the strained material.

- The results showed that the pits nucleated in sensitised samples also had a higher depth in comparison to the as received material. In non-strained conditions, the sensitised pit had a depth of 26 µm in comparison to the 19 µm reported for the annealed sample. Similarly, the sensitised strained material had a pit depth of 29 µm versus 27 µm reported for the annealed material under strain.

The results are in accordance with the findings reported by Breimesser et al. [98,99] who described that applied stress accelerates the dissolution of sensitised grain boundaries in low pH environments.

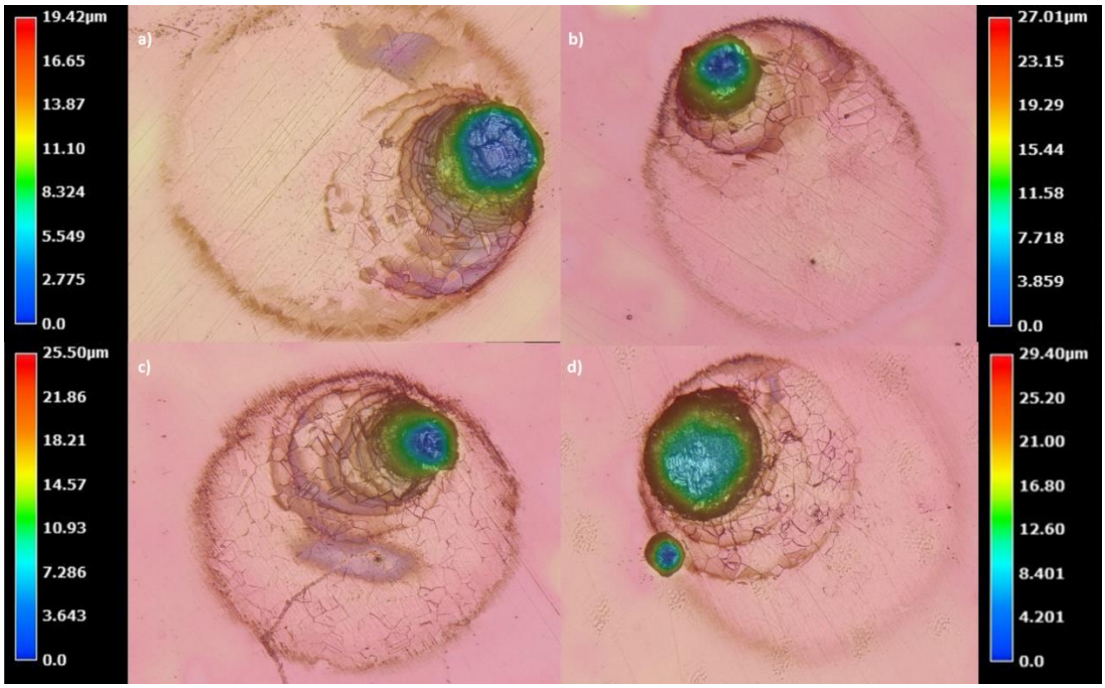

Figure 3.26 Pit depth profile obtained with the VHX-1000 digital microscope. a) AISI 304 as received non-strained. b) AISI 304 as received strained, c) AISI 304 sensitised non-strained, d) AISI 304 sensitised strained.

3.5 Conclusions

- Pitting in austenitic stainless steel 304 is dependent on the chloride concentration, being evident that 4 M $MgCl_2$ can promote stable pitting for

the material in the as received and thermally sensitised form, in strained or non-strained conditions.

- Samples under strain can nucleate pits at lower concentrations that non-strained specimens, however such pits seem not to be active for long time.
- Sensitised samples can nucleate more pits per droplet in comparison to as received samples, suggesting that sensitisation can have a negative impact on the pitting corrosion resistance.
- Strain applied on samples can influence the values obtained in potentiodynamic polarisation curves, decreasing the values of E_{corr} and E_{pit}.
- Pitting can be initiated in SS 304 in annealed and thermally sensitised conditions when immersed in 4 M $MgCl_2$ solution and open circuit conditions, while the phenomenon can be followed in-situ by SVET analysis.
- SVET was able to show significant differences in pit propagation when comparing the behaviour of both as-received and sensitised SS 304 in the presence and absence of tensile strain.
- The decay of maximum anodic pit current density values from original values measured immediately after initiation was significantly lower for both as-received and sensitised SS 304 when stress was applied. Typically an 80% decrease in J_{pit} was observed for non-strained specimens over a 24 h period, while under strained conditions J_{pit} was seemed to drop by 50% over the same timescale.

3.6 Suggestions for future work

- Study the pit propagation on samples (cross-sectional study or XCT).
- Combine the SVET with a small uniaxial tensile test machine (E.g. Deben stage), to control the load and load rate applied to the sample while scanned.
- Combine SVET with time-lapse microscopy to have visual surveillance on the localised corrosion development.
- Add other parameters to the experiments such as temperature or polarisation and observe their influence.

- Repeat the experiments using specific nuclear cladding alloys (e.g. 20Cr/25Ni/Nb) under different chloride concentration, tensile load, or temperature.

Chapter 4

4. Corrosion behaviour of 20Cr/25Ni/Nb - 45Fe/45Ni/10Cr coupons

The corrosion behaviour of metal coupons made of the bespoke nuclear alloy 20Cr/25Ni/Nb electron beam welded to a simulant sensitised grain boundary alloy (45Fe/45Ni/10Cr) was assessed. The simulant material was produced aiming to replicate the chemical composition of grain boundaries affected by radiation induced segregation (RIS), in which Fe and Cr are depleted, while Ni and Si are enriched. The electron beam welded process ensured a clean weld joint with minimal heat distortion and lower HAZ effect. The samples were used to perform different electrochemical tests such as potentiodynamic polarisation, SVET and SKP, the results obtained are shown below.

4.1 DC electrochemistry

As mentioned in section 2.6.1, potentiodynamic polarisation experiments were carried out in 1 M NaCl solutions. To compare the behaviour of the different areas of the coupons, experiments were completed in isolated areas which covered the three regions of interest (figure 2.12 for reference). The results are shown in figure 4.1 and the findings are summarised below:

- Simulant (45Fe/45Ni/10Cr): The simulant grain boundary alloy reached a corrosion potential (E_{corr}) at -240 mV (vs SCE), which was the lowest obtained between the three different sample locations. After increasing the potential to values above E_{corr} the material exhibited a high number of current transients that can be seen up to the breakdown potential, which is reached at 230 mV (vs SCE). The lack of a stable passive region can be

attributed to the Cr content in this alloy, which is below the minimum required of 10.5% for stainless steel, as specified by ASTM A240 [100].

- Cladding alloy (20Cr/25Ni/Nb): The cladding material was the most noble out of the three samples tested, obtaining a corrosion potential of -130 mV (vs, SCE), and pitting potential of 426 mV (vs SCE) being 200 mV above the value obtained by the simulant grain boundary alloy. Current density transients were also observed, but they were much less frequent than for the simulant alloy. This is likely due to the higher chromium content. The results are consistent with previous experiments on this alloy in 1 M NaCl, which found E_{corr}=-200 mV (vs. SCE) and E_{pit}=400 mV (vs. SCE) [101].
- Cladding-weld-Simulant: The bimetallic region had E_{corr} at -180 mV (vs. SCE) which is in between the values obtained for both materials. However, the results show that above the corrosion potential, the material did not exhibit a clear passive region with current density increasing exponentially for values above -50 mV (vs. SCE). It is possible that the weld joint region was thermally sensitised and due to Cr depletion could not show passivity. Additionally, post-test examination showed that several pits had nucleated at the weld joint, propagating towards the simulant material as can be seen in figure 4.2. It is important to mention that during the experiments the samples were hanging and the simulate material was facing down, which could have influenced the morphology observed in figure 4.2.

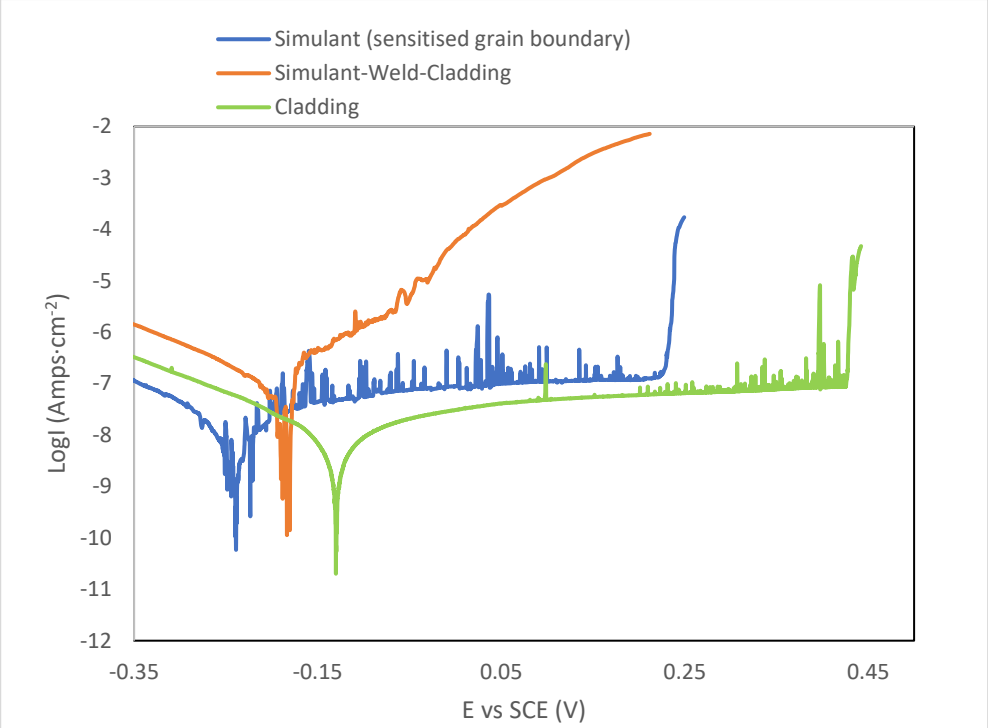

Figure 4.1 Potentiodynamic polarisation curves of different isolated regions for 20Cr/25Ni/Nb - 45Fe/45Ni/10Cr coupons in 1 M NaCl solution.

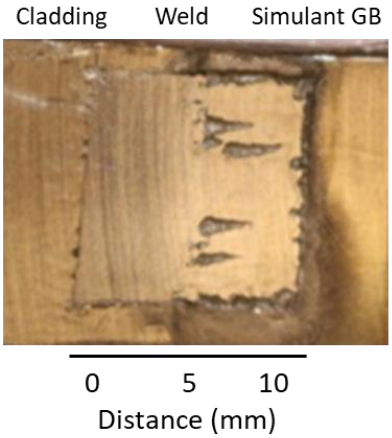

Figure 4.2 20Cr/25Ni/Nb-45Fe/45Ni/10Cr coupon following potentiodynamic polarisation in 1 M NaCl.

4.2 SVET experiments on 20Cr/25Ni/Nb - 45Fe/45Ni/10Cr coupons

One of the characteristics of the SVET, is its ability to observe the micro- and macro-electrochemical reactions occurring on the surface. This makes the SVET a good candidate for studying bimetallic welded materials under immersion.

The use of the SVET can offer a different approach to studying these coupons, which could prove to be useful in future projects. In fact, the SVET has been used previously to evaluate the changes in the corrosion resistance of metallic alloys due to the microstructural changes and residual stresses produced by different welding techniques [102-105].

The SVET current density maps for coupons (figure 4.3) where the area ratio between cladding and simulant grain boundary was 1:1, can be seen in figure 4.4. The colours observed on the maps are as follows: red areas represent the anodic activity (positive current density), blue areas represent the cathodic activity (negative current density), and the white areas the neutral regions (near zero current density).

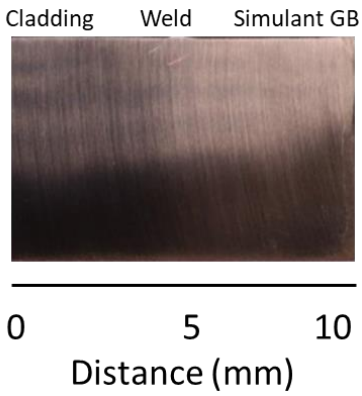

Figure 4.3 Illustration of the area exposed during the SVET experiments.

Analysing the different current density maps shown in figure 4.4, it is notable how the localised corrosion phenomenon evolved in short periods of time. The behaviour observed is summarised below:

- Figure 4.4-a: In the first scan, up to three different peaks can be seen emerging from the line where the weld was located on the sample (see figure 4.3 for reference).
- Figure 4.4-b: The activity at one of the anodic peaks on the weld joint increased sharply, while the other two peaks disappeared. This behaviour was observed in the next scan (figure 4.4-c).
- Figure 4.4-d: After 5 hours of testing, there was no significant activity.

- Figure 4.4-e: A new anodic current density peak emerges at the weld joint after 16 hours of testing, but it was not detected in subsequent scans.
- Figure 4.4-f: After 21 hours, no current density peaks could be observed at the weld joint. However, some anodic activity was recorded on the simulant GB side of the coupon.

Even though both materials have different corrosion behaviours (as seen on figure 4.1), when the area relation is 1:1 the SVET current density maps did not show a clear formation of a galvanic cell.

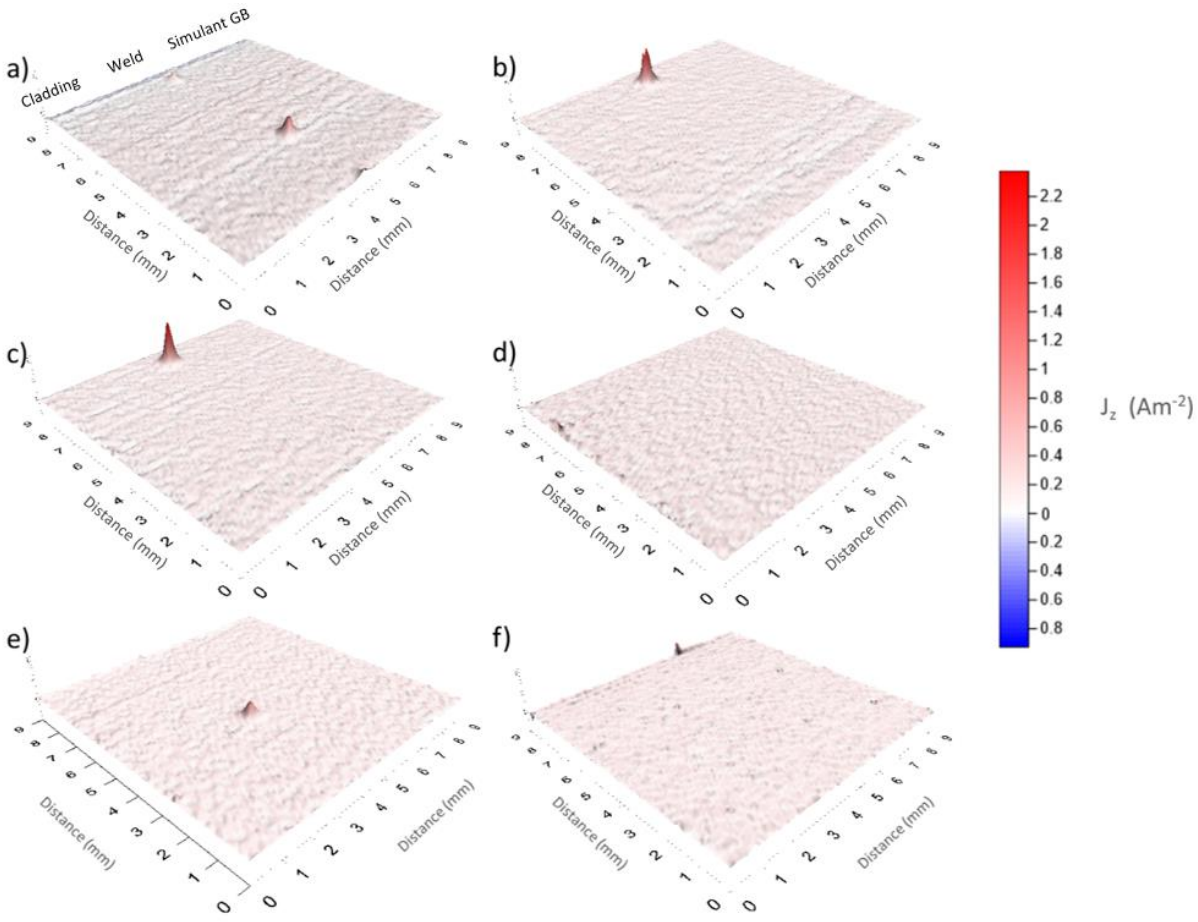

Figure 4.4 SVET current density maps for 20Cr/25Ni/Nb - 45Fe/45Ni/10Cr coupons in 1 M NaCl solution. a) 0 h, b) 2 h, c) 3h, d) 5h, e) 16 h, f) 21h.

Once the SVET experiments were completed, post-examination of the exposed surface was conducted. Only one corrosion site was found along the weld joint, at the same location where the maximum anodic peaks were observed (figure 4.4 b and c). This corrosion site is shown in figure 4.5.

Figure 4.5 clearly reveals intergranular corrosion (IGC) at the weld joint. The localised corrosion attack appears to be progressing towards the simulant alloy. The limited extent of damage aligns with the current density maps obtained, which showed an anodic current density peak that vanished after a couple of hours.

Given the low chromium content (around 10%) of the simulant alloy, the propagation of localised corrosion towards the simulant grain boundaries is not unexpected. Austenitic stainless-steels with chromium-depleted grain boundaries are well-known for their susceptibility to IGC.

Although electron beam welding typically produces clean microstructures and minimal heat affected zones (HAZ), an influence on the localised corrosion attack observed cannot be entirely ruled out.

No further corrosion sites were observed along the weld or other regions, even though the current density maps showed other anodic peaks of lower magnitude. This suggests that these sites could have repassivated.

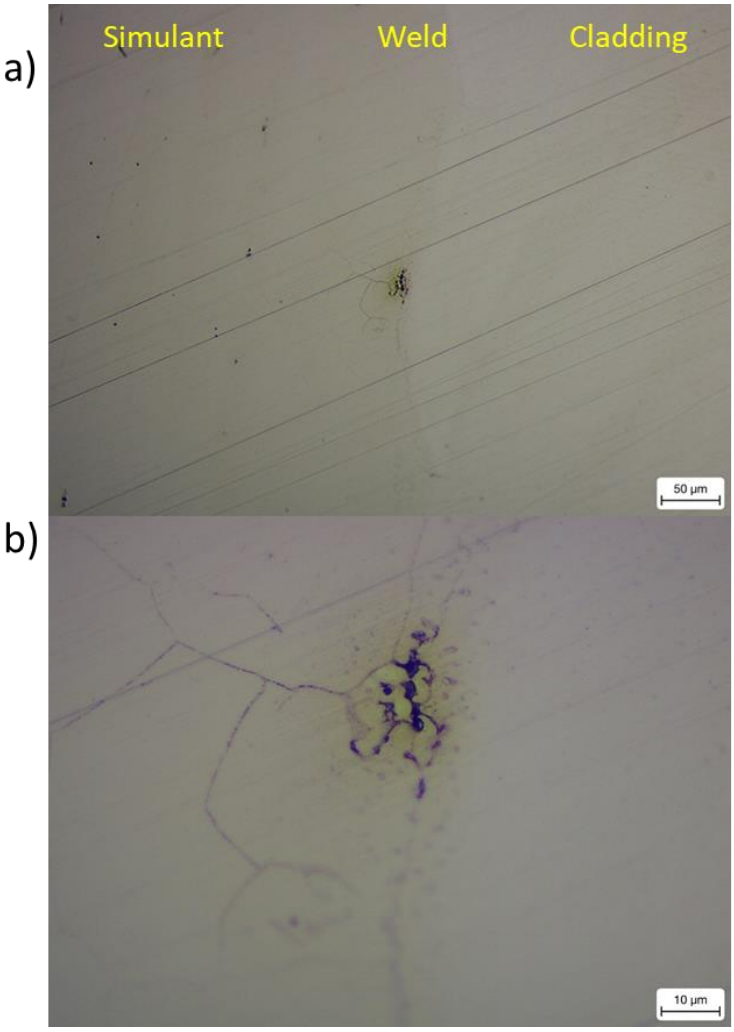

Figure 4.5. Intergranular corrosion site observed on the weld joint of the 20Cr/25Ni/Nb - 45Fe/45Ni/10Cr coupons tested with the SVET in 1 M NaCl, obtained with an optical microscope at different magnifications.

Mair and Frankel [66] demonstrated that the initiation of localised corrosion could also be detected by sudden drops in OCP. For this reason, a separate experiment measuring OCP in immersion conditions was completed and the results are shown in figure 4.6.

Analysing figure 4.6, it is noticeable the high variation in the potential during the first 10 hours of the experiments, with a tendency to stabilise at -150 mV (vs SCE). This value is close to the -180 mV (vs SCE) reported for the corrosion potential in the polarisation curve (figure 4.1). However, after 11 hours sudden drops in the OCP are observed, being possibly related to localised corrosion events.

Even though OCP and SVET experiments were not conducted in parallel, the results observed suggested that a combination between both techniques can be part of future research projects involving these coupons. Potentially showing how sudden drops in OCP potential are related to the appearance of anodic current peaks.

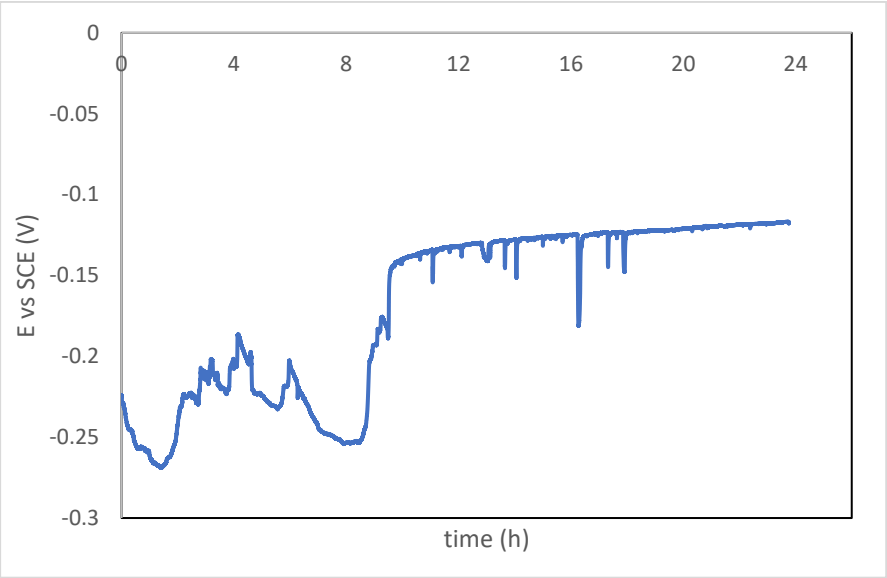

Figure 4.6 OCP measurements for 20Cr/25Ni/Nb - 45Fe/45Ni/10Cr coupons in 1 M NaCl.

4.3 SKP experiments on 20Cr/25Ni/Nb - 45Fe/45Ni/10Cr coupons

The potentiodynamic polarisation experiments reported previously, showed that the simulant grain boundary alloy is the most active region of the coupon. However, the SVET tests performed, reported that the localised corrosion sites emerge at the weld joint, rather than the simulant. To confirm the nobility of the three different regions of the coupons, an additional test was carried out with the Scanning Kelvin Probe (SKP), to observe changes in the volta potential distribution through line scans across the sample.

Figure 4.7 shows three of the seven parallel line scans (line 0, line 3 and line 6) and the potential differences measured between the regions of the coupons. The results reported correspond to measurements obtained after 16 hours of the initiation. They show that points measured at the cladding had the highest average potential value, which was at least 25 mV above the average reported for the simulant grain boundary alloy. Finally, the results confirmed that the electron beam

weld had the lowest potential, explaining why the pits initiated on this region during the SVET experiments.

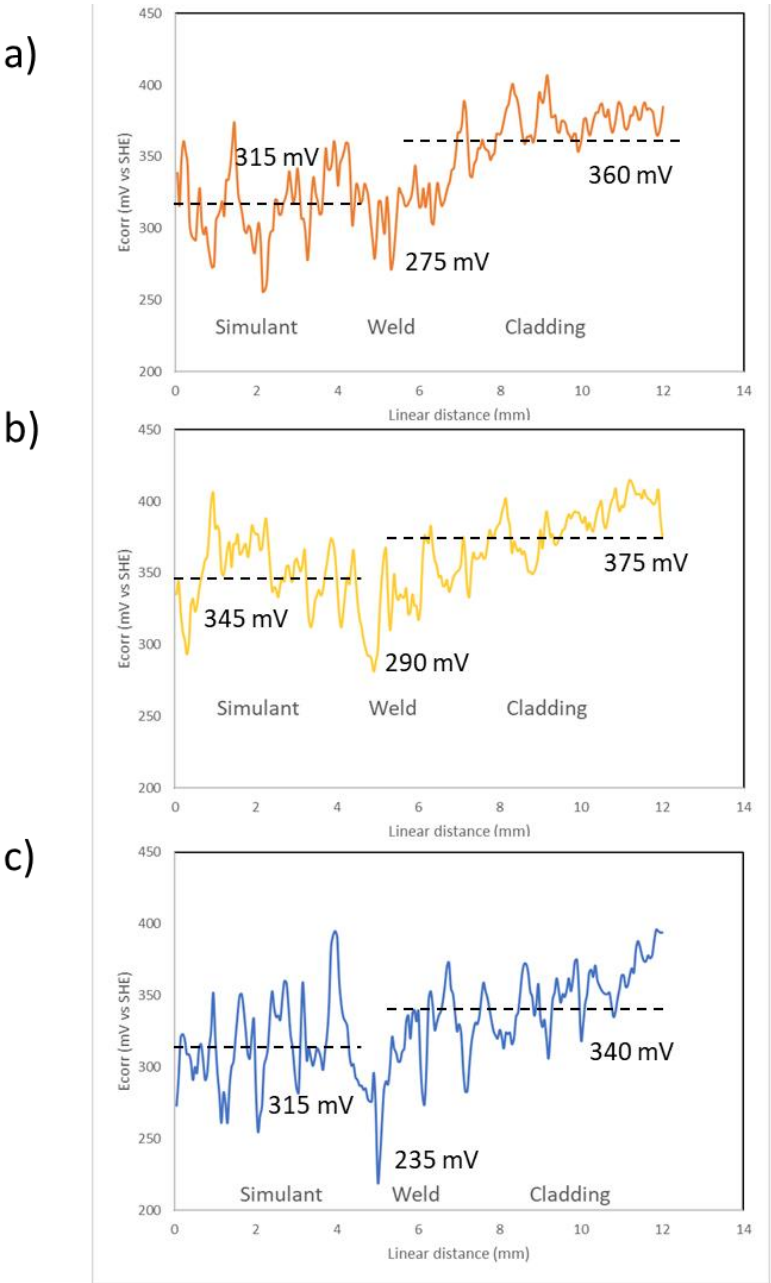

Figure 4.7 Line scans obtained with the SKP on 20Cr/25Ni/Nb - 45Fe/45Ni/10Cr coupons. a) Line scan '0', b) Line scan '3', c) Line scan '6'.

4.4 Conclusions

- Measurements taken with the SVET can detect the initiation of intergranular corrosion sites.

- Although 20Cr/25Ni/Nb and 45Fe/45Ni/10Cr have different corrosion potentials, coupons fabricated from both alloys do not exhibit the formation of a well-defined galvanic cell when immersed in 1 M NaCl solution at a 1:1 area ratio.
- The electron beam weld joint of the coupon is the most active region of the coupon and localised pit-like features were detected along the exposed length of the joint during full immersion of the bespoke cladding-grain boundary simulant specimen in 1M NaCl (aq). In contrast, SVET did not detect any evidence of localised corrosion activity on either the 20Cr/25Ni/Nb and 45Fe/45Ni/10Cr regions.

4.5 Suggestions for future work

- Repeat the experiments increasing the cladding area of the coupon to confirm any changes in the behaviour.
- Complete SVET experiments in parallel with OCP measurements.
- Analyse corrosion sites with SEM and EDS to confirm if they initiated at an inclusion site or specific phase.

List of References

[1] J.R. Davies, “Corrosion: Understanding the basis“, ASM International, first edition, pp 21-174, 2000.

[2] Association for Materials Protection and Performance, What is corrosion?, https://www.ampp.org/resources/what-is-corrosion , consulted on 27/01/2022.

[3] Bradford, “Corrosion Control”. Casti, second edition, pp 53-180, 2001.

[4] Z. Ahmad, ‘’Principles of corrosion engineering and corrosion control’’, Elsevier, pp 1-271, 2006.

[5] D.I. Hambley, “Technical Basis for Extending Storage of the UK’s Advanced Gas-Cooled Reactor Fuel, “ in Global 2013, Salt Lake City, USA (2013).

[6] H. S. Isaacs, ‘’ Initiation of Stress Corrosion Cracking of Sensitized Type 304 Stainless Steel in Dilute Thiosulfate Solution’’, J. Electrochem. Soc. vol. 135, 2180, 1988.

[7] R. N. Clark, R. Burrows, R. Patel, S. Moore, K. R. Hallam, P. E.J. Flewitt, ‘’ Nanometre to micrometre length-scale techniques for characterising environmentally-assisted cracking: An appraisal’’, Helylon, Vol. 6, e03448, 2020.

[8] R. Quiroz, M. Almeida, A. Rosales, “Laboratorio de Estabilidad de Materiales MT 4633“, Universidad Simón Bolívar, Dpto. de Ciencia de los Materiales, Sección de Corrosión, pp.5-44, 2010.

[9] H.S. Khatak, B. Raj, ‘’Corrosion of austenitic Stainless Steels Mechanism, Mitigation and Monitoring’’, Woodhead Publishing Limited, pp 24, 2002.

[10] ASM, “Stainless Steels for Design Engineers, ” ch. 6, pp. 69-78, ASM Technical books, 2008.

[11] A. Pardo, M.C. Merino, A.E. Coy, F. Viejo, M. Carboneras, R.Arrabal, “Influence of Ti, C and N concentration on the intergranular corrosion behaviour of AISI 316Ti and 321 stainless steels“, Acta Materalia, vol. 55, pp. 2239-2251, 2007.

[12] ASTM G46-94, “Standard Guide for Examination and Evaluation of Pitting Corrosion“, 2005.

[13] L. Guocheng, C. Haidong, X. Chunchun, H. Zonghu, “Effect of Strain and Chloride Concentration on Pitting Susceptibility for Type 304 Austenitic Stainless Steel“, Chinese Journal of Chemical Engineering, vol. 16, Issue 2, pp. 314-319, 2008.

[14] G. Ilevbare, G.T. Burstein, “The inhibition of pitting corrosion of stainless steels by chromate and molybdate ions“, Corrosion Science, 45, pp. 1545-1569, 2003.

[15] A. Abbasi Aghuy, M. Zakeri, M.H. Moayed, M.Mazinani, “Effect of grain size on pitting corrosion of 304L austenitic stainless steel“, Corrosion Science, vol. 94, pp. 368-376, 2015.

[16] R.T. Loto, ‘’ Pitting corrosion evaluation of austenitic stainless steel type 304 in acid chloride media’’. J. Mater. Environ. Sci. Vol. 4(4), pp. 448–459, 2013.

[17] T.H. Nguyen, R. Foley, ‘’On the mechanism of pitting of aluminum’’. J. Electrochem. Soc. Vol. 126(11), pp. 1855–1860, 1979.

[18] M. G. Fontana, N. D. Greene, “Corrosion Engineering,” 3rd Edition, McGraw-Hill, 1986.

[19] R. G. Kelly, J. R. Scully, D. W. Shoesmith, R. G. Buchheit, ‘’ Electrochemical Techniques in Corrosion Science and Engineering‘’, Marcel Dekker, pp 74-75, 2003.

[20] A. Turnbull, M. K. Gardner, ‘’Potential and pH Measurements in a Crevice of the Steel BS 4360 50D in 3·5% NaCl and in Artificial Sea Water’’, British Corrosion Journal, 16:3, pp. 140-144, 1981.

[21] G. Salamat, G.A. Juhl, R.G. Kelly, ‘’ Mechanism of Dissimilar Metal Crevice Corrosion of Superferritic Stainless Steels’’, Corrosion Science, Vol. 51 No. 11, pp. 826-836, 1995.

[22] Z. Szklarska-Smialowska, ‘’Pitting Corrosion of Metals’’, National Association of Corrosion Engineers, Houston, 1986.

[23] G.S. Eklund, “Initiation of Pitting at Sulfide Inclusions in Stainless Steel,“ Journal of the Electrochemical Society, 121(4), pp. 467-473, 1974.

[24] G. Wranglen, “Pitting and sulphide inclusions in steel“, Corrosion Science, 14(5), pp. 331-349, 1974.

[25] J.E. Castle, R. Ke, “Studies by auger spectroscopy of pit initiation at the site of inclusions in stainless steel, “ Corrosion Science, 30(4–5), pp. 409-428, 1990.

[26] S. E. Lott, R. C. Alkire, “The Role of Inclusions on Initiation of Crevice Corrosion of Stainless Steel: I . Experimental Studies “, Journal of Electrochemistry Society, 136, pp. 973-979, 1989.

[27] E. G. Webb, T. Suter, R. C. Alkire, “ Microelectrochemical Measurements of the Dissolution of Single MnS Inclusions, and the Prediction of the Critical Conditions for Pit Initiation on Stainless Steel“, Journal of Electrochemistry Society, 148, pp. B186-B195, 2001.

[28] O. Alyousif, R. Nishimura, “On the Stress Corrosion Cracking and Hydrogen Embrittlement Behaviour of Austenitic Stainless Steels in Boiling Saturated Magnesium Chloride Solutions“, International Journal of Corrosion, Vol. 2012, 2012.

[29] G.G. Scatigno, P. Dong. M.P. Ryan, M.R. Wenman, “The effect of salt loading on chloride-induced stress corrosion cracking of 304L austenitic stainless steel under atmospheric conditions“, Materalia, vol 8, 100509, 2019.

[30] Galván-Martínez, R.; Carmona, A.; Baltazar, M.; Contreras, A.; Orozco-Cruz, R. “Stress Corrosion Cracking of X70 Pipeline Steel immersed in Synthetic Soil solution”. Afinidad, vol76-585, 2019.

[31] R. Bosch, S. Ritter, M. Herbst, R. Kilian, M.G. Burke, J. Duff, F. Scenini, Y. Gu, A. Dinu, U. Ehrnstén, A. Toivonen, R. Novotny, O. Martin, F.J. Perosanz, A. Legat and B. Zajec. “Stress corrosion crack initiation testing with tapered specimens in high temperature water – results of a collaborative research project“, Corrosion Engineering, Science and Technology, Vol. 56, No. 2, pp. 103–118, 2021.

[32] N. Zhou, R. Pettersson, R.L. Peng, M. Schönning, “Effect of surface grinding on chloride induced SCC of 304L“, Materials Science & Engineering A, vol. 658, pp. 50–59, 2016.

[33] T. Suter, E. G. Webb, H. Bohni, and R. C. Alkire, '' Pit Initiation on Stainless Steels in 1 M NaCl With and Without Mechanical Stress'', 1 J. Electrochem. Soc. vol. 148, B174, 2001.

[34] S. Tokuda, I. Muto, Y. Sugawara, and N. Hara, '' Pit initiation on sensitized Type 304 stainless steel under applied stress: Correlation of stress, Cr-depletion, and inclusion dissolution'', Corrosion Science, vol. 167, 108506, 2020.

[35] N. Shimahashi, I. Muto, Y. Sugawara, and N. Hara, '' Effects of Corrosion and Cracking of Sulfide Inclusions on Pit Initiation in Stainless Steel'', J. Electrochem. Soc. vol.161, C494, 2014.

[36] S. Moore, R. Burrows, D. Kumar, M.B. Kloucek, A.D. Warren, P.E.J. Flewitt, L. Picco, O.D. Payton and T. L. Martin, "Observation of stress corrosion cracking using real-time in situ high-speed atomic force microscopy and correlative techniques", Materials Degradation, 2021.

[37] Department for Business, Energy & Industrial Strategy, (2021) , UK ENERGY IN BRIEF 2021, National Statistics, https://assets.publishing.service.gov.uk/government/uploads/system/uploads/attachment_data/file/1032260/UK_Energy_in_Brief_2021.pdf 24/01/2022.

[38] Department for Business, Energy & Industrial Strategy, (2019) , Nuclear in the UK, https://assets.publishing.service.gov.uk/government/uploads/system/uploads/attachment_data/file/789655/Nuclear_electricity_in_the_UK.pdf 24/01/2022.

[39] E. Nonbel, "Description of the Advanced Gas Cooled Type of Reactor (AGR), " Tech. Rep. November 1996, Riso national laboratory, Roskilde, 1996.

[40] E. Howett, C. Boxall, D. Hambley, "AGR Cladding Corrosion: Investigation of the Effect of Temperature on Unsensitized Stainless Steel, " MRS Advances, Vol. 2, Issue 11, pp. 615 – 620, 2017.

[41] J.S. Waddington, R.B. Sykes, E.C. (Ed.). "Properties of stainless steel cladding for use in advanced gas-cooled reactors ", United Kingdom: Metals Society, 1975.

[42] A.D. Marwick, “Segregation in irradiated alloys: the inverse Kirkendall effect and the effect of constitution on void swelling, “ J. Phys. F: Metal Phys., 8, pp. 1849-1861, 1978.

[43] A. R. Brooks, C. R. Clayton, K. Doss, and Y. C. Lu, “On the Role of Cr in the Passivity of Stainless Steel, “ J. Electrochem. Soc. 133, pp. 2459-2464, 1986.

[44] C.S. Tedmon Jr., D.A. Vermilyea, J.H. Rosolowski, “Intergranular corrosion of austenitic stainless steel, “ J. Electrochem. Soc. 118 (2), pp. 192–202, 1971.

[45] Magdy A.M.Ibrahim, S.S.Abd El Rehim, M.M.Hamza, , “Corrosion behaviour of some austenitic stainless steels in chloride environments, “ Materials Chemistry and Physics, Vol 115, Issue 1, pp. 80-85,2008.

[46] International Atomic Energy Agency and E. Agency, “Further analysis of extended storage of spent fuel,” IAEA-TECDOC-944, pp. 7-45, 1996.

[47] British Energy, “How an AGR power station works, “ https://archive.uea.ac.uk/~e680/energy/energy_links/nuclear/How_an_AGR_power_station_works.pdf , 26/01/2022.

[48] J. Kyffin, ‘’The Technical Case for Interim Storage of AGR Fuel’’, Sustainable Nuclear Energy Conference, 2014.

[49] K. A. Bradshaw, “Fuel pin dimensional changes in AGRs ,“ Gas-cooled reactors today, pp. 37–42, 1982.

[50] G.O.H. Whillock, B.J. Hands, T.P. Majchrowski, D.I. Hambley, ‘’Investigation of thermally sensitised stainless steels as analogues for spent AGR fuel cladding to test a corrosion inhibitor for intergranular stress corrosion cracking’’, J. Nucl. Mater. 498

[51] R. N. Clark, C.M. Chan, T.L. Martin , W.S. Walters, D. Engelberg, R. Burrows, G. Williams, “The effect of sodium hydroxide on niobium carbide precipitates in thermally sensitised 20Cr-25Ni-Nb austenitic stainless steel“ Corrosion Science, 170, pp 1-14, 2020.

[52] R.N. Clark, J. Searle, T.L. Martin, W.S. Walters, G. Williams, ''The role of niobium carbides in the localised corrosion initiation of 20Cr25Ni-Nb advanced gas-cooled reactor fuel cladding'', Corrosion Science, 165, 108365, 2020.

[53] E. Weidmann, A. Guesnier, B. Taylor, " Metallographic preparation of stainless steel", Struers, 2019.

[54] ASTM G39-99, "Standard Practice for Preparation and Use of Bent-Beam Stress-Corrosion Test Specimens" , 2021.

[55] BS EN ISO 8407, ''Corrosion of metals and alloys – Removal of corrosion products from corrosion test specimens'', 2021.

[56] ASTM E8/E8M − 13a, "Standard Test Methods for Tension Testing of Metallic Materials", 2013.

[57] A. C. Bastos, M. C. Quevedo, O. V. Karavai, M. G. S. Ferreira, " Review—On the Application of the Scanning Vibrating Electrode Technique (SVET) to Corrosion Research ", Journal of the Electrochemical Society, vol 164, pp C973-C990, 2017.

[58] G. Williams and H. N. Mcmurray, "Localized Corrosion of Magnesium in Chloride-Containing Electrolyte Studied by a Scanning Vibrating Electrode Technique," Journal of the Electrochemical Society, vol. 155, no. 7,pp. C340–C349, 2008.

[59] H. N. McMurray, D. Williams, and D. A. Worsley, ''Artifacts Induced by Large-Amplitude Probe Vibrations in Localized Corrosion Measured by SVET'', Journal of The Electrochemical Society, vol. 150, no. 12, pp B567-B573, 2003.

[60] B. P. Wilson, ''*Scanning Electrochemical Techniques for the Monitoring of Localised Corrosion on Automotive Steels*'', PhD thesis, Swansea University, 2003.

[61] BioLogic, ''*SKP101: An Introduction to Scanning Kelvin Probe*'', https://www.biologic.net/topics/skp101-an-introduction-to-scanning-kelvin-probe/ 15/04/2023.

[62] R. Waldram, '' *Investigating Corrosion Behaviour of Nickel-Plated Steel for Circulation Coinage '',* ENgD Thesis, Swansea University, 2019.

[63] G. Williams, H.N. McMurray, '' *Chromate Inhibition of Corrosion-Driven Organic Coating Delamination Studied Using a Scanning Kelvin Probe Technique* '', Journal of The Electrochemistry Society, Vol 148 B377, 2001.

[64] Y. Tsutsumi, A. Nishikata, and T. Tsuru, ''Pitting corrosion mechanism of type 304 stainless steel under a droplet of chloride solutions'', Corrosion Science, Vol 49(3): p. 1394-1407, 2007.

[65] T. Tsuru, K.I. Tamiya, and A. Nishikata, ''Formation and growth of micro-droplets during the initial stage of atmospheric corrosion'', Electrochimica Acta, Vol. 49(17-18): p. 2709-2715, 2004.

[66] B. Maier and G.S. Frankel, ''Pitting corrosion of bare stainless steel 304 under chloride solution droplets'' Journal of the Electrochemical Society, 157(10): p. C302-C312, 2010.

[67] Hastuty, S., A. Nishikata, and T. Tsuru, ''Pitting corrosion of type 430 stainless steel under chloride solution droplet''. Corrosion Science, 52(6): p. 2035-2043, 2010.

[68] L. Guo, S. Street, M. Haval, M. Ghahari, N. Mi, S. Glanvill, A. Du Plessis, C. Reinhard, T. Rayment, A. Davenport, '' The effect of relative humidity change on atmospheric pitting corrosion of stainless steel 304L'', Corrosion Science, 150, pp. 110-120, 2019.

[69] M. Matsumi, A. Nishikata, and T. Tsuru, Abstract 91, The Electrochemical Society and The Electrochemical Society of Japan Meeting Abstracts, Vol. 1999–2, Honolulu, HI, Oct 17–22, 1999.

[70] Y. Tsutsumi, , A. Nishikata, and T. Tsuru, ''Monitoring of rusting of stainless steels in marine atmospheres using electrochemical impedance technique'' Journal of the Electrochemical Society, vol 153(7): p. B278-B282, 2006.

[71] S.R. Street, N. Mi, A. Cook, H.B. Mohammed-Ali, L.Y. Guo, T. Rayment, A.J. Davenport, '' Atmospheric pitting corrosion of 304L stainless steel: the role of highly concentrated chloride solutions'' , Faraday Discuss. 180, pp. 251–265, 2015.

[72] J.R. Galvele, '' Transport processes and mechanism of pitting of metals'', J. Electrochem. Soc. 123, pp. 464–474, 1976.

[73] P. Marcus, I. Olefjord, '' A Round Robin on combined electrochemical and AES/ESCA characterization of the passive films on Fe-Cr and Fe-Cr-Mo alloys'', Corrosion Science, vol 28 (6), pp 589-602, 1988.

[74] S. S. M. Tavares, V. Moura, V. C. da Costa, M. L. R. Ferreira, and J. M. Pardal, '' Microstructural changes and corrosion resistance of AISI 310S steel exposed to 600–800 °C'', Mater. Charact., 60, pp. 573 – 578, 2009.

[75] M. W. A. Rashid, M. Gakim, Z. M. Rosli and M.A Azam, '' Formation of Cr23C6 during the Sensitization of AISI 304 Stainless Steel and its Effect to Pitting Corrosion'', Int. J. Electrochem. Sci., Vol. 7, pp. 9465 – 9477, 2012.

[76] R. L. Plaut, C. D. M. Herrera, P. R. Rios, and A. F. Padilha, '' A short review on wrought austenitic stainless steels at high temperatures: processing, microstructure, properties and performance'', Mater. Research, 10, pp. 453 – 460, 2007.

[77] A. J. Davenport, L. Guo, N. Mi, H. Mohammed-Ali, S. M. Ghahari, S. R. Street, N.J. Laycock, T. Rayment, C. Reinhard, C. Padovani, and D. Krouse '' Mechanistic studies of atmospheric pitting corrosion of stainless steel for ILW containers'', Corros. Eng., Sci. Technol., Vol 49(6), pp. 514–520, 2014.

[78] X. Zhao, C. Cheng, D. Zhang, Y. Zhao, T. Cao, S. Zhong, L. Zhang, J. Zhao, '' Effect of U-bending deformation on pitting corrosion of 2205 duplex stainless steel under wet-dry cycling of chloride salt droplets'', Corrosion Science, vol 218, 111185, 2023.

[79] Y. Hou, J. Zhao, C. Cheng, L. Zhang, J. Li, B. Liu, T. Cao, '' The metastable pitting corrosion of 2205 duplex stainless steel under bending deformation'', Journal of Alloys and Compounds, Vol. 830, 154422, 2020.

[80] R. H. Jones, M. A. Friesel, and R. Pathania, '' Evaluation of Stress Corrosion Crack Initiation Using Acoustic Emission'', Corrosion, vol. 47 (2), pp. 105-115, 1991.

[81] R. H. Jones, M. A. Friesel, and R. Pathania, '' Acoustic Emission During Pitting and Transgranular Crack Initiation in Type 304 Stainless Steel'', Corrosion, 48 (9), pp. 751-758, 1992.

[82] N. Ida, I. Muto, Y. Sugawara, N. Hara, '' Local electrochemistry and in situ microscopy of pitting at sensitized grain boundary of type 304 stainless steel in NaCl solution'', J. Electrochem. Soc., vol. 164, pp. 779–787, 2017.

[83] R. P. V. Cruz, A. Nishikata and T. Tsuru, ''Pitting corrosion mechanism of stainless steels under wet-dry exposure in chloride-containing environments'', Corrosion Science, Vol. 40(1), pp 125–139, 1998.

[84] K. Nakao, E. Tada, and A. Nishikata, '' Stress Corrosion Cracking of Sensitized 304 Stainless Steel Under MgCl2 Droplets'', ECS meeting Abstracts, Vol. MA2015-02, 672, 2015.

[85] A. B. Cook, S. B. Lyon, N. P. C. Stevens, R. C. Newman, M. Gunther, G. McFiggans, D. L. Engelberg, '' Assessing the risk of under-deposit chloride-induced stress corrosion cracking in austenitic stainless steel nuclear waste containers'', ECS Trans., Vol. 58, 25, 2014.

[86] S. Shoji and N. Ohnaka, ''Effect of relative humidity and chloride type on stainless-steel room temperature atmospheric corrosion cracking'', Boshoku Gijutsu (Corros. Eng. JP, Eng. Edn), Vol. 38, pp.111–119, 1989.

[87] S. Shoji and N. Ohnaka, ''Effect of relative humidity and chloride type on atmospheric stress corrosion cracking of stainless steels at room temperature'', Boshoku Gijutsu, Vol. 38, PP. 92–97, 1989.

[88] S. Shoji, N. Ohnaka, Y. Furutani and T. Saito, ''Effects of relative humidity on atmospheric stress corrosion cracking of stainless steels'', Boshoku Gijutsu, Vol. 35, pp. 559–565, 1986.

[89] A. Iversen and T. Prosek, ''Atmospheric stress corrosion cracking of austenitic stainless steels in conditions modelling swimming poolhalls'', Eurocorr 2007, Freiburg im Breisgau, Germany, September 2007, EFC, Paper No. 1142.

[90] T. Prosek, A. Iversen and C. Taxen, ‘‘Low temperature stress corrosion cracking of stainless steels in the atmosphere in presence of chloride deposits’’, Corrosion 2008, New Orleans, LA, USA, March 2008, NACE, Paper No. 08484.

[91] T. Prosek, A. Iversen, C. Taxen and D. Thierry, ‘‘Low temperature stress corrosion cracking of stainless steels in the atmosphere in presence of chloride deposits’’, Corrosion, Vol. 65 (2), pp. 105–117, 2009.

[92] R.N. Clark, J. Humpage, R. Burrows, H. Godfrey, M. Sagir and G. Williams ‘’ A Study into the Localized Corrosion of Magnesium Alloy Magnox Al-80 ‘’ Corrosion, 77 (2), pp. 168-182. 2021.

[93] A. Laferrere, R. Burrows, C. Glover, R. N. Clark, O. Payton, L. Picco, S. Moore, G. Williams, ’’ In situ imaging of corrosion processes in nuclear fuel cladding’’, Corros. Eng. Sci. Technology, 52 (8), pp. 596-604, 2017.

[94] S. Geary, H. N. McMurray, A. C. A. de Vooys, ‘’ High Resolution Characterization of Pitting Corrosion Using a Novel Environmental SVET and White Light Interferometry’’, ECS Transactions, Vol. 50, 47, 2013.

[95] H. Uchida, M. Yamashita, S. Inoue, K. Koterazawa, ‘In-situ observations of crack nucleation and growth during stress corrosion by scanning vibrating electrode technique’, Materials Science and Engineering, A319-321, pp. 496-500, 2001.

[96] S.M. Manhabosco, R.J.C. Batista, S. Neves da Silva, L.F.P. Dick,’’ Determination of current maps by SVET of hot-dip galvanized steel under simultaneous straining’’, Electrochimica Acta, Vol. 168, pp 89-66, 2015.

[97] S. Moore, R. Burrows, L. Picco, T. Scott, A. Laferrere, P. G. Martin, and O. D. Payton, ‘’ Investigating Corrosion Using High-Speed AFM’’, unpublished work, 2017.

[98] M. Breimesser, S. Ritter, H. Seifert, S. Virtanen, T. Suter, ‘’ Application of the electrochemical microcapillary technique to study intergranular stress corrosion cracking of austenitic stainless steel on the micrometre scale’’, Corros. Sci., Vol. 55, pp, 126-132, 2012.

[99] M. Breimesser, S. Ritter, H. Seifert, T. Suter, S. Virtanen, ‘’Application of electrochemical noise to monitor stress corrosion cracking of stainless steel in tetrathionate solution under constant load’’, Corros. Sci., vol. 63, pp.129-139, 2012.

[100] ASTM A240/A240 M, ‘’Chromium and Chromium-Nickel Stainless Steel plate, sheet, and Strip for pressure vessels and General Apllications’’. ASTM International, 2018.

[101] R. N. Clark, C. M. Chan, S. Walters, D. Engelberg, and G. Williams, ‘’ Intergranular and Pitting Corrosion in Sensitized and Unsensitized 20Cr-25Ni-Nb Austenitic Stainless Steel’’, Corrosion, Vol 77 (5), pp. 550-561, 2021.

[102] S. Weng, Y. Huang, F. Xuan, S. Zheng, ‘’ Fracture location transition in constant load tests of a NiCrMoV steel welded joint’’, Materials and Design, 181, 108072, 2019.

[103] S. Wang, J. Ding, H. Ming, Z. Zhang, J. Wang, ‘’ Characterization of low alloy ferritic steel–Ni base alloy dissimilar metal weld interface by SPM techniques, SEM/EDS, TEM/EDS and SVET’’, Materials Characterisation, vol. 100, pp. 50-60, 2015.

[104] R. Akid, P. Roffey, D. Greenfield, D. Guillen, ‘’ Application of scanning vibrating electrode technique (SVET) and scanning droplet cell (SDC) techniques to the study of weld corrosion’’, Local Probe Techniques for Corrosion Research – European Federation of Corrosion (EFC) series, pp. 23-32, 2007.

[105] R. Akid, P. Roffey, D. Greenfield, D. Guillen, ‘’Application of scanning vibrating electrode technique (SVET) to the study of weld corrosion’’, Eurocorr 2004, Long Term Prediction and Modelling of Corrosion, Code 93031, 2004.